Low Velocity Impact Properties of Sandwich Insulated Panels with Textile - Reinforced Concrete Skin and Aerated Concrete Core

by

Vikram Dey

A Thesis Presented in Partial Fulfillment
of the Requirements for the Degree
Master of Science

Approved November 2012 by the
Graduate Supervisory Committee:

Barzin Mobasher, Chair
Subramaniam D. Rajan
Narayanan Neithalath

ARIZONA STATE UNIVERSITY

December 2012

ABSTRACT

The main objective of this study is to develop an innovative system in the form of a sandwich panel type composite with textile reinforced skins and aerated concrete core. Existing theoretical concepts along with extensive experimental investigations were utilized to characterize the behavior of cement based systems in the presence of individual fibers and textile yarns. Part of this thesis is based on a material model developed here in Arizona State University to simulate experimental flexural response and back calculate tensile response. This concept is based on a constitutive law consisting of a tri-linear tension model with residual strength and a bilinear elastic perfectly plastic compression stress strain model. This parametric model was used to characterize Textile Reinforced Concrete (TRC) with aramid, carbon, alkali resistant glass, polypropylene TRC and hybrid systems of aramid and polypropylene. The same material model was also used to characterize long term durability issues with glass fiber reinforced concrete (GFRC). Historical data associated with effect of temperature dependency in aging of GFRC composites were used. An experimental study was conducted to understand the behavior of aerated concrete systems under high stain rate impact loading. Test setup was modeled on a free fall drop of an instrumented hammer using three point bending configuration. Two types of aerated concrete: autoclaved aerated concrete (AAC) and polymeric fiber-reinforced aerated concrete (FRAC) were tested and compared in terms of their impact behavior. The effect of impact energy on the mechanical properties was investigated for

various drop heights and different specimen sizes. Both materials showed similar flexural load carrying capacity under impact, however, flexural toughness of fiber-reinforced aerated concrete was proved to be several degrees higher in magnitude than that provided by plain autoclaved aerated concrete. Effect of specimen size and drop height on the impact response of AAC and FRAC was studied and discussed. Results obtained were compared to the performance of sandwich beams with AR glass textile skins with aerated concrete core under similar impact conditions. After this extensive study it was concluded that this type of sandwich composite could be effectively used in low cost sustainable infrastructure projects.

ACKNOWLEDGEMENTS

I would like to express my sincere gratitude to my advisor and committee chair, Dr. Barzin Mobasher, for his undivided attention, guidance, encouragement and motivation throughout my research. I would like to extend my regards to Dr. Subramaniam D. Rajan and Dr. Narayanan Neithalath for being in my thesis committee and providing me insight into several technical nuances that I tried to utilize throughout my Master's degree program. I would also like to acknowledge Dr. Amir Bonakdar for continuously challenging yet supporting me throughout my research work. I greatly appreciate the assistance provided by Peter Goguen and Kenneth Witczak for all the laboratory works. I would like to acknowledge all my classmates and colleagues, especially Sean Krauss, Arumugam Deivanayagam, and Yiming Yao. I would also thank Giulio Zani, Christopher Barsby, Dr. Deju Zhu and Zvi Cohen for their assistance in some of my work. I am very glad to have the moral support from all my friends Lavannya, Vaidehi, Aditi, Nikhil, Vamsi, Abhinav and Deepak. I would also like to express my gratitude to all the SSEBE and ASU administrative staffs for their kind help and support. I would like to acknowledge Navajo Flexcrete Building Systems and AAC Structures of Arizona for providing me some of the necessary material resources for this study.

I dedicate this to my grandmother, Late Anita Nag, my parents Radha and Dilip Kumar Dey, my brother Ankur Dey, my teacher Chitra Bhattacharjee. Without their love, mentoring and motivation this journey would not have been possible.

TABLE OF CONTENTS

Page

CHAPTER Page

CHAPTER Page

LIST OF TABLES

Page

Page

LIST OF FIGURES

Page

Page

Page

Page

Page

1. INTRODUCTION

One of the major challenges for the 21st century is to provide support for civil infrastructure systems to sustain economic growth and continuous societal developments. There is an urgent need to address to the concerns of global warming, ever increasing resource cost, and efficient energy usage. Concept of sustainability has gained immense importance over the years and is probably the only way ahead. From a global perspective, amongst the several sections of this society there is a staggering demand of building material sustaining the exponential growth of infrastructure. Concrete being one of the most consumed building materials; a lot of research is going on to increase durability, design light weight structural members, and develop building systems with low cement and utilize renewable energy resources. Lowering the cost of building materials is also one of the key aspects of sustainable infrastructure especially in the developing nations. This study is majorly based on evaluating the performance of fiber and textile reinforcement in brittle cementitious matrices. Plain concrete has always been known as a brittle material with weak tension capacities. Fabric based cement composites aid in improving tensile strength and stiffness along with introduction of ductility in the infrastructure systems. This type of fabric reinforced concrete could be used in wide range of structural and non-structural applications [1]. The main advantages of addition of fibers are to control crack propagations and provide post-cracking strength and ductility [2]. However considering this as a rather contemporary material, a lot of work is being done to theoretically characterize the behavioral changes incorporated in concrete systems

due to fabric additions [3]. Guidelines for design methodologies are needed to be incorporated in design and analysis of such exotic composite systems [1]. Another approach of this study is to study how to modify the cementitious matrix itself with cellular concrete system characterized by high fly ash substitution. Avoiding usage of coarse aggregates is another way to address the issue of sustainability, by making the structure light-weight. However with this sort of a material constitution, the strength of the system gets compromised. Although with the advantages of thermal efficiency, aerated (cellular) concrete could be used as a viable, cost effective, green construction material. Again internal reinforcement with fibers could be applied in order to improvise some of the structural properties of aerated concrete. Addition of low volume fine polymeric polypropylene fibers inside the aerated concrete matrix was studied in detail. Another alternative is textile reinforced sandwich composite with aerate concrete as the core material was investigated. This new-age sustainable cement-based sandwich composite can be considered as a competent alternative to traditional infrastructural material.

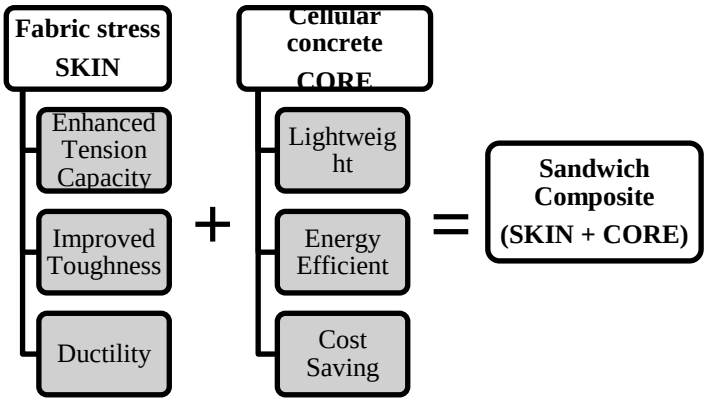

Figure 1-1 : Plan of this study

This study has been summarized in Figure 1-1 and the objectives of the individual chapters of this thesis have been briefly introduced in the subsequent sections of this chapter.

1.1 Textile reinforced cementitious composites

With a significant degree of strength, ductility, and versatility, the field of Strain Hardening Cement Composites (SHCC) has been led by novel cement based materials such as Textile Reinforced Concrete (TRC) [4]. With as much as one order of magnitude higher strength and two orders of magnitude higher ductility than fiber reinforced concrete (FRC), TRC's development has utilized innovative textiles, cementitious matrices, and manufacturing processes. A variety of individual fiber and textile systems such as alkali resistant glass (G) fibers, polypropylene (P), aramid (A), and carbon (C) have been utilized [1][5][6]. Mechanical properties of the composites under uniaxial tensile, flexural, and shear tests indicate superior performance such as tensile strength as high as 25 MPa, and strain capacity of 1-8%. In order to fully utilize these materials, material properties and design guidelines are needed to determine the size and dimensions, and expected load carrying capacity of structural members constructed with them. This chapter presents an approach applicable to the back calculation of material properties and design of TRC materials.

1.2 Aging of glass-fiber reinforced cement composite

Glass fiber reinforced concrete is a cement based composite that is generally used in the manufacturing of cladding panels and architectural accents. High strength alkali resistant glass fiber (AR-Glass) is used in a spray up

production technique with a blended Portland cement with polymers added in for curing aid. Short and chopped fibers bridge the micro cracks and by the process of de-bonding and pullout serve to transfer the load across the crack faces. GFRC is a high fiber content composite, typically it contains between 3% and 5% AR glass fibers of the total composite weight. The high fiber loading makes GFRC different from many other fiber-reinforced concrete materials which typically have fiber dosages less than 1% by weight. GFRC has proved to be a very durable building material for many products such as architectural panels of all types, utility products, roofing products, portable buildings, artificial rockwork, highway noise barriers, agricultural products, and many other products.

Long term properties of fiber reinforced composite exposed to humid environments exhibit embitterment and loss of flexural strength over time [7, 8, 9]. The deterioration is primarily caused by the chemical and physical processes. Glass fibers chemically degrade in the alkaline environment of hydrated cement paste and with time lose some of their tensile strength. The physical cause of strength reduction comes from the hydration products, especially calcium hydroxide which fills spaces between the fiber filaments and reduces the compliance of the fiber yarn. This causes stress concentration and excessive bonding at the surface of fibers, changing fiber pullout mechanism to fiber breakage under tension loading. The aging problem of glass fiber in alkaline environment led to the development of several measures such as the invention of alkali-resistant glass fibers, use of polymer emulsions in cement matrix, and addition of pozzolanic materials to react with calcium hydroxide. In order to

evaluate the improvement of GFRC for various treatments, accelerated aging procedures have been developed and the test results can be correlated with the natural aging collected from the fields [10,11,12,13]. An analytical model has been recently developed for predicting flexural behavior of fiber reinforced concrete [14,15]. This approach has been extended to both strain softening and strain hardening materials [16]. Therefore a rational modeling approach for GFRC is possible. The main objective of this chapter is to develop a procedure for using the aging flexural test data to predict the long term flexural and tensile behavior of GFRC.

1.3 Flexural impact tests on aerated concrete

Structural elements may be exposed to severe impact loads characterized by very high strain rates though for only a short duration. During the life span of structural members such as wall panels, hydraulic structures, floor panels; impact events due to hurricanes, wind and seismic loads, and ballistic projectile are expected. During such events, large amount of energy is transmitted to the structure in the form of dynamic loads. Certain impact events are characterized by low impact velocity, but high projectile mass which may cause significant damage. Structures generally respond through a variety of interactive mechanical properties which include strength, absorbed energy, deformation capacity and ductility. Cement-based materials generally exhibit low tensile strength and are inherently brittle by nature. Exposure to impact loading can thus cause extensive damage characterized by severe cracking, and ultimately complete failure. Fiber reinforcement aids in improvement of ductility, tensile, impact and flexural

performance of concrete systems. This makes them ideal for use under blast, impact, seismic and dynamic loads. However they have rate-dependent mechanical properties such as Young's modulus, ultimate strength, and fracture toughness. Considering the unique characteristics of fiber-reinforced concrete composites, the same finds its application as a tool to withstand high energy explosives [1]. Impact properties were investigated under three point bending conditions using an instrumented drop weight impact system. The instrumentation includes a conventional strain gage based load cell to record the impact loading, a linear variable differential transformer to measure mid-span deflection of the specimen, and an accelerometer mounted on its tension zone to determine acceleration of the specimen. Study was conducted based on the influence of different drop heights of hammer (dropping mass), size of specimen, along with effect of inherent material properties of aerated concrete. Specimens were tested at initial heights of 25 mm, 75 mm, and 150 mm of the impactor. Time history of the load, acceleration, deflection responses, absorbed energy of the specimen are discussed in detail. Processing, analysis and interpretation of raw and filtered experimental responses have been mentioned in subsequent sections.

2. CHARACTERIZATION OF FABRIC REINFORCED CEMENT-BASED SKIN COMPOSITES

Textile reinforcement in concrete has been a topic of interest in several research initiatives. Reinforcement in the form of yarns of textiles brings about improved tensile strength, strain capacity and enhanced toughness [17]. In this chapter, experimental flexural and tension tests conducted on mono-fibre type textile reinforced concrete with carbon alkali resistant (AR) glass, aramid, and polypropylene textile reinforced concrete have been discussed. Hybrid systems with multi-layer fabrics help in adding up the benefits of individual yarns into a unique superior composite material. Thus optimal performance of such composites can be achieved by combining different fabrics in hybrid formation. Proper characterization of such innovative materials can help us in controlling desired material properties by orienting the fabric of varied stiffness and strengths along specific directions of loading.

A parametric model [1] for simulation of tensile behaviour of reinforced cement-based composites is used to correlate the tensile stress - strain constitutive relation with flexural load carrying capacity of Textile Reinforced Concrete (TRC) composites. Using a back-calculation approach, the results of tensile experiments of composites are converted to a parametric model of a strain hardening/softening material and closed form equations for representation of flexural response of sections are obtained. Results are then implemented as average moment-curvature relationship in the structural design and analysis of beam specimens. This procedure can be used as a design methodology. The

correlation of material properties with simplified response of a series of TRC composites with individual and hybrid textiles are shown.

2.1 Constitutive Law for Homogenized Fiber Reinforced Concrete

The behavior of TRC systems can be predicted with a tri-linear model associated with a strain hardening tensile response. A general strain hardening tensile model, and an elastic perfectly plastic compression model as derived by Soranakom and Mobasher [18] and shown in Figure 2-1 is used to further simplify the tension stiffening model. By normalizing all parameters with respect to minimum number of variables, closed form derivations are obtained [19]. Tensile response is defined by tensile stiffness, E, first crack tensile strain ε_{cr}, cracking tensile strength, σ_{cr}, $=E\varepsilon_{cr}$, ultimate tensile capacity, ε_{tu}, and post crack modulus E_{cr}. The hardening/softening range is shown as a constant stress level $\mu E\varepsilon_{cr}$. The compression response is defined by the compressive strength σ_{cy} defined as $\omega\gamma E\varepsilon_{cr}$. Material parameters required for the simplified models are summarized as follows. Parameters, α, μ, η, ω are defined respectively as normalized tensile strain at peak strength, post-crack modulus, and compressive yield strain:

$$\alpha = \frac{\varepsilon_{trn}}{\varepsilon_{cr}},\ \eta = \frac{E_{cr}}{E},\ \omega = \frac{\sigma_{cy}}{E\varepsilon_{cr}} = \frac{\sigma_{cy}}{\sigma_{cr}} \qquad \text{Equation 2-1}$$

Applied tensile and compressive strains at bottom and top fibers, β and λ are defined as:

$$\beta = \frac{\varepsilon_t}{\varepsilon_{cr}},\ \lambda = \frac{\varepsilon_c}{\varepsilon_{cr}} \qquad \text{Equation 2-2}$$

Both strains are linearly related through the normalized neutral axis parameter, *k* by:

$$\frac{\lambda\varepsilon_{cr}}{kd}=\frac{\beta\varepsilon_{cr}}{d-kd} \quad \text{or} \quad \lambda=\frac{k}{1-k}\beta \qquad \text{Equation 2-3}$$

In order to simplify material characteristics of strain-hardening FRC and yet obtain closed-form design equations several assumptions are made. It has been shown that the ratio of compressive and tensile modulus, parameter γ, has negligible effect to the ultimate moment capacity [20]. Since in typical strain-hardening FRC, the compressive strength is several times higher than the tensile strength, the flexural capacity is mostly controlled by the weaker tension component.

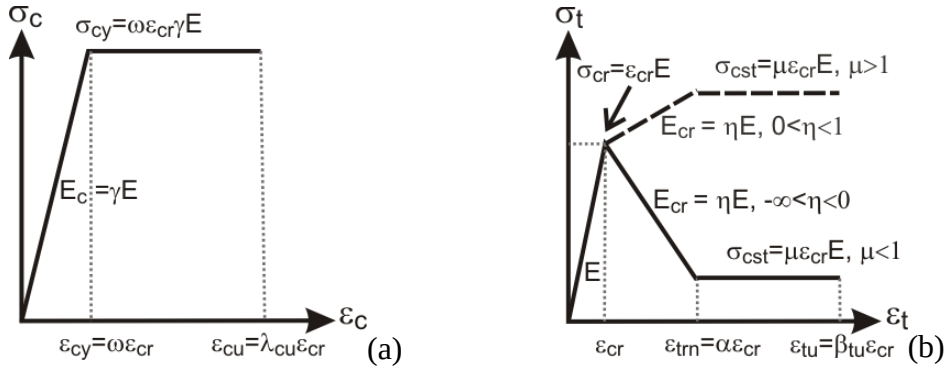

Figure 2-1 : Full option material models for both strain-hardening and strain-softening FRC: (a) compression model; and (b) tension model.

2.2 Closed Form Solutions for Moment-Curvature Relationship

Figure 2-2 shows three stages of stress strain diagrams ($0 < \beta \leq 1$, $1 < \beta \leq \alpha$ and $\alpha < \beta \leq \beta\tau_u$) as a function of the normalized bottom tensile strain β. These diagrams were used in the derivation of closed form solution for moment curvature diagram [14]. In the elastic stage 1, the stress diagram is unique as

shown in the Fig. 2(a) while stage 2 and 3 have two possible scenarios: the compressive strain at the top fiber is either elastic ($0 < \lambda \leq \omega$) or plastic ($\omega < \lambda \leq \lambda_{cu}$) and the derivations for these two stages were treated separately. The neutral axis depth ratio k is found by solving equilibrium of forces. The moment capacity is then calculated from internal forces and the neutral axis location; the corresponding curvature is obtained by dividing the top compressive strain with the neutral axis depth.

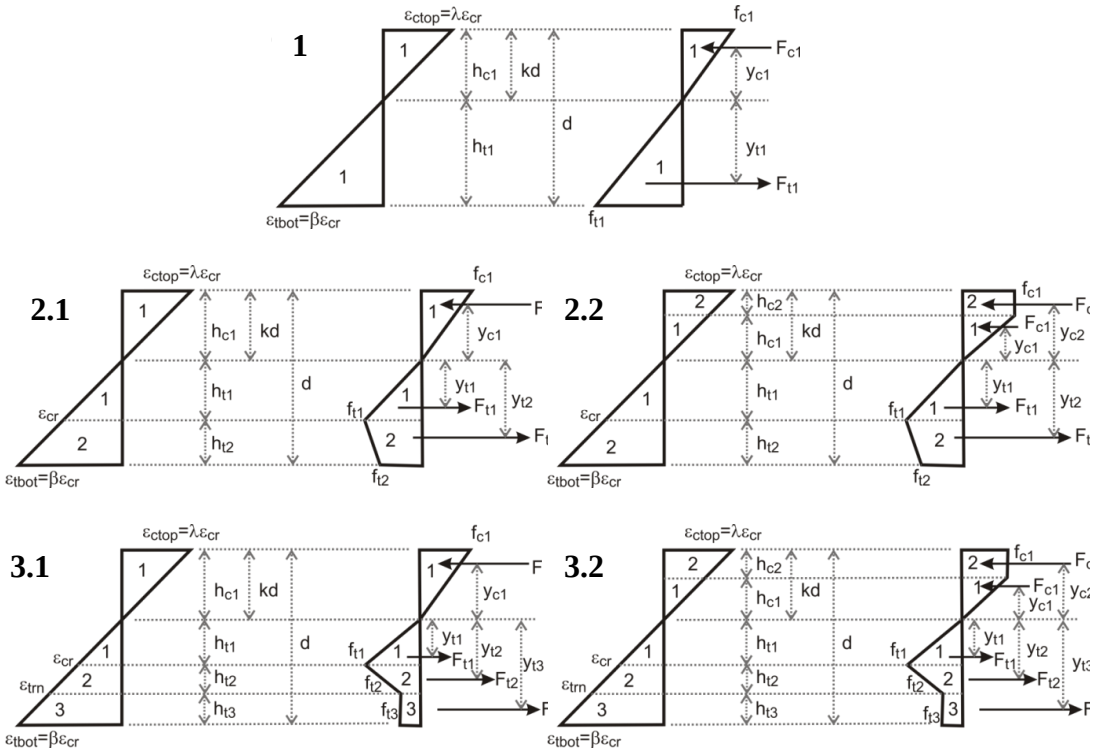

Figure 2-2 : Different stages of constitutive stress-strain diagram

Finally, the moment M_i and curvature ϕ_i for each stage i are normalized with their cracking moment M_{cr} and cracking curvature ϕ_{cr} to obtain the normalized moment M_i' and curvature ϕ_i', respectively. Expressions for calculating neutral axis depth ratio, moment and curvature are given in Table 2-1.

$$M_i = M_i' M_{cr}; \quad M_{cr} = \frac{1}{6} b d^2 E \varepsilon_{cr}$$ Equation 2-4

$$\phi_i = \phi_i' \phi_{cr}; \quad \phi_{cr} = \frac{2\varepsilon_{cr}}{d}$$ Equation 2-5

As mentioned earlier, the compressive strain at the top fiber λ in stage 2 or 3 could be either in elastic or plastic range, depending on the applied tensile strain β and neutral axis parameter k. The range can be identified by assuming $\lambda < \omega$ [Figure 2(b.1) or 2(c.1)] and using the expression k_{21} or k_{31} in Table 1 to determine λ from Equation (5). If $\lambda < \omega$holds true, the assumption is correct, otherwise $\lambda > \omega$ and the expression k_{22} or k_{32} is used instead. Once, the neutral axis parameter k and the applicable case are determined, the appropriate expressions for moment and curvature in Table 1 and Equations (6) and (7) are used.

Table 2-1 : Neutral axis depth ratio *k*, normalized moment and curvature for each stage

Stage	*k*	M_i' and ϕ_i'
1 $0<\beta\leq 1$	$k_1=\begin{cases}\frac{1}{2} & \text{for } \gamma=1\\ \frac{-1+\sqrt{\gamma}}{-1+\gamma} & \text{for } \gamma<1 \text{ or } \gamma>1\end{cases}$	$M'_1=\frac{2\beta\left[(\gamma-1)k_1^3+3k_1^2-3k_1+1\right]}{1-k_1}$ $\phi'_1=\frac{\beta}{2(1-k_1)}$
2.1 $1<\beta\leq\alpha$ $0<\lambda\leq\omega$	$k_{21}=\frac{\beta^2\gamma+D_{21}-\sqrt{\gamma^2\beta^4+D_{21}\gamma\beta^2}}{D_{21}}$ $D_{21}=\eta(\beta^2-2\beta+1)+2\beta-\beta^2\gamma-1$	$M'_{21}=\frac{(2\beta\gamma+C_{21})k_{21}^3-3C_{21}k_{21}^2+3C_{21}k_{21}-C_{21}}{1-k_{21}}$ $C_{21}=\frac{-2\eta\beta^3+3\eta\beta^2-3\beta^2-\eta+1}{\beta^2}$ $\phi'_{21}=\frac{\beta}{2(1-k_{21})}$
2.2 $1<\beta\leq\alpha$ $\omega<\lambda<\lambda_{cu}$	$k_{22}=\frac{D_{22}}{D_{22}+2\omega\gamma\beta}$ $D_{22}=\eta(\beta^2-2\beta+1)+2\beta+\omega^2\gamma-1$	$M'_{22}=(3\omega\gamma+C_{22})k_{22}^2-2C_{22}k_{22}+C_{22}$ $C_{22}=\frac{2\eta\beta^3-3\eta\beta^2+3\beta^2-\omega^3\gamma+\eta-1}{\beta^2}$ $\phi'_{22}=\frac{\beta}{2(1-k_{22})}$
3.1 $\alpha<\beta<\beta_{tu}$ $0<\lambda<\omega$	$k_{31}=\frac{D_{31}-\sqrt{\gamma\beta^2D_{31}}}{D_{31}-\beta^2\gamma}$ $D_{31}=\eta(\alpha^2-2\alpha+1)+2\mu(\beta-\alpha)+2\alpha-1$	$M'_{31}=\frac{(C_{31}-2\beta\gamma)k_{31}^3-3C_{31}k_{31}^2+3C_{31}k_{31}-C_{31}}{k_{31}-1}$ $C_{31}=\frac{3(\mu\beta^2-\mu\alpha^2-\eta\alpha^2+\alpha^2)+2\eta\alpha^3+\eta-1}{\beta^2}$ $\phi'_{31}=\frac{\beta}{2(1-k_{31})}$
3.2 $\alpha<\beta<\beta_{tu}$ □<□≤□_c *u*	$k_{32}=\frac{D_{32}}{D_{32}+2\omega\gamma\beta}$ $D_{32}=\omega^2\gamma+\eta\alpha^2+2(\mu\beta-\eta\alpha-\mu\alpha+\alpha)+\eta-1$	$M'_{32}=(C_{32}+3\omega\gamma)k_{32}^2-2C_{32}k_{32}+C_{32}$ $C_{32}=\frac{3(\mu\beta^2-\mu\alpha^2-\eta\alpha^2+\alpha^2)+2\eta\alpha^3-\omega^3\gamma+\eta-1}{\beta^2}$ $\phi'_{32}=\frac{\beta}{2(1-k_{32})}$

2.3 Crack Localization Rules and Load Deflection Prediction

Steps in calculation of load-deflection response from the moment-curvature have been discussed in detail in recent publications dealing with strain hardening [21] and softening type composites [22].Figure 2-3(a) shows a schematic drawing of four point bending test with localization of smeared crack that occurs in the mid-zone; while the zones outside the cracking region undergo unloading during softening [23,24]. The length of the localized zone is defined as "cS" representing product of a normalized parameter *c* and loading point spacing S=L/3, where *L* is the clear span. For the simulations of GFRC in this chapter, it was assumed that cracks were uniformly distributed throughout the mid zone and a value of c=0.5 was used.

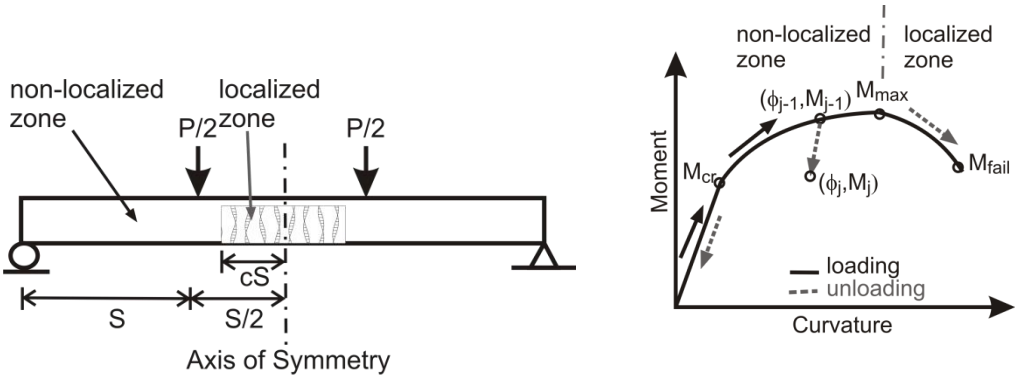

(a) (b)

Figure 2-3 **:** (a) Four point bending test, (b): Moment curvature response and crack localization rule

The curvature distribution in a beam specimen for a half-model according to the internal moment is divided into several areas. The load–deflection response

of a beam can be obtained by using the moment–curvature as shown in Figure 2-4, and the moment-area method as follows:

Steps 1 - For a given cross section and material properties, the normalized tensile strain at the bottom fiber β is incrementally imposed to generate the moment–curvature response using the expressions given in table 1. For each value of β in stage 2 and 3, the condition for compressive stress $\lambda < \omega$ or $\lambda > \omega$ is verified in advance of moment–curvature calculation as shown in Figure 2-4.

Step 2 - The moment-curvature response determines the maximum load allowed on a beam section, the discrete moment magnitudes are used to calculate the applied load vector $P = 2M/S$. Where S is a spacing between the support and loading point, $S=L/2$ for three point bending and $S=L/3$ for four point bending as shown in Figure 2-4.

Step 3 - The beam is segmented into finite sections. For a given load step, static equilibrium is used to calculate moment distribution along the beam and moment–curvature relationship along with crack localization rules to identify the curvature.

Step 4 - The deflection at mid-span is calculated by numerical moment-area method of curvature distribution between the support and mid-span. This procedure is applied at each load step to until a complete load deflection response is obtained.

The general profile of moment curvature response as shown in Figure 2-4 assumes that the contribution of fibers is in the post cracking tensile region, where the response continues to increase after cracking. Parametric Analysis of these

equations indicates that the response governed by the post-crack modulus E_{cr} is relatively flat with values of η = 0.0 - 0.4 for a majority of cement composites. The tensile strain at peak strength ε_{trn} is relatively large compared to the cracking tensile strain ε_{cr} and may be as high as α = 100 for polymeric based fiber systems. Such a characteristic response causes the flexural strength to continue to increase after cracking. Since typical strain-hardening FRC may not have a significant post-peak tensile strength, the flexural load carrying capacity drops after passing the tensile strain at peak strength (ε_{trn}). Furthermore the effect of post crack tensile response parameter μ may be ignored for a simplified analysis. In the most simplistic way, one needs to determine two parameters in terms of post crack stiffness η and post crack ultimate strain capacity α to estimate the maximum moment capacity for the design purposes [1].

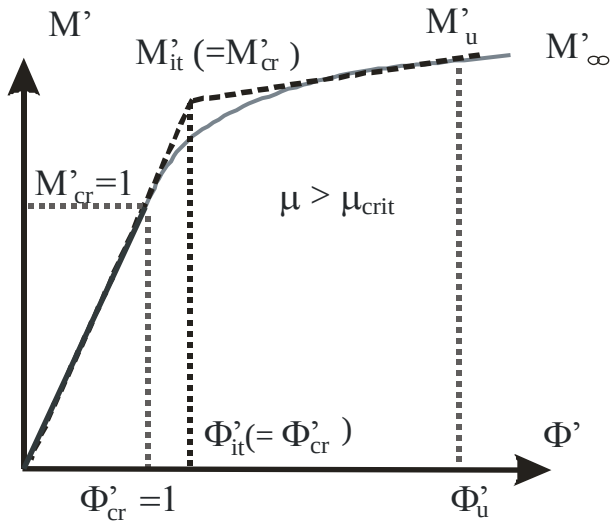

Figure 2-4 **:** Moment-Curvature relationship of strain-hardening FRC and its bilinear idealization.

The mid-span deflection is obtained directly using the double integration of curvature distribution, or by closed form solution of bilinear moment curvature response. A set of equations for calculating the mid-span deflection (δ) of the three-point bending at the first cracking (δ_{cr}), at ultimate (δ_u) under the condition of $\mu>\mu_{crit}$ are presented in .

Table 2-2.

Table 2-2 : Equations for calculating deflection at mid-span

Deflection	Four-point bending	Three-point bending
Elastic region	$\delta_{cr} = \frac{23}{216} L^2 \varphi_{cr}$	$\delta_{cr} = \frac{1}{12} L^2 \varphi_{cr}$
$\mu>\mu_{crit}$ Deflection hardening	$\delta_u = \frac{L^2}{216}\left[a_1\varphi_u + a_2\varphi_{cr}\right]$, $b = \frac{M_{cr}}{M_u}$, $a_1 = 23 - 4b - 4b^2, \quad a_2 = 4 + 4b$	$\delta_u = \frac{L^2}{24}\left[a_1\varphi_u + a_2\varphi_{cr}\right]$, $b = \frac{M_{cr}}{M_u}$, $a_1 = 2 - b - b^2, \quad a_2 = 4 + b$
$\mu<\mu_{crit}$ Deflection hardening/softening	$\delta_u = \frac{5L^2\varphi_u}{72} + \frac{M_u L^2 \varphi_{cr}}{27 M_{cr}}$	$\delta_u = \frac{\varphi_u L_p}{8}\left(2L - L_p\right) + \frac{M_u \varphi_{cr} L}{12 M_{cr}}\left(L - 2L_p\right)$

2.4 Experimental Plan

The mechanical performance of four different warp mono-fabric knitted textiles was examined. Two types of composites were studied: (i) mono-fabric high modulus fiber composites and (ii) hybrid composites as shown in Table 2-3. Hybrid composites were made with a combination of different yarns of low and high modulus within a single fabric. Aramid, carbon, and AR glass yarns were used as the high strength/high stiffness systems and polypropylene yarns were selected as low strength systems. The response of these composites was

evaluated individually. Attention was then focused on the effect of hybrid composites. Here the aramid system was chosen and different levels of aramid yarns were replaced with polypropylene yarns, providing a single multi-layered fabric with combination of those two yarns. This was in order to evaluate if a combination of low stiffness fibers in the presence of high stiffness fibers can provide a level of reinforcement that is comparable to 100% systems, i.e., fabrics with only one yarn type. The results of 100% systems. i.e., individual aramid, carbon, glass, and polypropylene fabrics, and the aramid-polypropylene hybrid system with the two yarns componation within a single fabric are discussed here.

Two sets of laminated cement boards were prepared: (i) single (mono) fabric board made from 4 layers of the single yarn type; and (ii) hybrid sandwich board using combination of aramid and polypropylene yarns. All the fabric boards were made of four layers of fabric embedded in a cement paste with water-cement ratio of 0.4. Pultrusion technique was used to manufature these composites. Aramid and polypropylene yarns were combined in a single fabric, located along the longitudinal direction of the fabric (warp direction). Different hybrid combinations of the aramid-polypropylene hybrid yarns were investigated with ratios of: 100:0, 75:25, 50:50, 25:75, 0:100 %, aramid (A) - polypropylene (P) respectively, providing five different combinations of fabrics. The fabrics and the related composites will be referred here as follows: 100A, 75A25P, 50A50P, 25A75P and 100P. In order to achieve such yarn ratios, four warp yarns were alternated within the fabric, having the formation of: A-A-A-A, A-A-A-P, A-P-A-P, A-P-P-P, P-P-P-P.

In the hybrid composition, the aramid fiber yarns were with a 322 Tex and the polypropylene with 444 Tex. In all fabrics the weft yarns (perpendicular to the loading direction) were AR glass with 1200 Tex. The stitches connected the yarns together to a fabric form were of polypropylene with 16.7 Tex. The reinforcing (warp) yarns were inserted in a two in two out formation, e.g., two yarns are as a pair and then two empty spaces, alternately. The weft yarns were inserted in a one in one out formation. Both warp and weft yarns were made from multifilament bundle. All specimens were prepared by the pultrusion process [14]. The tensile behavior of the composites was studied using closed loop uniaxial tension tests. The effect of various fabric types in suppressing the localization and crack bridging mechanisms as well as the microstructure were studied.

Table 2-3 **:** Experimental data used for back-calculation

Data Set	Type	Details of System
1	100 % Systems	Aramid
2		Carbon
3		Glass
4		Polypropylene
5	Hybrid Systems	25% Aramid – 75% Polypropylene
6		50% Aramid – 50% Polypropylene
7		75% Aramid – 25% Polypropylene

Tensile stress-strain of composites were studied using uniaxial tension tests conducted on a closed loop control MTS testing machine with a capacity of 89KN. The rate of cross head displacement was set at 0.008 mm/sec. Metal plates

with dimension of 25x50 mm and 1 mm thick were glued on the gripping edges of the specimen to minimize localized damage and allow better load transfer from the grips. Samples were held using hydraulic grips operated at low pressure to avoid localized crushing. Six replicate samples of each category were tested under flexure and tension. Results in Table 2-4 and Table 2-5 reflect the average and standard deviation values. All the specimens were of dimensions 250 (L) x 30 (B) x 9 (D) mm. For tension experiments, free length between the grips of the specimen (gage length) was maintained as 150 mm. Typical stress-strain curves representing the tensile behavior of individual composites were chosen for comparison. The flexural specimens were tested under a three point bending configuration with a clear span of 220 mm, with 15 mm of overhang on each side of the supports. Flexural load-deflection curves were drawn and used for comparison between individual composites. Based on these curves the average maximum tensile and flexural strength and toughness (area under stress-strain curve) were calculated.

Table 2-4 : Average experimental flexural data of representative TRC samples

Specimen Code		Stress at 1st Crack	Max Flex Load	Defl. at Max Flex Load	Defl. Capacity	Flexural Toughness	Flexural Stiffness	Flex. Strength, MOR
		MPa	N	mm	mm	N-mm	N/mm	MPa
100 % Aramid	Average	5.9	338	18.8	23.0	4035	47	46.9
	Std. Dev.	1.8	82	2.4	4.0	832	24	14.3
100 % Carbon	Average	8.3	509	9.1	21.7	5061	63	64.3
	Std. Dev.	1.6	76	1.5	0.3	1349	19	6.3
100 % Glass	Average	2.3	180	2.3	14.0	495	139	17.0
	Std. Dev.	0.6	30	0.5	1.3	41	46	3.6

Specimen Code		Stress at 1st Crack	Max Flex Load	Defl. at Max Flex Load	Defl. Capacity	Flexural Toughness	Flexural Stiffness	Flex. Strength, MOR
		MPa	N	mm	mm	N-mm	N/mm	MPa
100 % Polypropylene	Average	3.0	89	32.7	32.9	2026	97	12.2
	Std. Dev.	0.8	8	8.3	8.2	789	17	1.7
75 % Aramid + 25 % Polypropylene	Average	9.1	405	21.5	29.4	5673	48	60.7
	Std. Dev.	3.3	119	3.8	0.2	1593	18	20.4
50 % Aramid + 50 % Polypropylene	Average	5.1	316	21.9	29.6	5495	88	44.3
	Std. Dev.	1.3	60	2.9	0.0	1537	38	8.1
25 % Aramid + 75 % Polypropylene	Average	4.5	214	22.9	29.6	3778	66	31.2
	Std. Dev.	1.8	52	3.7	0.1	567	19	7.0

Table 2-5 : Average experimental tension data of representative TRC samples

Specimen code		Cracking Load	Stress at 1st Crack	Maximum Load	Displacement at Max Load	Stiffness	Tensile Strength
		N	MPa	N	mm	N/mm	MPa
100 % Aramid	Average	286.2	1.0	7086	4.1	16642	25.9
	Std. Dev.	89.9	0.5	589	0.4	7149	3.1
100 % Carbon	Average	360.9	1.3	22207	2.9	35947	79.5
	Std. Dev.	153.0	0.8	2097	0.4	16887	10.7
100 % Glass	Average	398.7	1.3	2077	0.9	2521	6.6
	Std. Dev.	161.2	0.5	362	0.2	466	1.1
100 % Polypropylene	Average	404.8	1.5	3047	18.3	8340	11.7
	Std. Dev.	213.1	0.8	834	4.1	2712	3.1
75%Aramid+25 % Polypropylene	Average	175.9	0.6	5595	3.9	15900	20.5
	Std. Dev.	95.5	0.4	1460	0.5	10909	6.5
50%Aramid+50 % Polypropylene	Average	200.3	0.7	3986	3.9	23171	14.8
	Std. Dev.	68.4	0.2	813	0.3	5691	2.8
25%Aramid+75 % Polypropylene	Average	303.8	1.2	2883	8.3	10231	11.0
	Std. Dev.	96.7	0.3	507	10.1	6682	1.7

2.5 Analysis - Prediction of Load Deflection Response of Fabric Cement Composites

Upper and lower bound mechanical properties of different TRC composites were documented [1]. In order to correlate the responses, experimental data from a set of specimens under uniaxial tension and three point bending tests were used. No attempt was made to obtain a best fit curve to the flexural or tensile response. The material parameters for the tension model were determined by fitting the hardening model to both the uniaxial tension test and flexural test. The result is shown by the simulated upper and lower bounds encompassing all the selected composites. Figure 7a shows the predicted flexural load deflection response of cement composites and Figure 7b shows the tensile stress-strain responses used in the simulation compared with experimentally obtained results. These key parameters α, η, and μ are changed to fit the experimental load-deflection and obtain the predicted tensile stress strain curves. There are two ways to accomplish the curve fitting, forward calculation using tension data and back-calculation using the flexural data. In the present approach only the back-calculation approach is used, however since independent tension data are also available, this enables an independent verification of the back calculation models. Simulations that use direct tension data to calculate the flexural response tend to underestimate the equivalent flexural stress. This is due to several factors including the size effect, uniformity in tension loading vs. the linear strain distribution in flexure, and variation in lamina orientation which may lead to a wider range of variation among the flexural samples. In addition

phenomenological effects such as fiber matrix de-bonding which leads to inefficient fiber performance can also lead significantly to the differences between the tensile and flexural response. In a tension test, the textile phase is held, often quite tightly in the grips, whereas in a flexural test, due to the high transverse shear loads, the end of the sample may easily de-bond, thus resulting in inefficient load transfer and thus low flexural values. These issues contribute to the performance characterization of these systems since a majority of the loading is primarily through the flexural loading mode. On the other hand flexural tests may overestimate the tensile results primarily due to the size effect. The underestimation of the flexural capacity can be addressed by increasing the apparent tensile capacity using scalar scaling parameters as discussed earlier [21]. These topics are not beyond the scope of present work, however, proper characterization of the observed differences between test methods points out the differences that are not captured using data reduction techniques. The procedure for the use of the flexural response to develop a moment-curvature response based on back-calculation however provides a potential way where the flexural results can be applied to the design of flexural load cases.

2.5.1 100 % Systems

Figure 2-5 represents the experimental and simulation of flexural load deflection results of single fiber type for the aramid textiles. The load versus deflection response based on the experimental values and the simulated fit of the data matches the experimental response. The overall fits are good; the discrepancies could be because of the variation between the individual test results.

Representative properties for the simulation of upper and lower bound values obtained from the 100 % Aramid specimens were: E = 2900 – 5900 MPa, α = 18 – 90, μ = 7 – 14, η = 0.07 – 0.76, ε_{cr} = 400 – 970 μstr. The constants were γ = 1, and ω = 11. The limits of the modeling were β_{tu} = 23 – 105 and λ_{cu} = 71. As clearly evident, there is a direct correlation between samples that show a low flexural response and their associated lower than normal constitutive models.

Tensile stress-strain responses are shown in Figure 7b which exhibits the back calculated tension response from the flexural data and compares them with the experimentally obtained tension response. Note that the initial linear portion of the curve is not well captured since the experimental data were not collected using strain gages to record the first crack strain accurately. The model however is quite accurate in predicting the overall post crack stiffness, stress capacity, strain capacity, and ductility response of the tensile samples.

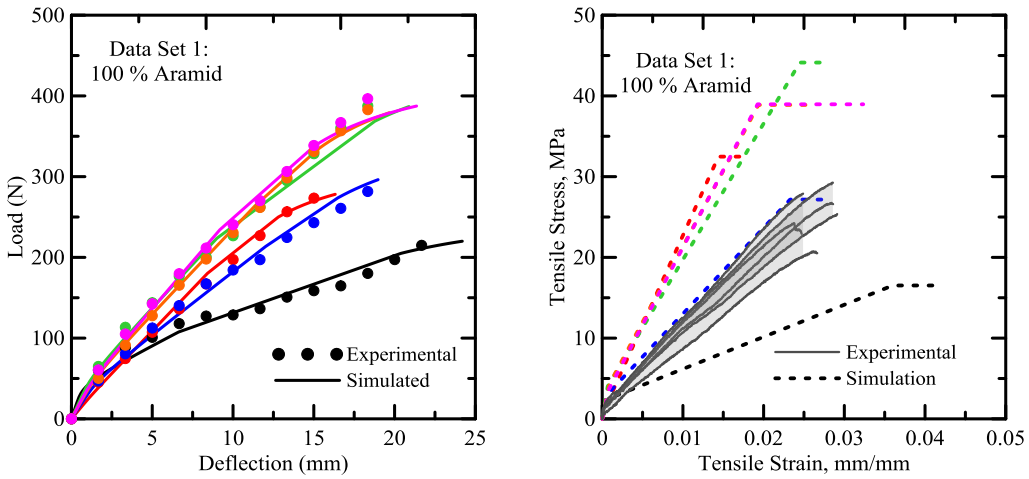

Figure 2-5 : 100 % Aramid; (a) Flexural, (b) Tension responses

The results of carbon fibers are shown in Figure 2-6(a) which shows the flexural load vs. deflection for both experimental and simulated responses. Figure

2-6(b) shows the back-calculated tension results compared with the experimentally obtained data. While it is clearly possible to fit the experimentally flexural tests, the resulting back-calculated tension response significantly underestimates the experimental response. This may be attributed to the differences in the actual bond mechanisms that are operative in the two tests. In the flexural tests, the load transfers to the carbon yarns through the interfacial zones in order to carry the load. Due to the weak bond properties of carbon systems, the capacity is rather low. In the tension test the carbon fibers are effectively clamped, therefore the load carries into the fibers quite efficiently. This explains why the tension results of carbon composites are superior to the other textile systems. The experimental tensile stress is about 40 MPa whereas the simulated tensile strengths are as high as 90 MPa. These responses are however characteristic of the carbon yarn response and though not the response of the overall composite, a loading condition that is not attainable in a flexural test. The lower and upper bound values of the representative material properties for the 100 % Carbon specimens were: E = 6000 – 8500 MPa, α = 5 – 18, μ = 7 – 9, η = 0.41 – 1.50, ε_{cr} = 660 – 1000. The constants were γ = 1, and ω = 11. The limits of the modeling were β_{tu} = 11 – 21 and λ_{cu} = 71. Values shown are for a preliminary set of data and proper model optimization with upper and lower bound values for each variable are required. The results of AR-glass fibers are shown in Figure 2-7 which shows the flexural load vs. deflection for both experimental and simulated response. In this case the results of the tension back-calculated response and experimentally obtained tension responses are shown in Figure 9b. The back

calculated tension response in this case demonstrate a much stiffer response than the experimentally obtained values, although the strength of the samples is rather comparable between the experimental and back-calculated values. The back-calculated strain capacity is between 0.1 - 0.3% whereas the experimentally obtained strains are in the range of 0.5 - 0.8%. Clearly the slip effects that takes place in the clamping of the tension fibers is important since not all the fibers are loaded due to the yarn effect. In addition any type of yarn curvature or misalignment reduces the initial stiffness of the tension samples whereas due to the imposed curvature in the flexural test, more filament to filament interaction is expected in flexure. The representative material properties and their range for 100 % AR Glass specimens were: E = 7200 – 11000 MPa, α = 10 – 20, μ = 5 – 8, η = 0.21 – 0.44, ε_{cr} = 115 – 180. The constants were γ = 1, and ω = 11. The limits of the modeling were β_{tu} = 5 – 8 and λ_{cu} = 71.

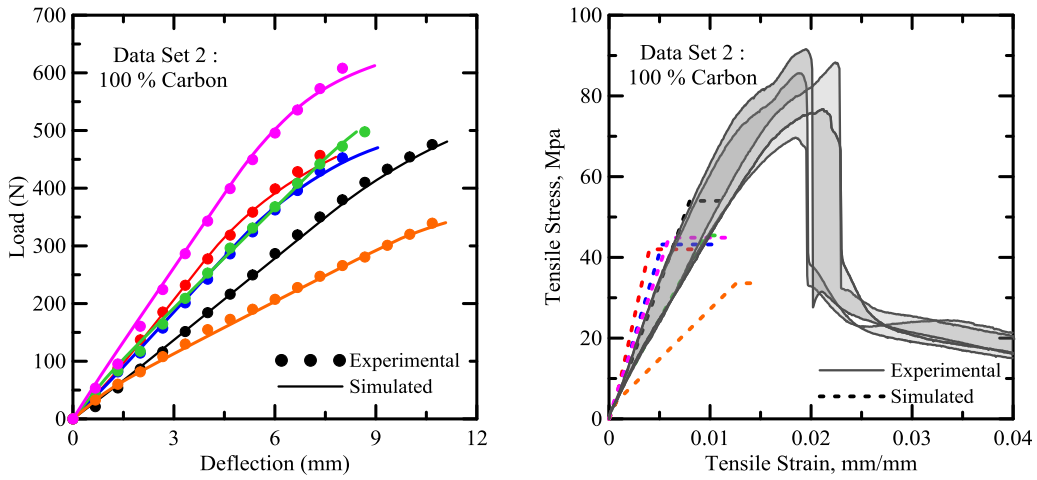

(a) (b)

Figure 2-6 : 100 % Carbon; (a) Flexural, (b) Tension responses

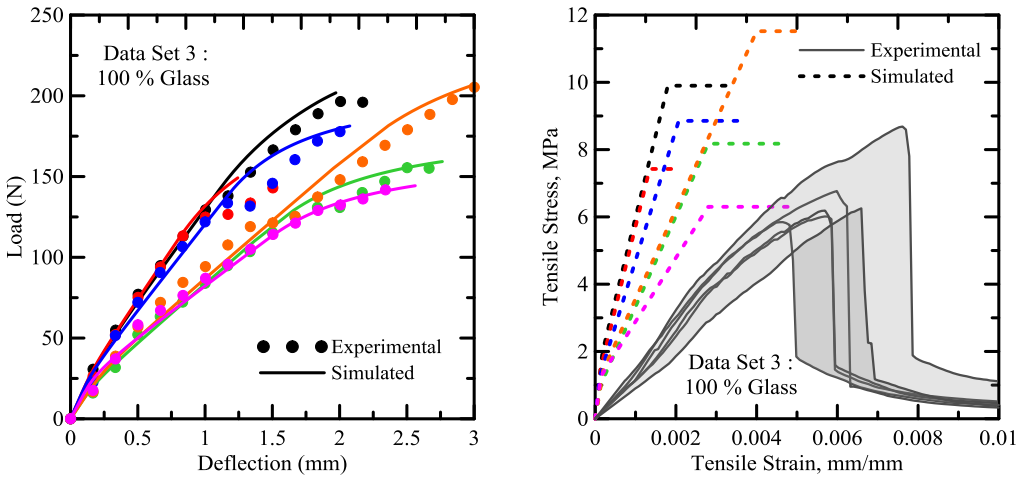

Figure 2-7 : 100 % Glass; (a) Flexural, (b) Tension responses

Results of polypropylene fabrics are shown in Figure 2-8. As evident, the model underpredicts the tension response for these fabrics. The simulated tensile strength is within 4 – 6 MPa, whereas the experimental tensile response is in the range of 10 – 15 MPa. The range of material properties for 100 % AR Glass specimens obtained from the simulations were: E = 5800 – 8200 MPa, α = 165 – 275, μ = 8 – 9, η = 0.007 – 0.012, ε_{cr} = 190 – 335. The constants were again γ = 1, and ω = 11. The limits of the modeling were β_{tu} = 200 – 400 and λ_{cu} = 71.

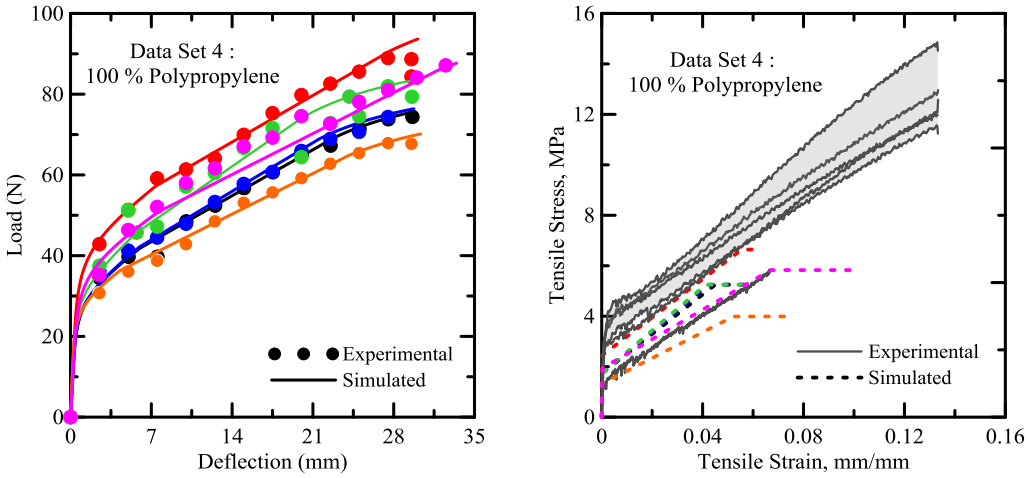

(a) (b)

Figure 2-8 : 100 % Polypropylene; (a) Flexural, (b) Tension responses

A comparison of the response of the 100% systems is shown in Figure 2-9. Note that the carbon fiber system shows an exceedingly high tensile response however the flexural capacity is only shown by the high stiffness as compared to the glass, aramid and polypropylene. The polypropylene system shows the lowest flexural stiffness, largest deflection among the systems studied. The comparison of the tension simulated and experimental tensile responses indicate that the largest discrepancy can observed in the results obtained for the carbon fibers followed by the aramid, glass and polypropylene respectively. The back-calculated values for the aramid and glass are both in the same response range; however both methods overestimate the post cracking stiffness in these systems with an average tensile strength of 30 and 10 MPa respectively.

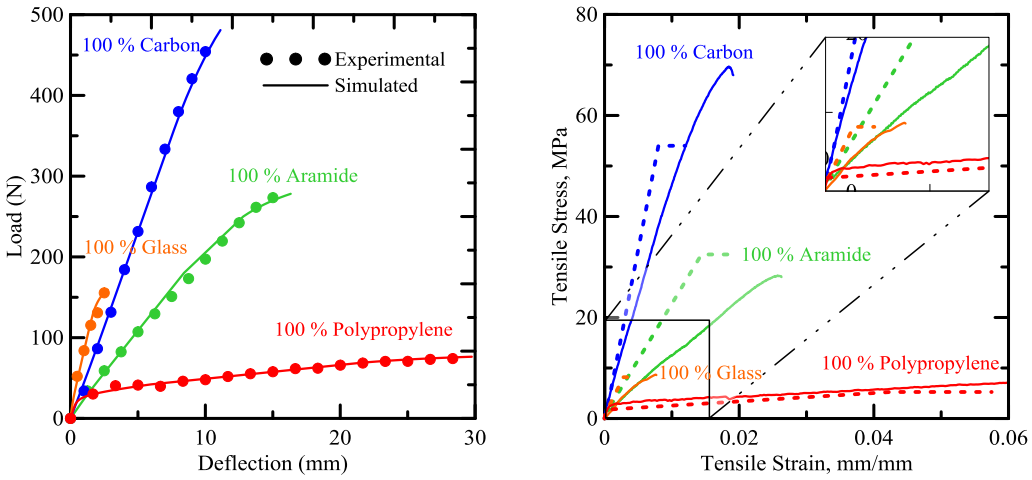

(a) (b)

Figure 2-9 : Comparison between 100 % systems; ; (a) Flexural, (b) Tension responses

2.5.2 Polypropylene – Aramid Hybrid Systems

Results of hybridization are shown in Figure 2-10 - Figure 2-12. Figure 2-10(a) shows the flexural load vs. deflection for both experimental and simulated response of 75A25P samples. Comparison of the back-calculated tension and experimentally obtained tension responses are shown in Figure 2-10(b). The back calculated tension response in this case demonstrates a stiffer response than the experimentally obtained values, with a slightly higher strength of the samples. There is however a good correlation between the experimental and back-calculated values. The back-calculated strain capacity is about 0.2-0.3% whereas the experimentally obtained strains are in the range of 0.2-0.4%.

Results of 50A50P and 25A75P are shown in Figure 2-11 and Figure 2-12. In both these systems it is shown that the combination of the two yarns helps with the general behavior of the composite and there is a change in the response based

on the overall stiffness reduction by replacing a stiff fiber with a more compliant fiber system.

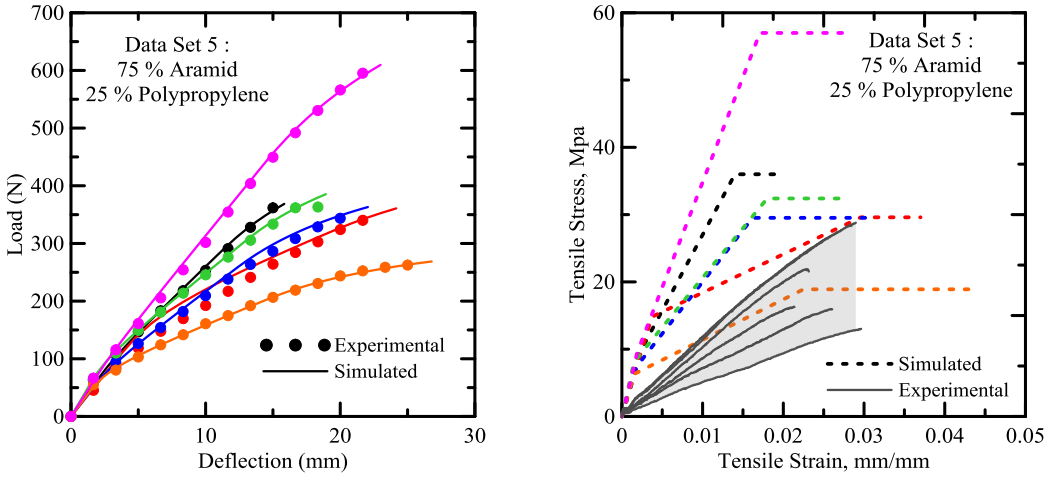

(a) (b)

Figure 2-10 : Hybrid of 75 % Aramid + 25 % Polypropylene; (a) Flexural, (b) Tension responses

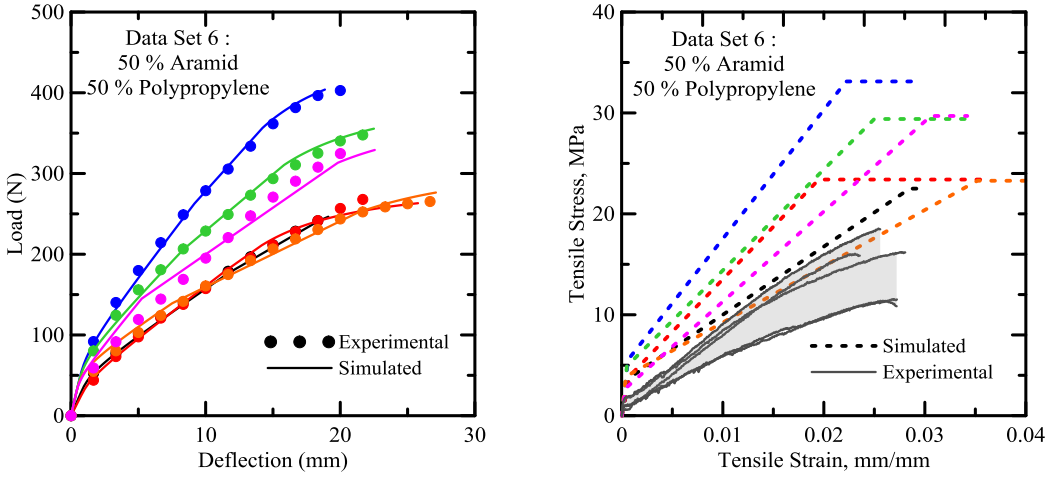

(a) (b)

Figure 2-11 : Hybrid of 50 % Aramid + 50 % Polypropylene; (a) Flexural, (b) Tension responses

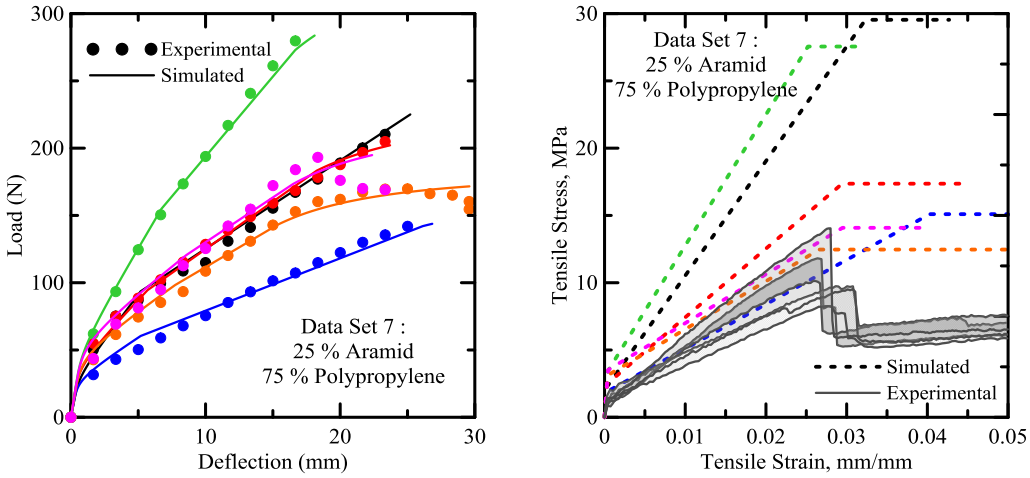

(a) (b)

Figure 2-12 : Hybrid of 25 % Aramid + 75 % Polypropylene; (a) Flexural, (b) Tension responses

Comparison between polypropylene – aramid hybrid systems is shown in Figure 2-13. Note that the gradual change in the stiffness is clearly shown and the proposed approaches can be used to generate the desired stiffness of the samples by properly aligning the yarns and optimizing the response in accordance to the required stiffness of the sample. As expected aramid fabrics introduce higher strength and stiffness to the composites. Polypropylene textiles however have significant lower flexural and tensile strength. Hence when the composition of the hybrid composites is modified, changes in the stiffness and strength can be observed in the expected lines. As the aramid content in the hybrid composition is reduced from 75 % to 25 %, about 50 % reduction in the load carrying capacity can be observed. Effect on tensile strength is however insignificant.

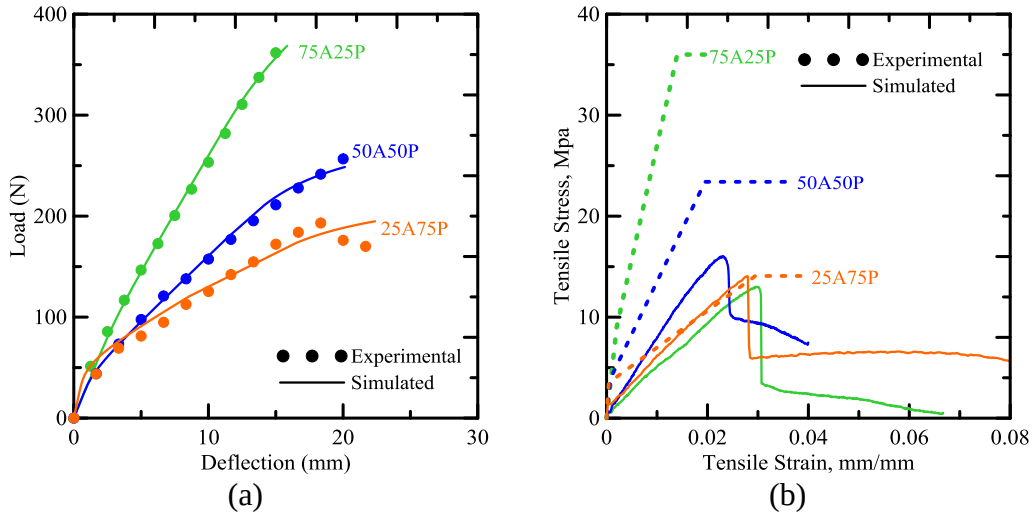

Figure 2-13 : Comparison between hybrid systems of Aramid and Polypropylene

Comparison between model parameters is shown in Figure 2-14. Note that by developing these responses, one can develop proper design tools so as to customize the appropriate material properties for a given design. With the ability to weave three dimensional, it is possible to utilize a unique textile configuration for a given loading criteria. Effect of yarn proportion (X) on the back calculated tension responses in terms of elastic modulus, post crack stiffness, the first cracking strain, and ultimate strain of hybrid aramid-polypropylene fiber combinations are shown. Effect of hybridization on elastic modulus, E of aramid-polypropylene composites is shown in Figure 2-14(a). Changes in material parameter, η is shown in Figure 2-14(b). An increasing trend could be seen starting from 100A specimens and continue to increase up to 100P specimens. A contrasting trend could be seen in Figure 2-14(c), with maximum transition tensile strain, α can be observed 100P specimens, indicating an increase in strain capacity. Hence with the reduction in the content in polypropylene in hybrid

composition, transition tensile strain, α continues to decrease. First cracking tensile strain values of these fabric combinations are shown in Figure 2-14(d).

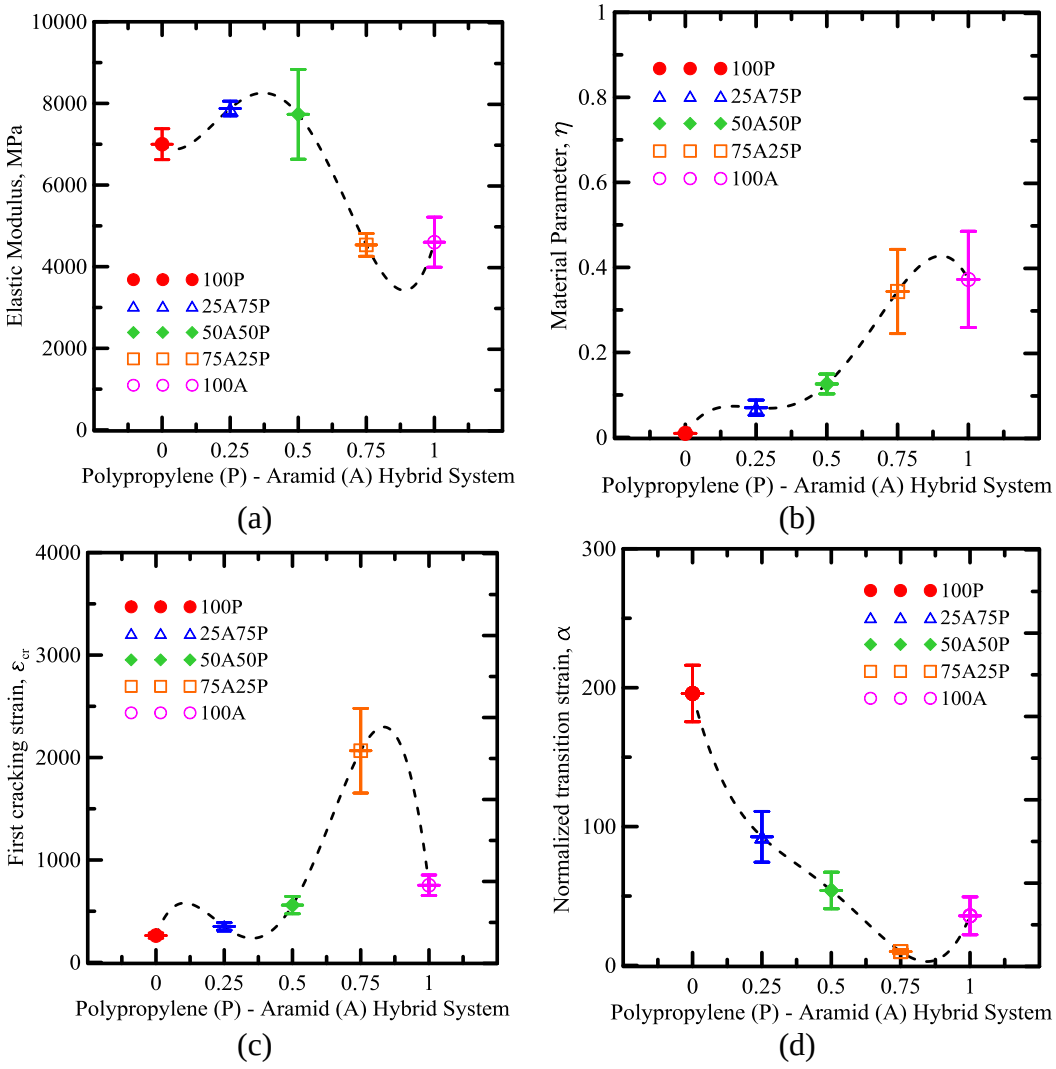

Parameter	Polynomial Fit Equation	R^2 value
E	$E = 7000 - 5556 * X + 69556 * X^2 - 155644 * X^3 + 89244 * X^4$	0.6
η	$\eta = 0.0097 + 0.99 * X - 5.16 * X^2 + 10.04 * X^3 - 5.51 * X^4$	0.6
ε_{cr}	$\varepsilon_{cr} = 262.5 + 6988 * X - 47328 * X^2 + 97338 * X^3 - 5650\ 7 * X^4$	1
α	$\alpha = 195.83 - 779.69 * X + 2137 * X^2 - 3064 * X^3 + 1546 * X^4$	1

Figure 2-14 : Comparison between Model parameters

Table 2-6 : Input parameters used for the inverse analysis of different TRC systems

Sample ID		Model Input						
		Material Parameters		Tension Model Parameters				
		E (MPa)	ε_{cr} (μstr)	α	γ	η	μ	β_{tu}
100A	Avg.	4600	753	36	1	0.37	10	44
	SD	1226	201	27	0	0.23	3	31
100C	Avg.	7050	785	10	1	0.96	8	15
	SD	952	119	5	0	0.39	1	4
100G	Avg.	9417	152	16	1	0.36	6	27
	SD	1849	32	5	0	0.08	2	8
100P	Avg.	7000	263	196	1	0.01	3	268
	SD	759	50	41	0	0.002	0	74
75A25P	Avg.	4533	2067	10	1	0.34	4	17
	SD	557	826	3	0	0.20	1	7
50A50P	Avg.	7733	560	54	1	0.13	7	69
	SD	2202	169	26	0	0.05	2	28
25A75P	Avg.	7875	352	93	1	0.07	7	130
	SD	360	73	37	0	0.04	3	44

Table 2-7 : Average values of the results from the inverse analysis of different TRC systems

Sample ID		Model Output											
		Back calculated Flexural properties							Back calculated Tensile properties				
		Stiff-ness	Defl. at 1st Crack	Strength at 1st Crack	Max Load	Defl. at Max Load	MOR	Tough-ness	Strength at 1st Crack, σ_{cr}	Transit-ion Strain, ε_{trn}	Ulti-mate Strain, ε_{tu}	Residual Strength Parameter, $\mu\sigma_{cr}$	Tough-ness
		N/mm	*mm*	*MPa*	*N*	*mm*	*MPa*	*N-mm*	*MPa*	*μstr*	*μstr*	*MPa*	*MPa*
100A	Avg.	39	0.68	3.32	327	21.01	45	5005	3.32	22793	28717	33.0	0.58
	SD	12	0.19	0.83	73	3.54	12	1725	0.83	7380	7913	10.0	0.20
100C	Avg.	63	0.70	5.49	476	7.10	61	2609	5.48	7565	11513	43.9	0.34
	SD	17	0.13	0.67	87	2.53	9	501	0.67	3175	1950	6.6	0.06
100G	Avg.	161	0.11	1.41	174	2.27	14	253	1.41	2470	4043	8.7	0.03
	SD	30	0.02	0.32	27	0.64	2	87	0.32	940	1176	1.8	0.01
100P	Avg.	57	0.24	1.83	83	33.27	11	2629	1.83	50583	68863	5.4	0.28
	SD	7	0.05	0.37	11	8.11	2	941	0.37	9799	17754	0.9	0.09
75A25P	Avg.	33	1.93	9.18	393	21.79	58	17854	9.18	19567	31100	33.9	0.74
	SD	4	0.77	2.98	114	3.89	17	32086	2.98	5659	8193	12.7	0.23
50A50P	Avg.	61	0.52	4.04	312	22.65	44	5485	4.11	26833	34767	26.9	0.62
	SD	20	0.17	0.87	61	3.36	8	1390	0.98	5755	5266	4.4	0.11
25A75P	Avg.	58	0.33	2.79	208	25.76	30	4742	2.79	30558	43318	19.3	0.56
	SD	6	0.06	0.67	54	3.46	7	1029	0.67	5378	7244	7.3	0.14

Table 2-6 and Table 2-7 summarize the input parameters used and the results obtained from the inverse analysis for 100 % systems and hybrid systems investigated in this chapter, respectively. Only average and standard deviation values of each of the parameters are reported. α and β_{tu} are unit less scalars that apply to the first crack strain, ε_{cr}. Parameters γ and η are unit less scalars that apply to the stiffness E. Parameter, μ is a unit less scalar that applies to the first crack tensile strength, σ_{cr}. The key back-calculated flexural and tension parameters (only average and standard deviation values) obtained from the inverse analysis are also mentioned.

2.6 Conclusions

The material model based on a constitutive stress-strain relationship of fiber reinforced concrete developed earlier here in Arizona State University was used to study experimental response of various TRC composites. Various alternatives of fabric material (aramid, carbon, glass, and polypropylene) were individually evaluated in terms of their flexural and tensile characteristics. An innovative idea of using hybrid type fabric combination was also investigated. Idea behind hybridization of multiple fabric layers was to obtain optimal performance of individual fabrics by combine them into a single TRC board. Prospect of using a hybrid combination of aramid (high strength) and polypropylene (cheap, low strength) was thoroughly investigated by using different proportions of these fabrics inside one composite board. Hybrid fabrics made out of aramid and polypropylene was found to significant enhance the flexural and tensile strength under static conditions when compared to mono layer polypropylene textiles.

With such an idea, different hybrid fabrics with varied ratios of constituent textiles can be manufactured to model a wide range of TRC composites constituted by brittle response to highly ductile composite with very high strain capacity. This could cater to different design requirements of structural systems.

3. MODELING OF DURABILITY OF TEXTILE AND GLASS FIBER REINFORCED CEMENT COMPOSITES

One of the key parameters in assessing the performance of cement based composites is their ability to withstand the environmental conditions imposed during service life. It is imperative that any new system developed will have sufficient long term performance that can ensure proper and sustainable life cycle. It is therefore important to use the same methodology that is used for the design of cement composites and extend the procedures developed in order to simulate both the early strength and also long term performance of the proposed systems. In this chapter the methodologies developed for back calculation of material properties are extended to develop a model for aging and durability for the response of general cement based composite systems. These models can be used in order to simulate the textile reinforced concrete as well as any other type of system that can be exposed to simulated aging conditions. While there are a significant number of experimental durability studies are available, very little analytical tools are available to simulate the durability mechanics, and develop a comparative basis for evaluation of different systems.

This chapter develops procedures for modeling the aging of cement composites for long term performance based on back calculated properties measured. The aging parameters and functions are calculated by means of model calibration using existing long term durability data that are available for GFRC. The same constitutive law for fiber reinforced concrete described in the previous chapter was used for characterization and prediction of long term flexural

behavior of GFRC materials using existing and historical data. Experimental flexural test data was back-calculated to obtain material parameters and establish their relationships with aging. The material behavior as described before is controlled mainly by three parameters: Young's modulus, first cracking strain and a normalized transitional tensile strain parameter. Once the relationships between the parameters and age were established, the time dependent flexural performance of the mixes was simulated. Test results reported by Marikunte et. al. [25] which addressed mixtures containing metakaolin, silica fume without polymers and silica fume with polymers were subjected to hot water accelerated aging at three levels (un-aged, 28, and 84 days of aging). Results reveal that addition of metakaolin and silica fume enhances the flexural strength and also reduces the deterioration of moment and ductility as material ages with time. GFRC composite containing metakaolin shows improved strength retention and durability in the long term when compared to silica fume. A similar approach was used to study the classical ageing response of GFRC composites as published by Litherland et. al. [26]. In this study the effect of accelerated ageing of GFRC in hot water at different temperatures and various durations of time was investigated.

Development of GFRC was possible with the design of a sodium-zirconium-silicate alkali-resistant (AR) glass by the Building Research Establishment (BRE) and Pilkington Brothers Ltd. in 1971. GFRC shows a reduction in strength, ductility, toughness, and impact resistance over time [27] and assuming that fiber corrosion was the main degradation mechanism, accelerated aging procedures such as the "strand in cement" (SIC) test were

developed to predict long term strength of the composite [10]. The accelerated aging tests were then compared with weathering data to obtain empirical relationships for weathering acceleration factors for a range of climatic temperatures between 5 and 80°C and [28, 29 and 30]. The relationship between time in accelerated aging (different temperatures) and exposure to weathering was proposed as a basis for testing GFRC products [30]. Further investigations established that material properties are influenced by more complex mechanisms than glass fiber corrosion, and other aging mechanisms including densification of the fiber-cement interface with time, and calcium hydroxide filling of the space between the filaments in a strand, reducing its flexibility were identified [31, 32]. In addition to strength loss, reduction in strain capacity and total ductility of GFRC composites was also noted [33,34]. Based on the identification of degradation mechanisms, development of improved long term durability of GFRC addressed modified matrices such as ground granulated blast furnace slag, silica fume [35], fly ash [36], and/or calcium aluminate or sulpho-aluminate based cements [37].

It has been observed that far fewer $Ca(OH)_2$ crystals precipitate in fiber bundles in non-OPC GFRC [27]. Sulpho-aluminate modified cements produce little, if any $Ca(OH)_2$ and in metakaolin-type matrices $Ca(OH)_2$ content is decreased [38] or precipitate away from the fibers. Fiber push out tests and microstructural studies have shown that densification within the fiber bundle does not occur with aging in GFRC metakaolin modified GFRC [39]. Both these composites have improved durability compared to traditional OPC GFRC

according to accelerated aging tests, however strength loss still occurs, to less extent though [41,39].

Glass is chemically attacked by hydration products (hydroxyl ions), leading to a break-up of the Si-O-Si glass network, which leads to a weak glass surface. Orlowsky [40] proposed a model based on physico-chemical degradation. Initial corrosion rate is linear with time, but the process slows down with increasing zirconium concentration in the deeper layer and becomes diffusion controlled. Formation of hydration products in the interface zone of a glass fiber-concrete may increase transversal shearing on the filament and lead to embrittlement (loss of ductility) and is considered as mechanical attack. It is believed [31, 32, and 27] that embrittlement due to the growth of hydration products around glass filaments, particularly $Ca(OH)_2$ crystals, occurs at an early stage of curing of the composite, which leads to loss of filament strength before the chemical attack. Delayed fracture may also occur under static load due to the introduction of small defects in the production process [43].

Variations in matrix ingredients include use of metakaolin [41,42,43] acrylic polymer [44, 45, 46], and cement types, such as sulpho-aluminate cement (SAC) [47,48,49, and[50], inorganic phosphate cement (IPC) [51,52,53, 54] and calcium aluminate cement (CAC) [55,56]. Marikunte et al. [41] studied the hot-water durability of AR-glass fiber reinforced composites in blended cement matrix and were rated for their flexural and tensile performance. Different matrices selected were (a) cement; (b) cement + 25% metakaolin; and (c) cement + 25% silica fume. Specimens after normal curing of 28 days were immersed in a

hot water bath at 50 degrees C for up to 84 days and then tested under flexural and tensile stresses. The results indicate that the blended cement consisting of metakaolin significantly improves the durability of GFRC composite. Flexural stress and strain at failure (MOR) are considered as a measure to assess durability [41].

Beddows and Purnell [42] and Purnell and Beddows [43] developed a durability model for GFRC samples including OPC I and OPC II, and GFRC with metakaolin, polymers and sulfo-aluminates and concluded that AR-glass composites with OPC+5% polymer + sulpho-aluminate based additives was the most durable of the GFRCs tested. Beddows and Purnell [42] present a comparison of acceleration factors advanced by Litherland et al. [10] and Purnell's model for OPC II and M II (matrix modified with metakaolin).

3.1 Effect of matrix ingredients in durability of GFRC composites

The aging effects on flexural and tensile mechanical responses of GFRC reported by Marikunte et. al. [25], were analyzed with the proposed model. Test was categorized on the basis of ingredients involved in mix design and curing conditions to which they were exposed. Three test series of mixes involving metakaolin (MK) and silica fume (SF - with and without polymers) are considered. Cement used was a U.S white Portland cement, the silica fume was Elkem air densified microsilica, metakaolin was Englehard Metamax, the polymer was Forton acrylic polymer and the super plasticizer was Sikament 10 and the AR-glass fiber was Cem-FIL. Table 3-1 presents the proportions of mixture

ingredients. Mixing was done inside a high shear mixer with mortar and chopped glass fibers sprayed in the mold in four crossed layers and later roller compacted.

Table 3-1: Details of test series and mixture proportions

Mix Ingredients	GFRC Mixes (in kg) A - Metakaolin (MK)	B – Silica Fume (SF 1)	C - Silica Fume (SF 2)
Cement	100	100	100
Sand	100	100	100
Metakaolin	25	-	-
Silica Fume	-	25	25
Water	44	45.9	45.9
Polymer	12.3	-	12.3
Super	3	3	3
AR Glass	5% by weight of	5% by weight of	5% by weight of

Specimens were initially exposed to normal curing for 28 days. In order to simulate the long term performance the specimens after normal curing were immersed in a hot water bath at 50 ºC. Samples were segregated and categorized further based on exposure to two levels of accelerated aging, 28 and 84 days. Four point flexural test and uniaxial tension test were then conducted to evaluate their flexural performance and tensile properties. Flexural tests were conducted on specimens of size 50 x 10 x 225 mm with a clear span of 205 mm and mid-point deflections were measured. Stress and strain corresponding to the limit of proportionality (LOP) and failure (MOR) were observed. Tension tests were conducted on notched specimen, and crack mouth opening displacement (CMOD) was measured. Flexural performances of GFRC composites at different levels of

aging were further compared to understand the effect of the mixture ingredients. Figure 3-1 (a) – (c) compares the said responses based on aging effects.

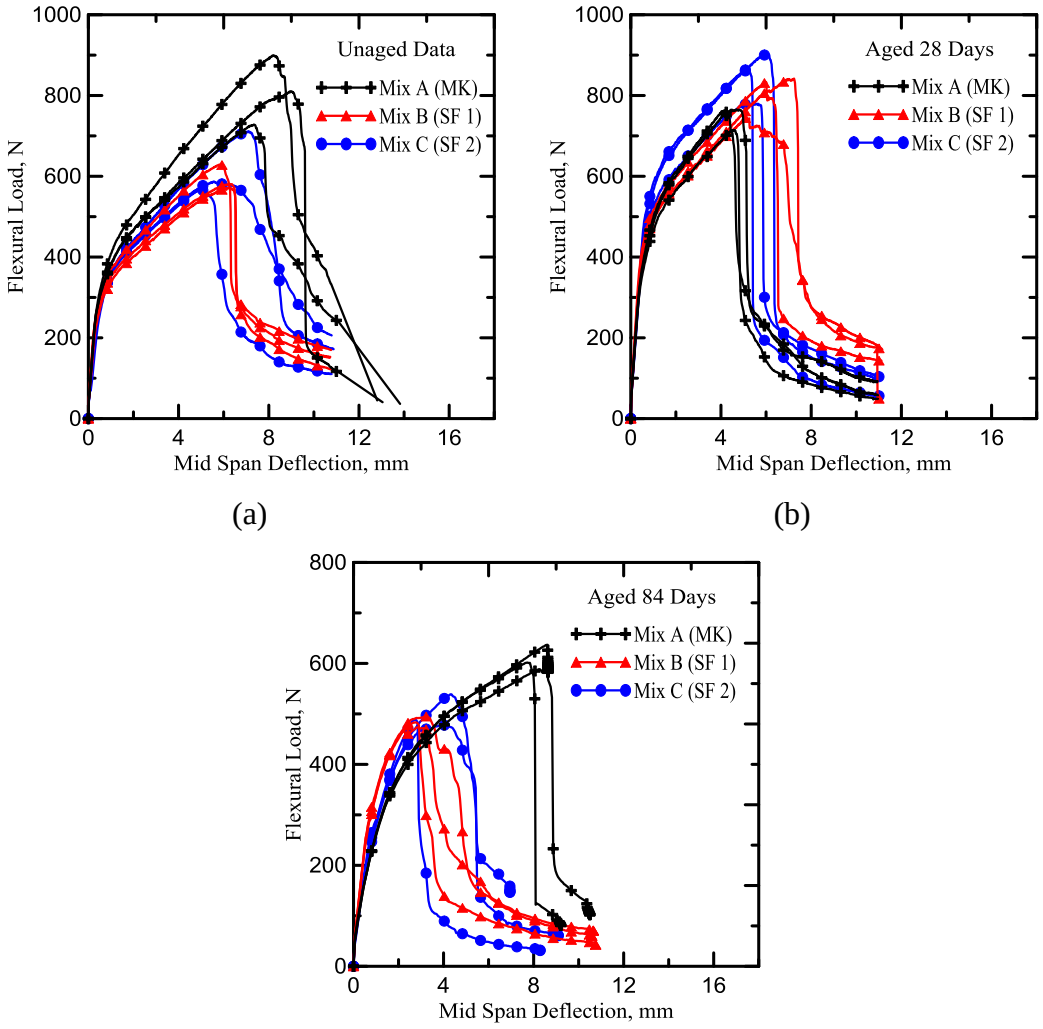

Figure 3-1 : Comparison between (a) Un-aged, (b) 28 day aging, (c) 84 day aged data

3.1.1 Inverse Analysis

Since the compressive strength of concrete materials is several times higher than its tensile strength, tensile characteristics control the flexural behavior of a beam specimen. The tensile properties of GFRC can therefore be estimated by inverse analysis from flexural response. For typical high dosage fiber GFRC

that show deflection hardening followed by brittle failure in the post peak region, it is sufficient to describe the material behavior with three parameters: Young's elastic modulus E, first cracking strain ε_{cr}, and strain at peak stress ε_{trn} (or transitional strain). The constant stress in the last post crack region σ_{cst} for all test series was assumed according to the experimental post peak response which is predominantly brittle. The compressive response was assumed in linear elastic range as compressive strength is relatively higher when compared to weaker tensile strength.

The inverse analysis was performed by first adjusting Young's modulus until the initial slopes of the predicted and experimental flexural stress deflection responses matched. Next, the first cracking strain was adjusted until the predicted post crack response matched the proportional limit (LOP) of the experiments. Finally, the strain at peak stress was adjusted until the predicted and experimental peak stresses were similar.

3.1.2 Results and Discussions

Figure 3-2 - Figure 3-4 shows the results of inverse analysis conducted on the mixes exposed to three levels of aging. With the addition of metakaolin in the mix (A), the long term flexural behavior shows very less strength reduction and durability as can be seen in Figure 3-2 - (a) and (b). The initial slope of flexural response slightly increases between un-aged and 28 days of aging and then decreases when it reaches 84 days. Drop of flexural strength from the un-aged to the age of 84 days is marginal. The ductility as defined by an area under curve decreases slightly with aging. Figure 3-2(b) reveals the inverse analysis results,

which resembles to the equivalent flexural stress but is less than an half in magnitude. This difference is due to the stress definitions assumed by each model. The equivalent flexural stress assumes a linear elastic stress distribution, having a triangular shape, for pre-crack to post-crack responses while the proposed model assumes more realistic shape of tensile stress as previously described in Figure 3-2(b).

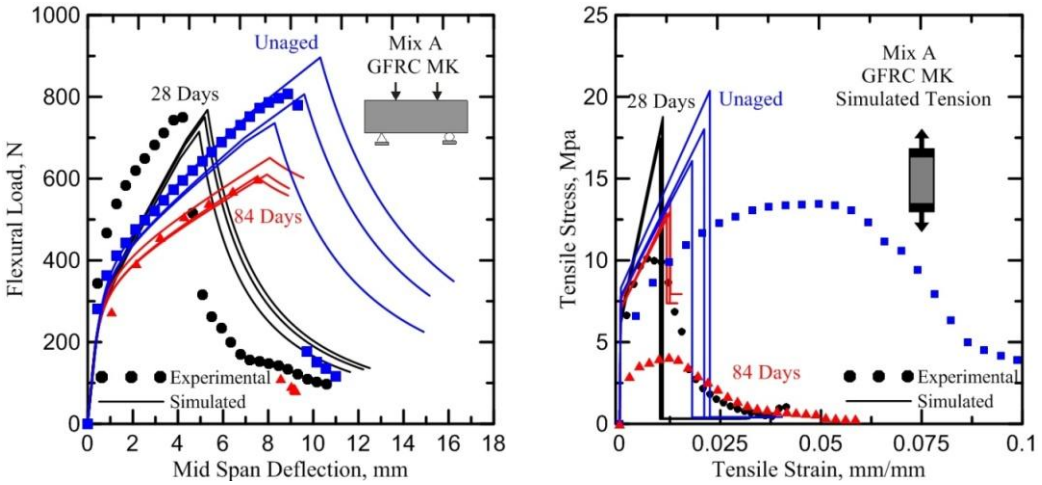

(a) (b)

Figure 3-2 (a) : Inverse Analysis of Metakaolin Mix, (b) : Backcalculated Tension Models

Addition of silica fume without any polymer in the mixture matrix (B), changes the behavior of the composite to a great extent. The long term flexural behavior shows deterioration when compared to the control mix. Figure 3-3(a) and (b) show that the 28 day samples show higher flexural strength and back calculated tensile strength, followed by the un-aged samples and 84 day samples. Addition of silica fume with polymer in the mix (C) shows similar trend as the previous case (mix B). Addition of polymers shows marginal improvement in

terms of the overall flexural and tensile behavior across all ages when compared to the mix (B) without polymer. Figure 3-4(a) and (b) show that the 28 day samples show higher flexural and tensile strength, followed by the un-aged samples and 84 day samples, similar to mix (B).

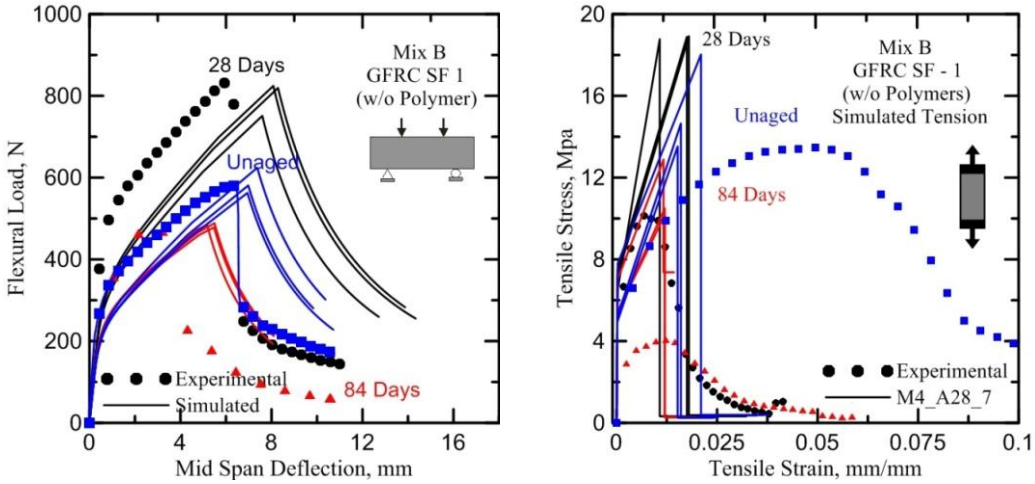

Figure 3-3 (a) : Inverse Analysis of Silica fume (SF 1) Mix B, (b):

Backcalculated Tension Models

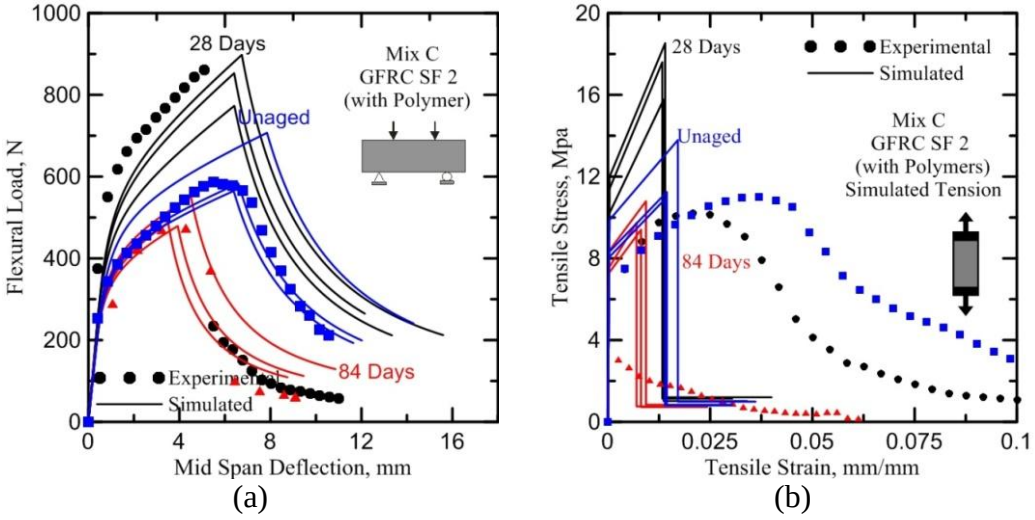

Figure 3-4 (a) : Inverse Analysis of Silica fume (SF 2) Mix C, (b) :

Backcalculated Tension Models

Parameters used in the material for simulating the performance of GFRC composites with metakaolin and silica fume are presented in Table 3-2. Flexural strength parameters calculated from the material model are presented in Table 3-3. Clearly GFRC matrix with metakaolin (mix A) has superior long-term strength retention. Enhanced load carrying capacity and toughness could be achieved only with metakaolin mixes with ageing. Insignificance of addition of silica fume in terms of long term durability of GFRC mixes is evident.

Table 3-2: Input material parameters used to model GFRC composites

Sample ID	Model Input: Material Parameters E	ε_{cr}(μstr)	α	Tension γ	η	μ	β_{tu}	Compression ω	λ
	GPa	mm/mm	mm/mm	MPa/MPa	MPa/MPa	MPa/MPa	mm/mm	mm/mm	mm/mm
Mix A (MK): Cement + 25% Metakaolin									
A28 - M3 - 07	30	280	40	1	0.039	1.05	150	12	26
A28 - M3 - 08	30	210	50	1	0.039	0.05	150	12	26
A28 - M3 - 09	30	215	50	1	0.039	0.05	150	12	26
A84 - M3 - 13	27	260	48	1	0.018	1.05	55	12	26
A84 - M3 - 14	27	280	45	1	0.019	1.05	55	12	26
A84 - M3 - 15	27	260	45	1	0.019	1.05	55	12	26
C28 - M3 - 01	26	320	70	1	0.021	0.05	126	12	26
C28 - M3 - 02	26	270	70	1	0.02	0.05	126	12	26
C28 - M3 - 03	26	300	70	1	0.019	0.05	126	12	26
Mix B (SF 1): Cement + 40% Slag + 20% NRS (w/o Polymer)									
A28 - M4 - 07	30	250	70	1	0.022	0.05	145	12	26
A28 - M4 - 08	30	240	75	1	0.022	0.05	145	12	26
A28 - M4 - 09	30	220	75	1	0.022	0.05	145	12	26
A84 - M4 - 13	27	200	60	1	0.016	0.05	100	12	26
A84 - M4 - 14	27	200	60	1	0.015	0.05	100	12	26
A84 - M4 - 15	27	200	56	1	0.017	0.05	100	12	26
C28 - M4 - 01	26	190	80	1	0.022	0.05	126	12	26
C28 - M4 - 02	26	200	80	1	0.023	0.05	140	12	26
C28 - M4 - 03	26	190	80	1	0.0205	0.05	140	12	26
Mix C (SF 2): Cement + 40% Slag + 20% NRS (with Polymer)									
A28 - M5 - 07	30	340	40	1	0.014	0.1	100	12	26
A28 - M5 - 08	30	400	35	1	0.016	0.1	100	12	26
A28 - M5 - 09	30	380	35	1	0.016	0.1	80	12	26
A84 - M5 - 13	27	310	30	1	0.01	0.1	90	12	26
A84 - M5 - 14	27	270	30	1	0.01	0.1	90	12	26
A84 - M5 - 15	27	280	25	1	0.012	0.1	80	12	26
C28 - M5 - 01	26	310	45	1	0.008	0.1	95	12	26
C28 - M5 - 02	26	320	45	1	0.008	0.1	95	12	26
C28 - M5 - 03	26	380	45	1	0.009	0.1	95	12	26

Table 3-3 : Results of the inverse analysis on GFRC composites

Inverse Analysis Output								
Sample ID	Bending Stress, MOR	Flexural Stiffness	Load at first crack	Defl. at first crack	Stress at first crack	Max Flexural Load	Defl. at Max Flexural Load	Flexural Toughness
	MPa	N/mm	N	mm	MPa	N	mm	N.mm/mm^2
Mix A (MK): Cement + 25% Metakaolin								
A28 - M3 - 07	32.163	618.36	133.33	0.22	6.0	714.74	4.94	8.60
A28 - M3 - 08	33.771	618.36	140.00	0.23	6.3	750.48	5.19	9.48
A28 - M3 - 09	34.575	618.36	143.33	0.23	6.5	768.34	5.31	9.93
A84 - M3 - 13	27.456	556.52	156.00	0.28	7.0	610.12	7.95	8.37
A84 - M3 - 14	29.288	556.52	168.00	0.30	7.6	650.85	8.07	9.68
A84 - M3 - 15	27.196	556.52	156.00	0.28	8.1	604.36	7.50	8.34
C28 - M3 - 01	40.345	535.91	184.89	0.35	8.3	896.55	10.31	20.24
C28 - M3 - 02	33.350	535.91	156.00	0.29	7.0	741.12	8.67	14.11
C28 - M3 - 03	36.285	535.91	173.33	0.32	7.8	806.32	9.60	17.05
Mix B (SF 1): Cement + 40% Slag + 20% NRS (w/o Polymer)								
A28 - M4 - 07	37.102	618.36	166.67	0.27	7.5	824.48	8.08	15.48
A28 - M4 - 08	36.872	618.36	160.00	0.26	7.2	819.38	8.29	15.52
A28 - M4 - 09	33.800	618.36	146.67	0.24	6.6	751.10	7.59	13.04
A84 - M4 - 13	21.991	556.52	120.00	0.22	5.4	488.70	5.40	5.67
A84 - M4 - 14	21.521	556.52	120.00	0.22	5.4	478.25	5.48	5.56
A84 - M4 - 15	21.798	556.52	120.00	0.22	5.4	484.39	5.17	5.43
C28 - M4 - 01	26.143	535.91	109.78	0.20	4.9	580.95	6.98	8.51
C28 - M4 - 02	28.089	535.91	115.56	0.22	5.2	624.21	7.37	10.18
C28 - M4 - 03	25.322	535.91	109.78	0.20	4.9	562.72	6.94	8.68
Mix C (SF 2): Cement + 40% Slag + 20% NRS (with Polymer)								
A28 - M5 - 07	34.793	618.36	226.67	0.37	10.2	773.17	6.41	12.74
A28 - M5 - 08	40.406	618.36	266.67	0.43	12.0	897.90	6.74	16.14
A28 - M5 - 09	38.385	618.36	253.33	0.41	11.4	853.01	6.41	13.35
A84 - M5 - 13	24.759	556.52	186.00	0.33	8.4	550.21	4.51	6.92
A84 - M5 - 14	21.565	556.52	162.00	0.29	7.3	479.21	3.93	5.25
A84 - M5 - 15	21.951	556.52	168.00	0.30	7.6	487.80	3.50	4.78
C28 - M5 - 01	25.425	535.91	179.11	0.33	8.1	565.01	6.39	9.03
C28 - M5 - 02	26.245	535.91	184.89	0.35	8.3	583.23	6.59	9.62
C28 - M5 - 03	31.822	535.910	219.55	0.410	9.880	707.15	7.849	13.78

3.1.3 Comparison between model parameters due to the aging affect

The relationships between material parameters and accelerated aging were studied in Figure 3-5 (a)-(d). Time dependent material parameter were fit using a second degree polynomial (quadratic) fit, and associated fit equations of which are mentioned. The elastic Young's modulus for samples is the maximum at age of 28 days, followed by the 85 days aged samples and the un-aged samples. The elastic modulus values were assumed to be the same for all mixes, to simplify the simulations. Figure 3-5 (a) shows the variation of the back-calculated elastic modulus with aging. Material parameter, η was also studied for its effect due to aging of the samples. The material parameter, η for 28 day samples were maintained at a moderately higher value over the un-aged and 84 day samples for all the mixes. Variation of the parameter within replicate samples was pretty much negligible apart from one data point recorded for 28 day samples. Figure 3-5 (b) projects the change in the material parameter, η with aging. Mixes with silica fume without polymer (mix B) and metakaolin (mix A) show close trends with their values several degrees higher than mix without polymer. The effect of first cracking tensile strain, ε_{cr} due to aging is predicted in Figure 3-5 (c). The values of strain due to the first crack show an interesting trend as the silica fume samples with polymers (mix C) report larger strain through all ages, than the GFRC matrix with metakaolin (mix A), followed by mix with silica fume without polymers (mix B). Normalized transition strain, α shows a decrease trend with aging across all mixes. For the mix with silica fume without polymers (mix B)

strain parameter α is more than the mix with metakaolin (mix A) followed by silica fume specimen with polymer (mix C) as evident in Figure 3-5 (d).

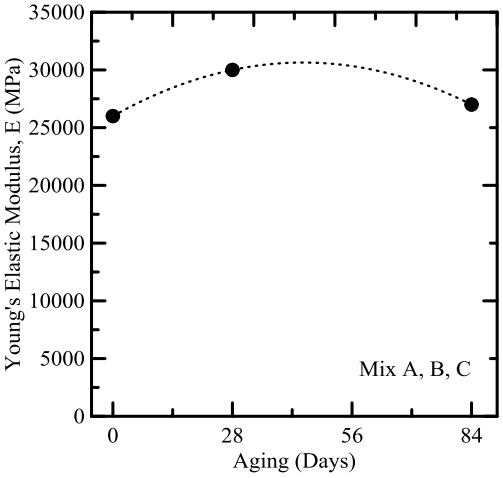

(a)

$E = 26000 + 208*T - 2.34\ T^2$
(R-squared = 1)

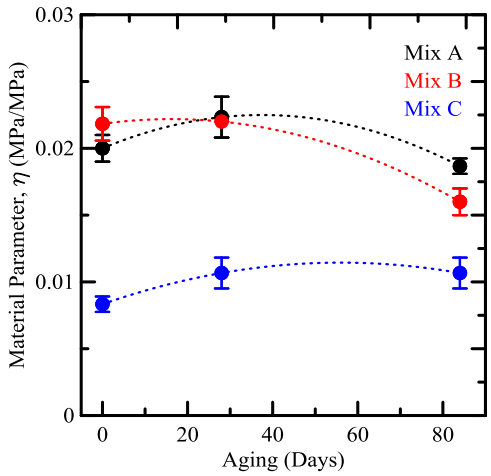

(b)

$\eta = 0.02 + 0.00013 * T - 1.77E\text{-}006 * T^2$
(R-squared = 0.74)

$\eta = 0.02 + 4.37E\text{-}005 * T - 1.35E\text{-}006 * T^2$
(R-squared = 0.93)

$\eta = 0.008 + 0.0001 * T - 9.92E\text{-}007 * T^2$
(R-squared = 0.64)

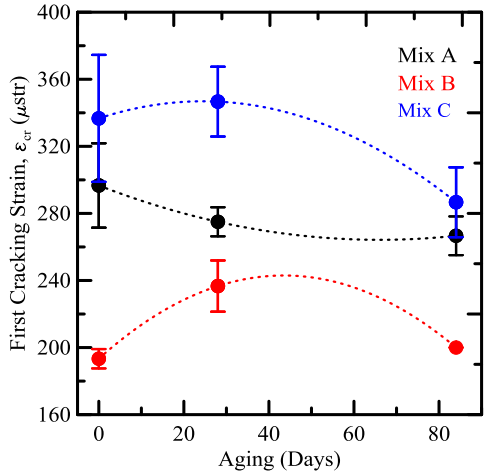

(c)

$\varepsilon_{cr} = 296.67 - 0.98 * T + 0.007 * T^2$
(R-squared = 0.46)

$\varepsilon_{cr} = 193.33 + 2.28 * T - 0.026 * T^2$
(R-squared = 0.859649)

$\varepsilon_{cr} = 336.67 + 0.83 * T - 0.017 * T^2$
(R-squared = 0.57)

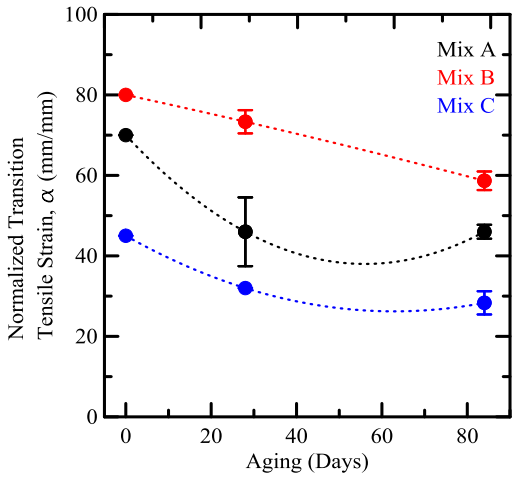

(d)

$\alpha = 70 - 1.14* T + 0.01* T^2$
(R-squared = 0.88)

$\alpha = 80 - 0.23 * T - 0.0003 * T^2$
(R-squared = 0.96)

$\alpha = 45 - 0.60 * T + 0.005 * T^2$
(R-squared = 0.97)

Figure 3-5 (a)-(d) : Time dependent material model parameters

3.2 Temperature dependence in ageing of GFRC composites

A methodology for accelerated ageing of GFRC to understand temperature dependence of GFRC strands in cementitious environment was studied. A procedure involving immersion of glass fiber reinforced composites in hot water at different temperatures for different duration of time was devised by Litherland et al. [57]. Strength of GFRC composites was found to be dependent on fiber content, orientation and distribution of fiber along with fiber matrix bond strength and cement matrix strength. This may however vary with aging time and in between individual composite structures. Hence to standardize the manufacturing process, the technique of sprayed GFRC was used.

3.2.1 Comparison of the present Model with Historical Data

Fiber content of Cem-FIL AR glass was maintained approximately at 5 % to 6 % by weight of the cement based composite. Composites were produced in the form of flat sheets, and dewatered by vacuum suction. Glass fibers were thus randomly distributed in cementitious base in the form of two-dimensional matrix.

Strength-time curves of these composites were characterized by two distinct regions, a steadily degrading initial region, followed by a rather constant strength portion. This can be observed in Figure 3-6 wherein the GFRC composites in the form of strips of dimension 150 mm x 50 mm and thickness varied between 6 – 8 mm, were immersed in water at various temperatures.

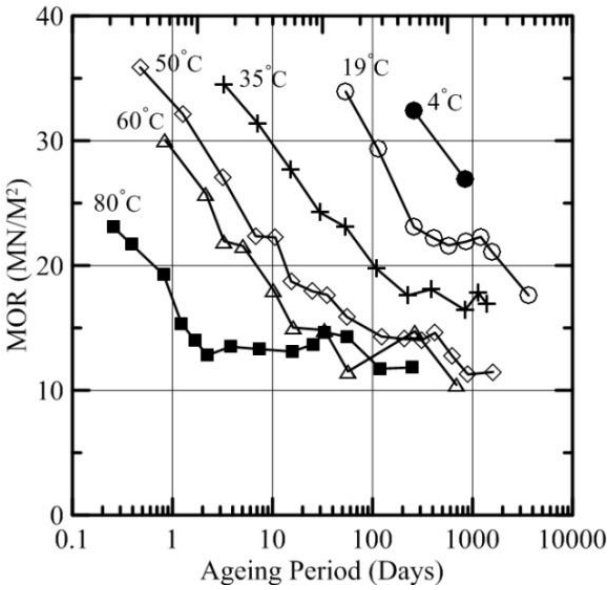

Figure 3-6 : Strength retention of GRC Composites in water at various temperatures

About six replicate specimens were tested at various temperatures for their flexural strength after various ageing periods. The data points in the figure represent the average results obtained from several repetitions of these tests based on variations in temperature and ageing periods. At accelerated ageing temperatures of 60 °C and 80 °C there is a rapid fall in initial strength followed by a constant strength portion referring to the long term strength of these composites. For lower ageing temperatures of 4 °C, 19 °C and 35 °C the initial strength loss is much slower. This indicates that the initial strength loss of GFRC composites is

more rapid at high temperatures. For the ageing temperature of 50 $^{\circ}$C the transition between the initial and the long term strength is much smoother unlike the higher temperatures wherein this transitional phase is more drastic. Earlier research has shown that long term strength of GFRC composites is rather temperature independent, with gradual strength loss in the later stages of ageing.

3.2.2 Inverse Analysis

Objective of this study is to use the material model discussed in the previous sections and observe the trend in the model parameters based on the loss of flexural strength when GFRC specimens were tested at different temperatures. Each set of temperature data was individually considered and the modulus of rupture (MOR) value of each their data points were fed to the material model. Based on the individual MOR values, model parameters were developed and simulated MOR values were matched against the experimental trend. Until both MOR values – simulated (model) and experimental (digitized) match to their second place of decimal, the model parameter were varied until they reach their individual threshold. To simplify this procedure, only one parameter was iteratively modified, while the rest were kept constant throughout this analysis. The parameter to be modified was decided based on their ability to match the trend in experimental MOR, when they were iteratively varied. After many attempts, the model parameters “alpha (α)” and “eta (η)” which are the transitional tensile strain and first cracking tensile strain respectively were selected because of their relative accuracy in matching the experimental MOR values.

(a)

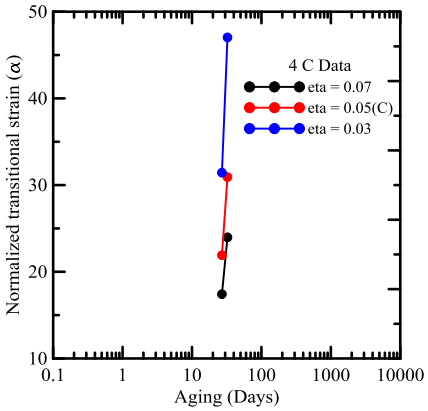

(b)

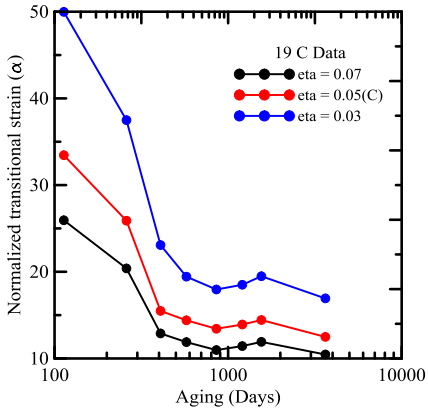

c)

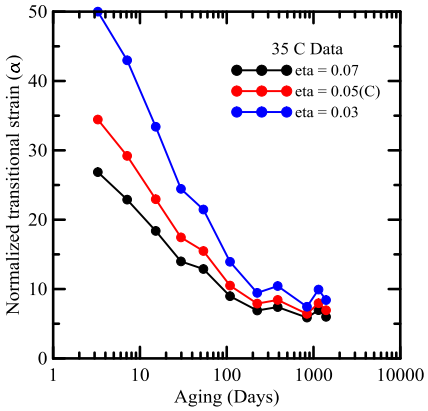

(d)

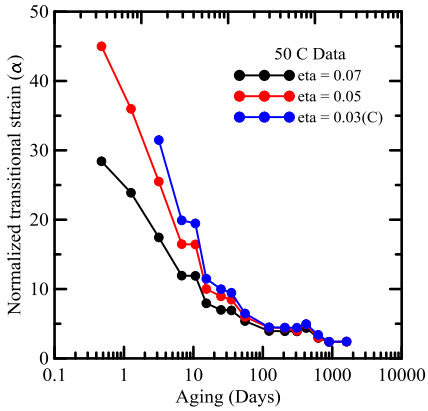

(e)

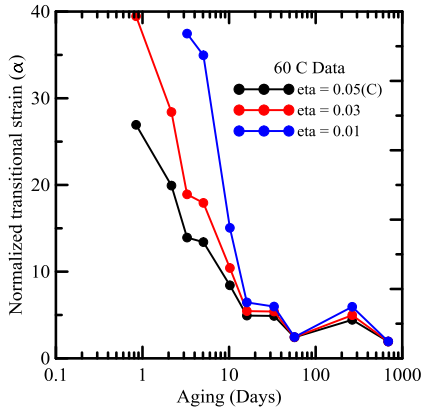

(f)

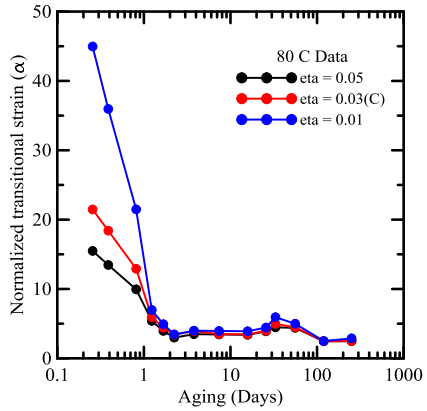

Figure 3-7 (a)-(f) : Response of parameter alpha as a function of parameter eta

Figure 3-7 (a)-(f) shows the response of parameter α against experimental aging response at different η values. Amongst the simulations controlled by

parameter η, one series of α as a function of η is selected and compared in the following figures. Next up the back calculated parameter, α was plotted against the experimental MOR and the latter is plotted against the digitized aging data, all in one plot as shown is Figure 3-8 (a)-(f). This is done to check the correctness of the prediction, and also to facilitate comparison between the model parameter and the experimental responses.

Figure 3-9 shows the comparison between the experimental responses between MOR, ageing period and back calculated model parameter (normalized transitional tensile strain, α). The latter as explained before is obtained from the material model. It is to be noted that the idea behind this study was to simulate the long term response of GFRC composites. Hence even though the model response does not accurately replicate the experimental data points, the response of the material model could predict a trend similar to the experimental trends.

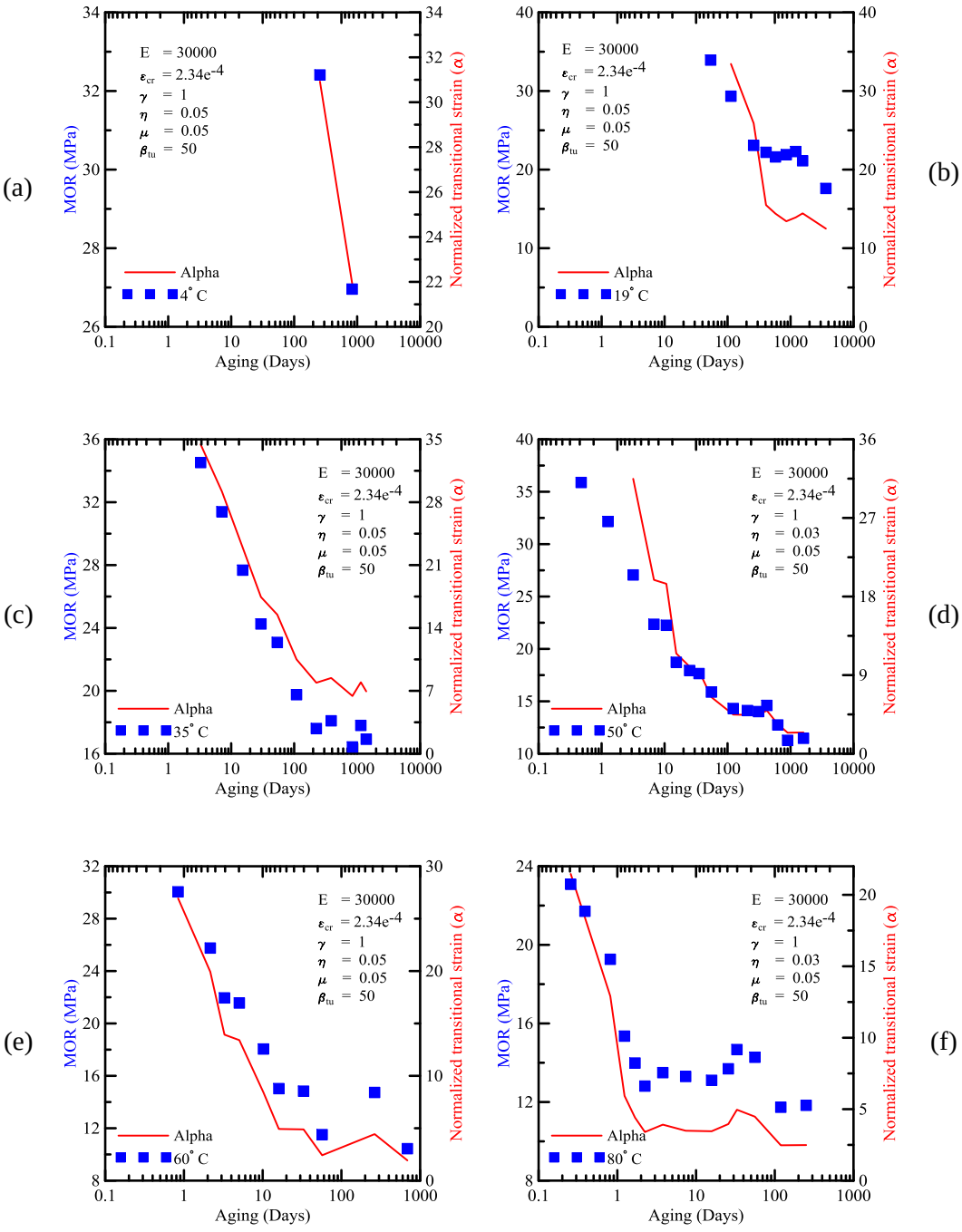

Figure 3-8 (a)-(f) : MOR - aging response against transitional strain (α)at different temperatures

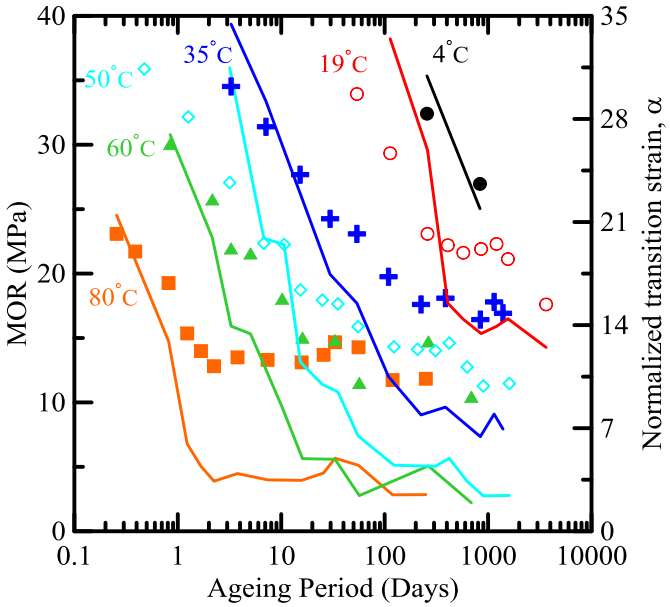

Figure 3-9 : Experimental (symbols only) v/s simulated (solid lines) aging response using transitional strain (alpha)

3.3 Conclusions

The objective of the existing material model was used to characterize and simulate the aging effect in GFRC mixtures. Effect of aging on material responses described by the four parameters: Young's modulus, first cracking tensile strain, first cracking tensile strain and strain at peak stress were established and studied closely. In this study, effects modifications in the cementitious matrix in the form of metakaolin, silica fume and their contribution in long term durability of GFRC composite was studied in detail. Metakaolin has more profound influence in strength retention than silica fume. Temperature dependence through accelerated ageing of GFRC composites was also investigated.

4. IMPACT RESPONSE OF FIBER REINFORCED AERATED CONCRETE AS THE CORE MATERIAL

The objective of this chapter is to investigate the various lightweight cementitious core materials from the view point of sustainability and long term performance. Aerated concrete products have been a very mature technology for construction that has been used for several years. An alternative material that is being considered for the core in the sandwich composite is a new generation of aerated concrete materials that is reinforced with polymeric fibers. This is chosen since the overall material provides good thermal characteristics in terms of conductivity and heat capacity, sound isolation, ductility, fire resistance, and ease of construction. The core material is also quite compatible to the cement based skin, so no additional bonding agent is needed in the construction of the sandwich panels. The core is also compatible in terms of thermal expansion and contraction, moisture migration is limited due to isolated, closed pore system, and finally, the material is non-toxic in the case of fire and has excellent resistance to UV radiations. An experimental based study was conducted on this novel green construction material in order to address the potential ductility especially in cases where the sandwich panel may be exposed to high strain rates. Behavior of this material was evaluated under high strain flexural impact loading in order to document the potential benefits of fiber reinforcement in the aerated concrete products.

4.1 Introduction to Aerated Concrete

Aerated or cellular concrete (AC) is a lightweight, noncombustible, low cement content material with good thermal characteristics. As mentioned in ACI 523.2R [58], aerated concrete is manufactured from a mixture of Portland cement, fly ash or other sources of silica, quick lime, gypsum, water, and aluminum powder or paste. This mixture, if autoclaved for accelerated strength gain, is referred to as Autoclaved Aerated Concrete (AAC). Aerated concrete is characterized by a highly porous structure, with micro air-pores to macro air-pores [59] with the pore diameter in the range of 0.1 to 1 mm. This results in lower density and compressive strength, but good thermal insulation when compared to normal-weight concrete. Figure 1.2.1 shows their pore-structure using a scanning electron microscope and a typical gray-scale image obtained by image analysis.

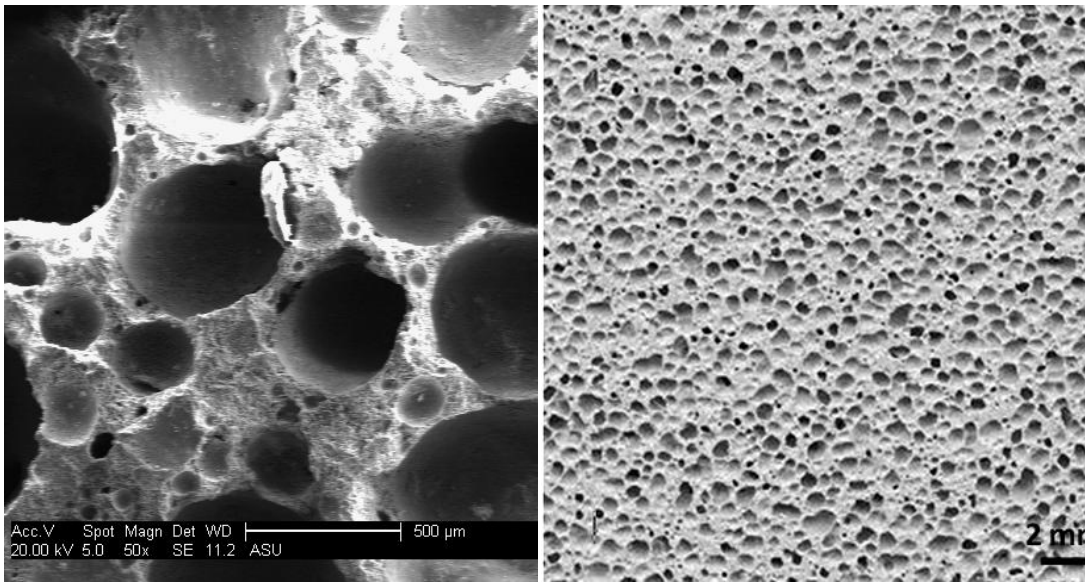

Figure 4-1 **:** Pore-Structure of Aerated Concrete

ASTM C-1693 (previously C-1386) classifies aerated concrete based on the dry density of 400-800 kg/m^3 and compressive strength values of 2-6 MPa [60]. Thermal conductivity is reported to be 0.07 - 0.11 W/m.°C which is several times less than normal weight concrete [61]. The porous micro structure is a result of chemical reaction between calcium hydroxide and aluminum powder or paste. As a product of this reaction, hydrogen gas is generated which associates with large volume changes, as the cementitious mix expands to almost twice its volume. The chemical reaction as shown in Equation 4-1 contributes to a highly porous structure. Neithalath [62] reported that approximately 80% of the volume of the hardened material is made up of pores with a general ratio of 2.5:1.0 air-pores to micro-pore.

$$2Al + 3Ca(OH)_2 + 6H_2O \rightarrow 3CaO.Al_2O_3.6H_2O + 3H_2 \uparrow \qquad \text{Equation 4-1}$$

Supplementary cementitious materials such as slag, fly ash and silica fume have been increasingly used to improve aerated concrete and further focus on sustainability. Addition of high volume fly ash not only benefits in reuse and recycle of coal combustion by-products but also improves the durability of cement-based materials in exposure to external sulfate attack [63]. However because of low density and relatively low compressive strength limits its applicability to many structural applications. It could be easily be used in construction of one-two stored buildings. AC is comparatively lighter than regular masonry units making it a perfect material for small-scale constructions in seismic regions. Excellent thermal insulating properties of AC helps in reducing house-

hold energy consumption by about 7% by controlling the cooling energy associated with the HVAC systems in residential structures [64]. A unique variation of aerated concrete is Fiber-Reinforced Aerated Concrete (FRAC) wherein autoclaving process is eliminated from the production and curing is performed at room temperature. FRAC as the name suggests is additionally reinforced with short polymeric fibers such as polypropylene. Thus making it a pseudo-ductile composite characterized by a ductile elasto–plastic load – deformation behavior [65]. The reason behind elimination of autoclaving conditioning process is to protect the polymeric fibers, but this affects the overall strength and affects the homogeneity of the system. However cost effectiveness and energy efficiency can be achieved by eliminating the autoclaving process. Thus FRAC can serve as a novel green construction material. Short polymeric fibers induce bridging action during crack formation in elastic and plastic stages due to the mechanical forces, shrinkage, or standard heating-cooling cycles. Research conducted [66] to assess the effect of adding short polypropylene fibers to lightweight cementitious panels have reported marked improvement in mechanical properties such as modulus of rupture and toughness along with improved resistance to cracking and crack propagation [65]. Aerated concrete products can exhibit a considerable amount of residual compressive strength after reaching the peak strength [67]. Ratio of residual strength to peak strength for FRAC is however typically more than AAC due to the role of uniform distribution of randomly oriented fibers in integrating the cellular structure. Thus AAC is characteristically more brittle than FRAC which shows a predominantly

ductile response under flexural and tensile loading, as evident in Figure 4-2. Post peak response under compression is predominantly characterized by sequential crushing of pores, and collapse of cellular walls. Under tensile/flexural load, ductility in FRAC can be observed after reaching its ultimate strength whereas AAC shows characteristically brittle response, as discussed earlier.

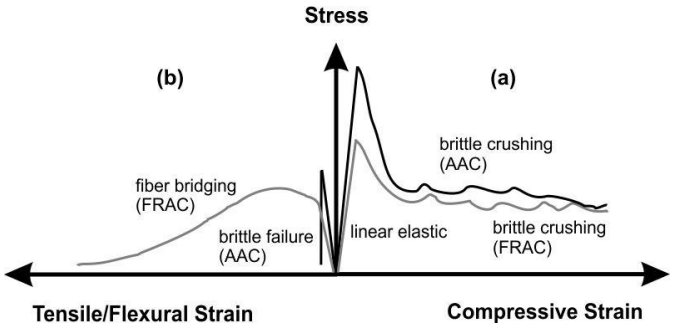

Figure 4-2 **:** A schematic view of strain-stress response for AAC (black) and FRAC (gray) [86]

Literature Review

Impact behavior of materials has been the topic for several investigations especially based on low-velocity impact on fiber-reinforced concrete composites. Type of impact test can be broadly classified as: Charpy, Izod, drop-weight, split Hopkinson bar (SHB), explosive, and ballistic type tests. These tests can be either instrumented or heuristically based and the resistance can be measured based on fracture energy, damage accumulation, and measurement of the number of drops to achieve a desired damage or stress level [1]. Testing variables can be size of specimen, machine compliance, strain rate, type of instrumentation, or the test set-up itself. Natural fiber-reinforced cement composites under similar three point

bending configuration based impact testing system using a drop weight mechanism was conducted by Silva et al. [68]. They observed no significant effect of strain rate on the ultimate strength of the composites under impact loading when compared to static tests. Energy absorption showed an increasing trend with increase in drop height. Zhu et al. [69] studied alkali resistant (AR) glass fabric reinforced cement composites and crack pattern. Specimen with beam type orientation show a higher load carrying capacity and lesser deflection when compared to plate type orientated specimens. Maximum flexural stress and absorbed energy of beam specimen increased with the number of fabric layers, whereas plate specimen show reverse trend. Initial stiffness degradation is observed after first crack formation; however initial stiffness as a function of impact energy was insignificant. Impact properties of polyethylene (PE) fabric were investigated by Gencoglu et al. [70] and compared to AR glass fabric. PE fabric composites as they exhibit more load carrying capacity at large deflections and hence more ductile than AR glass fabric systems. However PE fabric composites displayed lesser strength than AR glass composites, which showed brittle behavior.

Charpy impact tests and static three point bending tests were conducted by Silva et al. on sisal pulp fiber-reinforced cement composites with a fiber mass fraction of 14%. Insignificant difference was observed between maximum force obtained from static and impact test [71,72]. Modified SHB used by Romano and Silva et al. to characterize steel fiber-reinforced concrete (SFRC), showed an increase in both toughness and ultimate strength when compared to static compression test

[73]. Bindiganavile and Banthia [74,75] showed that flexural strength is higher when subjected impact loading in comparison to quasi-static loading for fiber-reinforced concrete. Polymeric fibers reinforced concrete reported an improvement in energy absorption under impact loading. Manolis et al.[76] also showed that fibrillated polypropylene fibers significantly improved the impact resistance of concrete slabs. Lok and Zhao [77] reported that at strain rates exceeding $50s^{-1}$, post-peak ductility of steel fiber-reinforced concrete (SFRC) is lost owing to the loss of bond between the concrete fragments and steel fibers. Choi and Lim [78] addressed the impact response of composite laminates using the concept of linearized contact law approach. Wang et al. [79] identified two different damage mechanisms for fiber-reinforced concrete (FRC) under drop weight impact. Fiber fracture dominates the failure mechanism for fiber fractions lower than the critical fiber volume (CFV). Whereas FRC with fiber fraction higher than the CFV, fiber pull-out mechanism dominates the impact response. The critical value for the hooked steel fibers was found to be in between 0.5% and 0.75%. Li et al.[80] investigated the behavior of extruded sheets with short fibers of polyvinyl alcohol (PVA) and glass under static and impact loads. Glass fibers were found to be more effective in improving the tensile strength and impact properties, while PVA fibers increased the tensile strain and absorbed energy of specimens. Low velocity impact (LVI) response of autoclaved aerated concrete (AAC) was investigated by Serrano-Perez et al.[81] and their load carrying capacity was stated to be limited due its brittle nature. However sandwich plates made with carbon fibers and AAC as core material, were found to be considerably

ductile when subjected to similar impacts. AAC units under high-intensity pulses using specially developed micro-explosions were studied for the characteristics of dynamic cracking and comparison was made to plain hardened cement paste (HCP) by Yankelevsky and Avnon [82]. Textile fabric glued to AAC with PVA as surface reinforcement was found to increase the tensile strength and ductility along with improved resistance to spalling cracks due to the explosion. Influence of addition of hydrophilized and non-hydrophilized fibers to AAC, at different fiber contents between 0.1 % - 0.4 % was studied by Laukaitis et al [83]. Carbon, polypropylene, basalt and kaoline fibers were used for this project. Compression and flexural strengths were investigated for various fibrous additions. Carbon fibers showed maximum strength followed by polypropylene, basalt and kaoline fibers. Hydrophilized fibrous additives contribute more to the increase in compressive and flexural strengths than non-hydrophilized fibers. Micro-structural properties were studied using scanning electron microscope in terms of chemical interaction of fibers with concrete matrix, which ultimately influences the macro-structural properties. Fiber filaments which were chemically inert showed higher strength, when compared to kaoline filaments which interact chemically with concrete matrix resulting in loss of strength. Fracture toughness of AAC was investigated by Wittmann and Gheorghita [84] through compression tests on ring beams, beams in the shape of prisms were tested under three point bending and a compact tension (CT) specimen. Fracture energy of AAC was found to be about one-tenth of normal weight concrete. Compressive, splitting tensile strength, impact resistance properties of nylon and polypropylene fiber

reinforced concrete were studied by Song et al [85]. Due to the higher tensile strength of and better fiber distribution in the concrete matrix, nylon fibers displayed higher strength and better resistance to shrinkage cracks when compared to polypropylene fibers. Large projectile type impact tests using a wood lumber at a controlled velocity and small projectile high energy type tests using hand guns were conducted on fiber reinforced cellular concrete (FRCC) by Zollo and Hays [65]. Extent of penetration was evaluated and impact response of FRCC was documented to be influenced by its low-density void structure.

4.2 Experimental Program

4.2.1Material Properties

FRAC is manufactured in the form of masonry blocks in various sizes and dimensions. Mixture proportions of the ingredients are listed in Table 4-1. Constituents of the mix are weighed and mixed using an automatic batching system.

Table 4-1 **:** Mix proportions (percentage by weight)

Material (each batch)	FRAC	AAC
Cement	28	18
Fly ash	42	0
Silica	0	27
Lime Stone + Gypsum	0	8
Recycled Material	0	9
Water ~ 38 °C (100 °F)	28	38
Polypropylene Fiber	0.2 – 0.4	0
Aluminum Paste	<0.1	<0.1
Other additives (classified)	0.3	0

Preparation and the steps involved in the manufacturing process of FRAC blocks are based on using preheated water at 38 °C which speeds the reaction process. The fresh prepared slurry is poured into large steel molds of dimensions 8m x 1.2m. Depth of pour inside the mold is maintained at 0.6m. Since the autoclaving process is not used in the manufacturing process, temperature distribution through the mixture is influenced by the interaction of the size of the specimens with internal heat generated during the exothermic chemical reaction and the ambient temperature. The hydration generates heat due to exothermic reactions within the first 24 hours and a rise in temperature as much as 30 degrees is observed, which may result in micro-cracks in the initial few hours. The non-uniform temperature distribution introduces heterogeneity in the process, which further influences material porosity and inconsistency in mechanized test results. FRAC is retained in its molds, until it achieves desired composure and form. It is normally hardened for 5 – 7 days after casting, and then de-molded. Blocks of dimension 8m x 1.2m x 0.6m are then cut using wheel blade. Extensive research [86] on FRAC with varying amounts of polypropylene fiber dosage has been tested earlier and a correlation between mechanical properties and the level of fiber dosage was studied. These include micro and macro level pore structure analysis, variation of density and compressive strength within the blocks, compression, flexure, and tension properties along with thermal conductivity.

Table 4-2 lists out some of the properties determined based on the above experiments conducted [1,86].The material properties show a distinct range of values based on fiber dosage between 0.2–0.4 %, as mentioned in

Table 4-2. Figure 4-3 shows the instrumented three point static bending test conducted on AAC and FRAC, whose results can be seen in Figure 4-4.

Table 4-2 : Selected material properties of AC

Selected material properties [86]	FRAC	AAC
Compressive Strength: F_c: MPa	3.05 – 3.22	5.61
Residual Strength: MPa	1.71 – 1.76	1.52
Residual Strength Ratio	0.53 – 0.54	0.27
Elastic Modulus: GPa	4.51 - 5.02	7.50
Poisson's Ratio	0.26 - 0.27	0.26
MOR: MPa	0.27 - 0.56	0.66
Flexural Initial stiffness: N/m	4.20 - 4.58	4.06
Tensile Strength, F_t: MPa	0.10 - 0.13	0.10

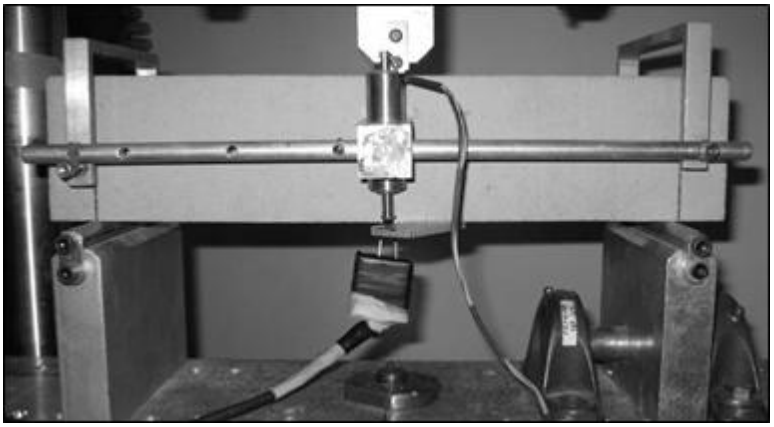

Figure 4-3 : Setup of static flexural test conducted on notched AC beams

(150x150x450 mm)

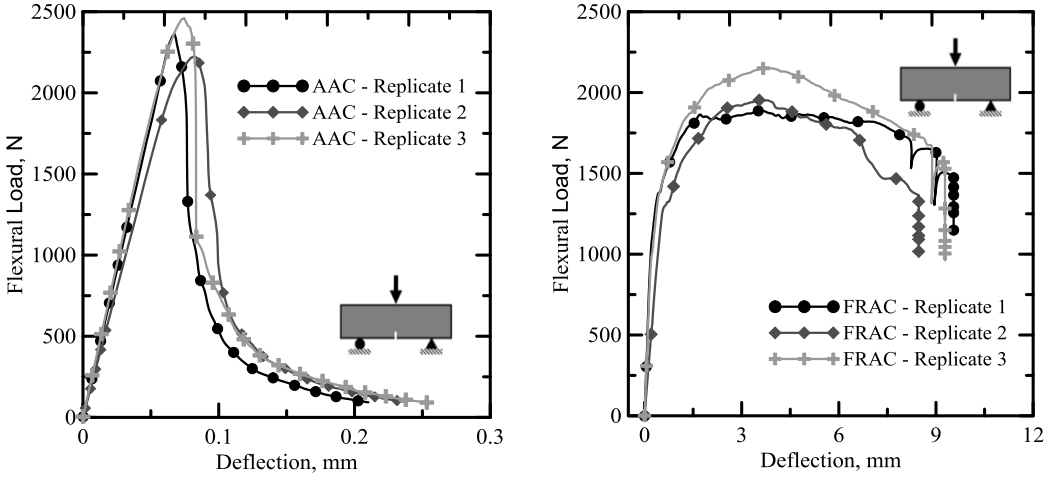

(a) (b)

Figure 4-4 : Static flexural load versus deflection for (a) AAC and (b) FRAC

4.2.2 Impact test procedure and instrumentation

Impact test set-up included an instrumented hammer dropped freely on a specimen placed under a three point bending support system. Schematic of the system is shown in Figure 4-5(a) and a picture showing the test setup during an actual test can be seen in Figure 4-5(b). The drop heights can be adjusted within a range from 1 to 2000 mm which can be controlled by means of an electronic hoist and release mechanism. An anti-rebound system consisting of a pneumatic brake system triggered by a contact type micro switch was in place to stop the hammer after the duration of impact. The experimental set-up consists of the entire moving part that impacts the specimen including the free weight, frictionless bearings along the drop columns, load cell, connection plate, and a set of threaded rods. This entire assembly was referred to as the hammer and weighed approximately

134 N. In case the test specimen breaks completely, the threaded rods protect the bottom load cell from the impact of the hammer. The hammer can be released from a predetermined drop height by means of triggering switch which is backed by an electronic brake release mechanism.

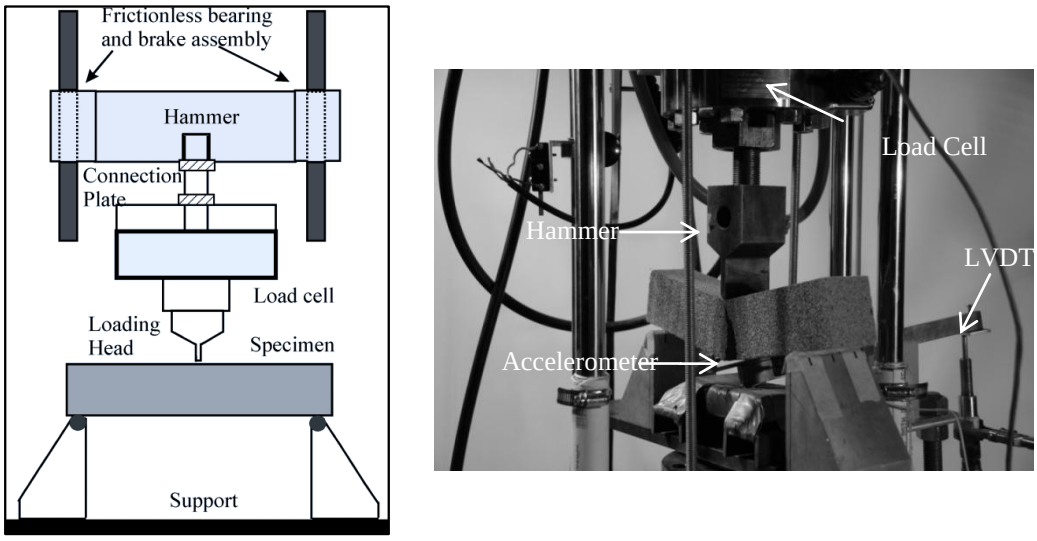

(a) (b)

Figure 4-5 : Schematic diagram (a) and actual picture (b) of impact test set-up

The impact force induced by the free fall weight was measured by the strain-gage based load cell with a range of 90 kN mounted on the hammer behind the blunt shaped impact head. Another load cell with same capacity was mounted beneath the support plate and is used to measure the force transmitted to the equipment base. A linear variable differential transformer (LVDT) with a range of $\pm$10 mm was connected to the bottom of specimen (tension zone) by means of a lever arm. Test specimen is placed on metal clip that is screwed to the lever arm. An accelerometer with a capacity of $\pm$ 500g m/s^2 was placed in the tension zone of the specimen to document the acceleration-time history of the specimen. The data acquisition system consisted of a PC based National Instruments PCI

acquisition card and LABVIEW VI's with a trigger function which can record signals from load cell, accelerometer and the LVDT simultaneously at sampling rates of up to 100 kHz. For this study, the data acquisition system was conditioned to collect data at the sampling rate of 20 kHz. The entire duration of the test lasts 200 milliseconds irrespective of the testing conditions. Signal acquisition during a high dynamic test is strongly conditioned by the nature of the test itself [87], and its interpretation is problematic. Rapid variation of the kinematic quantities excites vibrations depending on the initial stiffness and mass of both the specimen and the hammer resulting in disturbed signals. The interpretation of these signals is difficult and hence it is mandatory to filter the data [88]. The frequency of data collection, results in large set of data corresponding to each of the measured response. Careful investigation of data response is necessary to select the range of data corresponding to the actual impact on the specimen. In order to address these challenges, a MATLAB program was developed for data processing and analysis of raw test data. Steps involved in the analysis along with the fundamental concepts are discussed in the following section. A high speed digital camera (Phantom v.7) was set up to record the proceedings during the duration of impact. The damage caused in the specimen for the different drop heights were then compared by visual examination.

4.2.3 Theoretical background

The input energy for this test is the potential energy of the hammer and depends on its drop height, mass and the amount of energy lost during the free fall of the dropping mass. While a part of the input energy is absorbed by the test

specimen and stored in as internal energy, a part of the remaining energy is either dissipated by friction, or transferred to the test set up through the supports after the impact event. The input energy or the potential energy of the hammer, U_i is defined based on the principle of conservation of energy, is stated in Equation 4-2.

$$U_i = mgH = \frac{1}{2}mv_0^2 + U_d = U_k + U_f + U_d \qquad \text{Equation 4-2}$$

In this equation m is the mass of the entire moving assembly measured to be approximately 134 N, g stands for acceleration due to gravity, H is the drop height of hammer which is varied accordingly, v_o represents the hammer velocity prior to impact, U_d is the frictional energy dissipated energy between the time of release of the hammer until just prior to the impact event. U_k represents the energy absorbed by the specimen which is also the toughness of the material, and U_f represents the energy remaining in the system after complete failure of the specimen. This energy may be elastically stored in the specimen resulting in rebound of the hammer mass, or transmitted through the specimen to the support. The rebound action of the hammer is generally observed at relatively small drop heights, and depends on the initial stiffness and strength of the material tested. The absorbed energy or kinetic energy dissipated in the specimen, U_k, was defined as in Equation 4-3 **[**1**]**.

$$U_k = \int_{t=0}^{t=t^*} P(t)v(t)dt \approx \sum P(t)\Delta d(t) \qquad \text{Equation 4-3}$$

Where *P(t)* and *v(t)* represent the force and velocity history of the impact event, *t** represents the impact event duration, $\Delta d(t)$ represents the deflection increment history of test specimen. This can be alternatively defined as the area enclosed between the load-deflection responses obtained from the analysis. Velocity of the hammer, v_0 prior to the impact is calculated using the energy conservation concepts, as represented in Equation 4-4 [1].

$$v = \sqrt{2gH} \qquad \text{Equation 4-4}$$

The maximum flexural stress, σ_f, was measured as in Equation 4-5 **[**1**]** based on the classical linear elastic - small displacement bending equation associated with 3 point bending flexural tests.

$$\sigma_f = \frac{3}{2}\frac{P_m L}{bh^2} \qquad \text{Equation 4-5}$$

In this equation, P_m is the maximum load recorded during the test, *b* and *h* are the width and thickness of the test specimen, respectively, *L* is the specimen span. The strain rate for three point bending test was computed in a method based on continuous mechanics proposed by Land [89]. The general form is as stated in Equation 4-6 [1].

$$\varepsilon_{\max} = \frac{2h(N+2)y}{(L-a)[L+a(N+1)]} \qquad \text{Equation 4-6}$$

Where *h* and *L* are same as the above, *N* is the creep exponent and *y* is the deflection. For a three point bending configuration and elastically deflected material: $a = 0$ and $N = 1$. Differentiating with respect to time, t reduces this equation to a modified form as shown in Equation 4-7 [1].

$$\dot{\varepsilon} = \frac{d\varepsilon}{dt} = \frac{6Hv}{L^2}$$ Equation 4-7

Where *v* is the velocity of test specimen calculated using the slope of the displacement - time response.

4.3 Analysis of test data

Un-notched specimens of three different dimensions were tested during this study, whose brief geometric details are mentioned below in Table 4-3. While the length and span of the specimen were kept constant at 250 mm and 200 mm, respectively. Two types of cross-section: square and rectangular cross-section was considered to understand the size effect of aerated concrete beams when exposed to impact loading. Width and thickness of the specimen were alternately varied between 50 mm and 100 mm. Impact tests were conducted at initial heights of 25 mm, 75 mm, and 150 mm of the impactor. Polymeric fiber content of FRAC specimens tested was kept constant at 0.4%.

Table 4-3 : Dimensions of specimen tested under impact loading

Type of AC		Dimensions, mm (L x B x D)	
FRAC	A	250 x 50 x 50	Square X/S
	B	250 x 50 x 100	Rectangular X/S
	C	250 x 100 x 100	Square X/S
AAC	A	250 x 50 x 50	Square X/S
	B	250 x 50 x 100	Rectangular X/S
	C	250 x 100 x 100	Square X/S

This section discusses the MATLAB program specially developed to analyze the test data and calculate useful mechanical properties. The idea behind developing this code was to process the raw data through necessary modifications, smoothening and filtering of the response to reduce the noise in the data, characteristic of such dynamic tests. The code was developed in several parts. First section deals with input parameters which include physical specifications of test specimens span and overhang length of the sample. Testing variables which include geometrical details and material properties of the specimen should be carefully entered, to obtain meaningful and correct results from the analysis. Control parameters for data reduction of raw response are defined after number of trials with different combinations of such numbers. Test data is next converted to international unit (SI) of measurement, and the first row of time, load, acceleration and deflection responses is modified to start from zero. Each of these modified responses was further smoothened to reduce their inherent noise. Due to the dynamic nature of this test, the entire range of all the responses are often characterized by multiple peaks. Identifying the actual impact and corresponding range of reduced data is necessary for further processing and meaningful interpretations. After careful consideration of all the measured responses, deflection was considered as the basis for selection of the range of the actual impact. Subsequently a set of data is generated which is smoothened and reduced based on the above procedure. A linearization fit of the load – time response is critical to minimize external disturbances and also for comparison between replicate data. Modified data is further reduced to three segments based on

selection of a range of data which represents a somewhat linear load response. Initial part of load data, prior to the manually selected linear range, corresponds to the first section. This is followed by the selected linear load-time response and the remaining non-linear load response. Corresponding acceleration and deflection data is defined for these three segments. Section of the modified data before the linear part is ignored, as it is assumed to be caused by the initial disturbances during the test. Instead a new set of data is defined based on the slope of the linear part. The non-linear part is retained in its original form. Next, the linearized load-time curve combining all the segments is shifted to start the time data from origin. A modified set of data is generated, which is to be used for further calculations. This concludes the second part of code whose focus was mainly to reduce the raw response to a rather selective, smoothened response indicating the actual impact event as shown in Figure 4-6. A series of plots corresponding to all the measured responses is generated to check the correctness of the analysis. The final part of the code focuses on applying the theoretical concepts discussed in the previous section. Impact velocity of the hammer is computed based on Equation 4-4. Stress generated due to the impact is calculated using Equation 4-5. A polynomial fit of the displacement-time response is generated, and solving for the unknown in the equation gives the slope of the displacement-time response. This value corresponds to the velocity of the sample during the test, which further utilized to calculate the strain rate using Equation 4-7. The slope of the load-deflection response corresponds to the rigidity or the Initial stiffness of the specimen. These

computed values and responses were further analyzed by generating standard figures, mentioned in the latter sections.

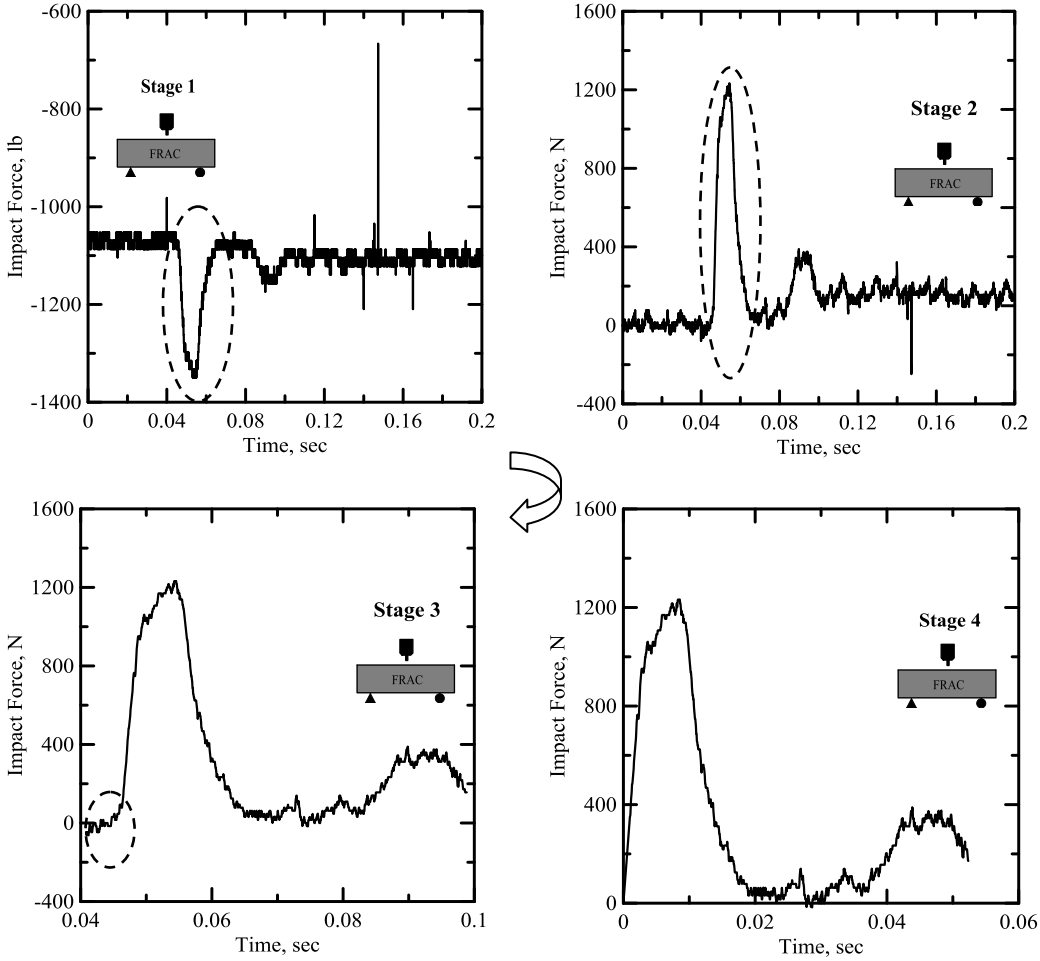

Figure 4-6 : Different stages involved in processing of experimental data

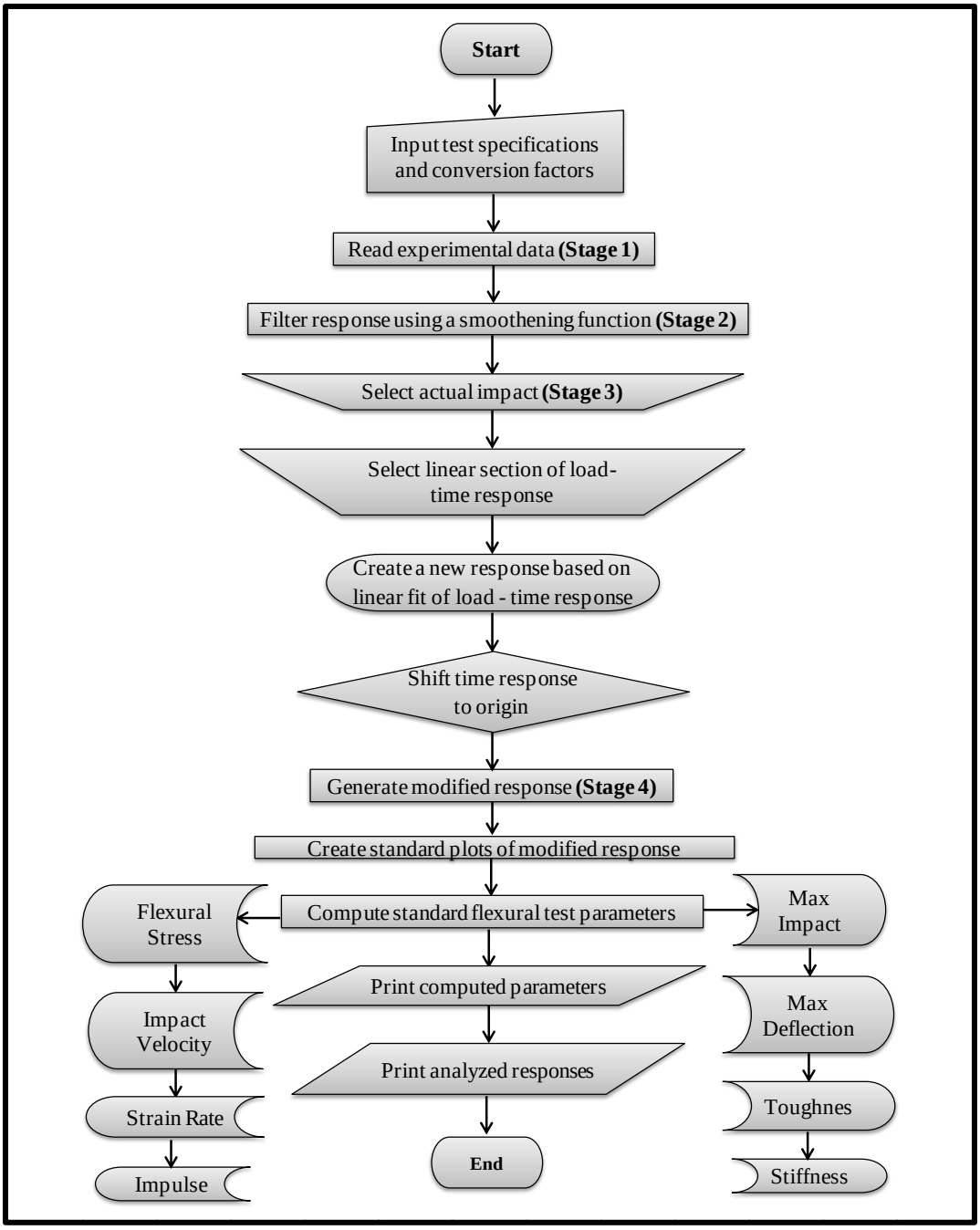

Figure 4-7 : Flow Chart explaining the analysis involved

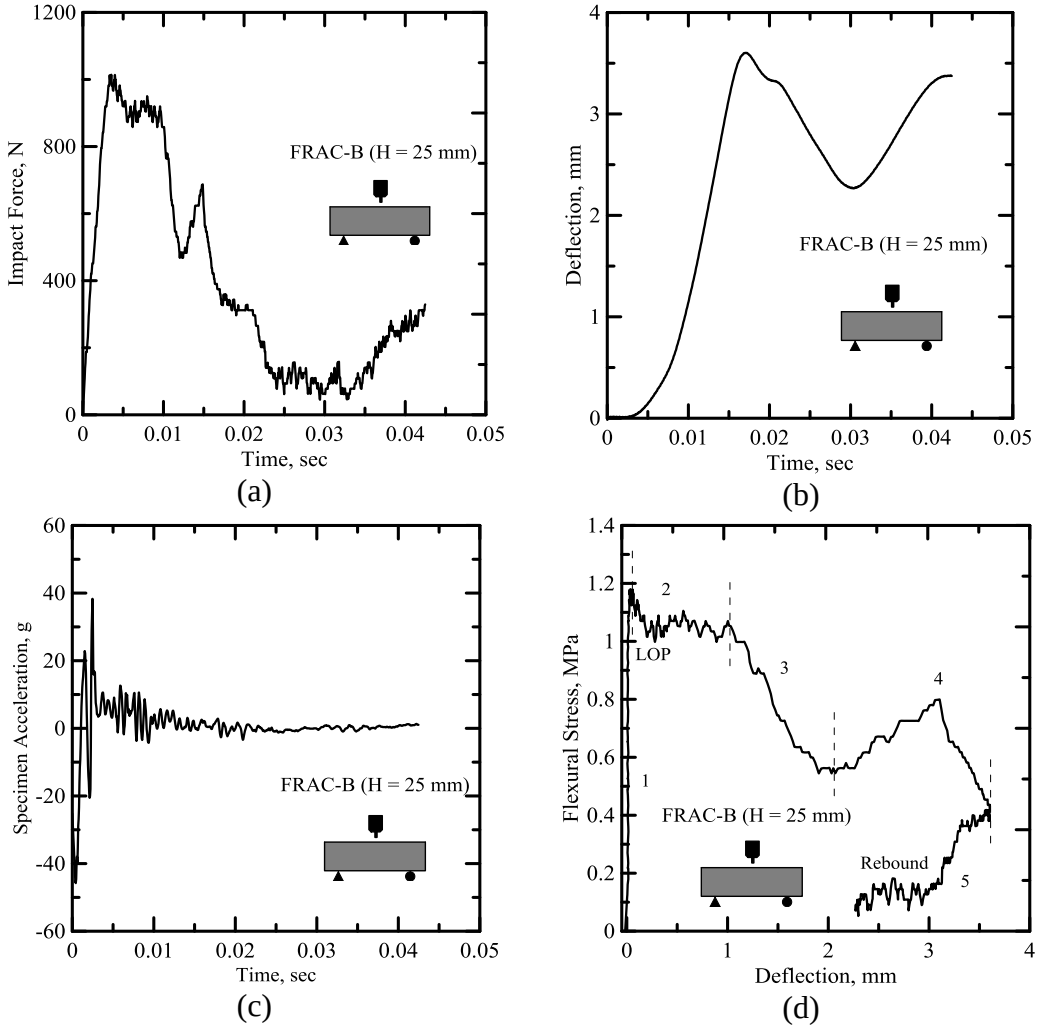

Figure 4-8 (a)-(d) : Post analysis response of an impact test event

Figure 4-8 (a)-(d) and Figure 4-9 presents typical results obtained from analysis of a FRAC-B specimen tested at a drop height of 25 mm of impact hammer. A typical flexural stress vs. deflection behavior can be categorized in five distinct zones as presented in the Figure 4-8(d). Zone I is the linear elastic range that ends with the formation of the first crack. The stress corresponding to this point is defined as the limit of proportionality (LOP). This is followed by Zone II which is characterized by multiple cracks associated with strain softening. Initial stiffness / rigidity degradation starts in Zone II, and maximum flexural

stress values are obtained at the end of this region. Strain softening behavior is again predominant in zones III and zone IV can be associated with fiber pull-out mechanism. Depending on the nature of available energy which is a function of drop height, Zone V can be observed which is characterized by the rebound of the specimen. If there is sufficient ductility and stiffness in the specimen to absorb the applied energy, some of the stored energy released causes a rebound that is characterized by a reduction in deflection of the specimen as the load is decreased. Time history of load, deflection and acceleration response obtained from the above test is shown in Figure 4-9. Considerable phase lag can be observed in deflection signal because maximum deflection of specimen is recorded when the load acting on it drops significantly. Acceleration of the specimen initially increases with increase in the load, followed by which it decelerates before coming to rest. However the load and deflection signals stabilize much after the specimen fails due to which permanent deflection and post failure oscillations exist even after the impact event. According to Newton's second law of motion, depending on the mass of the FRAC and AAC specimens, inertial force computed based on the peak acceleration value was found to be approximately 10% of the maximum impact force. For comparison of impact responses across different size and material of test specimen, inertial force on the specimen during impact was neglected.

Five (or more) replicate specimens were tested for each testing condition. Replicates of FRAC-B specimen tested at drop height of 75 mm are shown in Figure 4-10 shows the reproducibility of test responses.

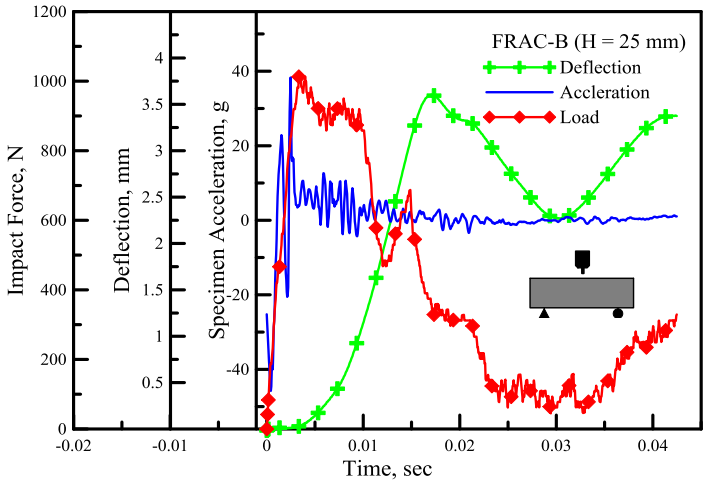

Figure 4-9 : Time history of impact event of FRAC under low velocity impact

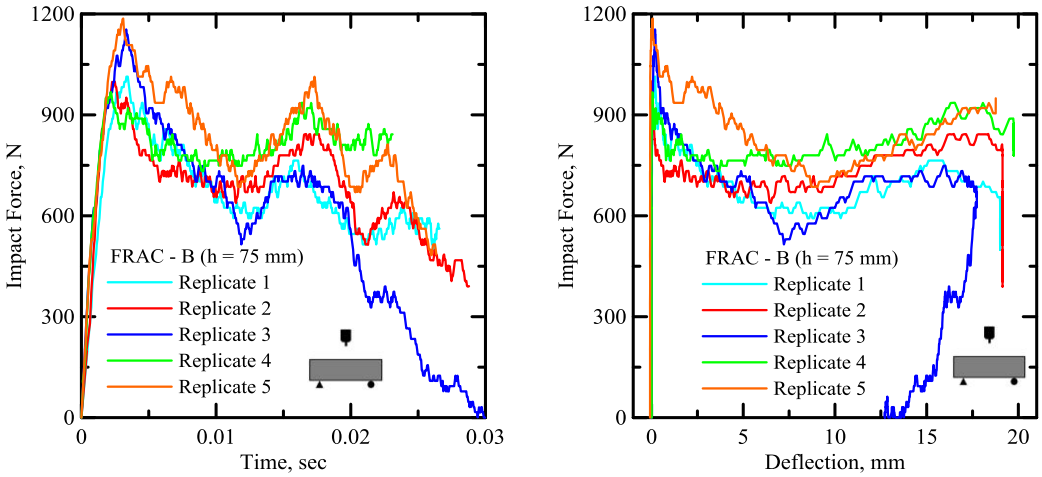

(a) (b)

Figure 4-10 (a)-(b) : Response of replicate FRAC-B specimens tested for same drop height

4.4 Discussion of Test Results

4.4.1 Effect of drop height

Drop height of hammer was varied between 25, 75, and 150 mm and correspondingly input potential energy of the impact ranges between 3 to 21 J. Figure 4-11 (a) – (b) shows the summary of time history of impact force and acceleration curves of selected representative FRAC specimens. Figure 4-11 (a)

suggests a trend regarding the effect of drop height of hammer on mechanical properties associated with FRAC. By varying the drop height of the impactor, the input energy or potential energy and drop velocity of the hammer is varied. For large specimens effect of the drop height is more pronounced, as for FRAC-C specimen maximum impact force increases with increasing drop heights. For FRAC-A and FRAC-B specimen increase in the drop height has marginal effect on peak impact force and flexural strength. Initial stiffness of FRAC-B and FRAC-C also increases with increasing drop height. Owing to their larger cross-sectional dimensions, they tend to behave like a stiff beam with good linear response under higher impact loads. Figure 4-11(b) shows time history of acceleration response, which measured using an accelerometer placed near the tension zone of the specimen. Peak acceleration recorded tends to marginally increase with increasing drop height.

Figure 4-12(a) – (b) shows the time history of the force and acceleration response for AAC specimen, respectively. There is insignificant effect of the drop height of the impactor on AAC specimen. The peak impact force and corresponding flexural strength is somewhat independent of the drop height of the drop height. Only peak acceleration recorded tends to marginally increase with increasing drop height.

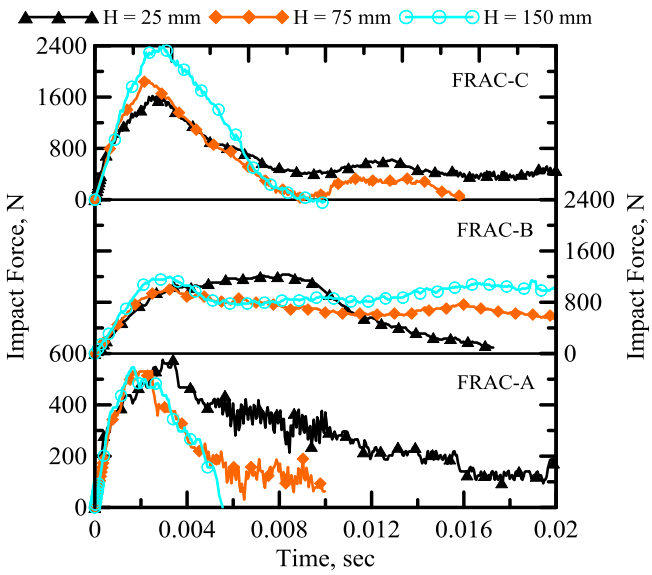

(a)

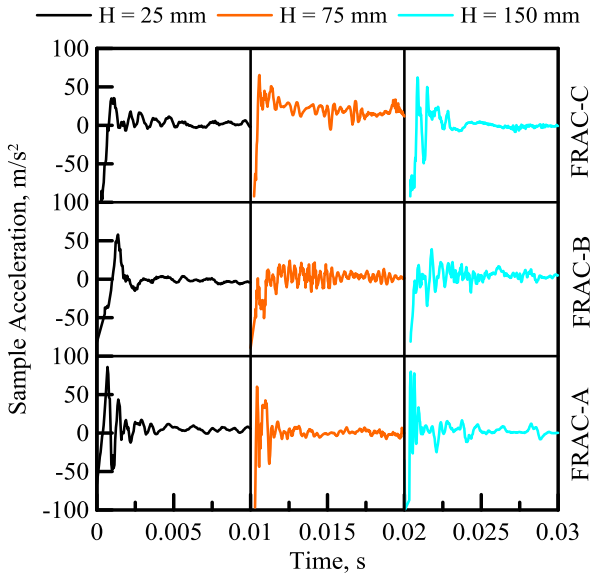

(b)

Figure 4-11 (a)-(b) : Effect of drop height on FRAC specimen

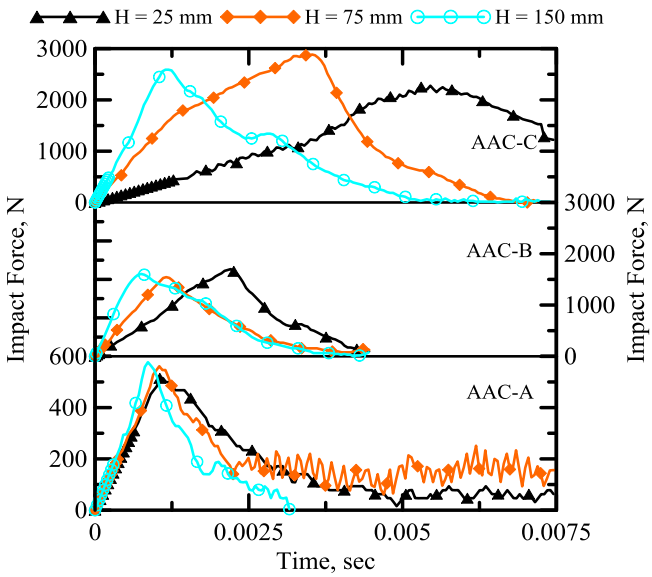

(a)

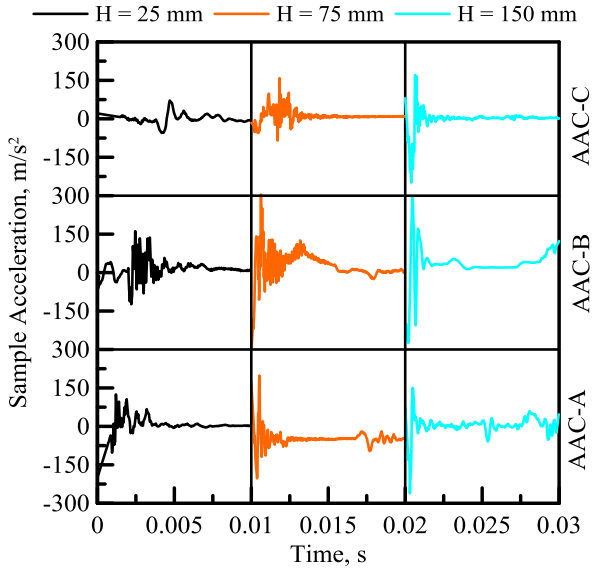

(b)

Figure 4-12 (a)-(b) : Effect of drop height on AAC specimens

4.4.2 Size Effect

Size effect was studied through three different cross-sections of AC specimen as mentioned in table 3. Figure 4-13 (a) – (b) and Figure 4-14 (a) – (b) summarizes their responses.

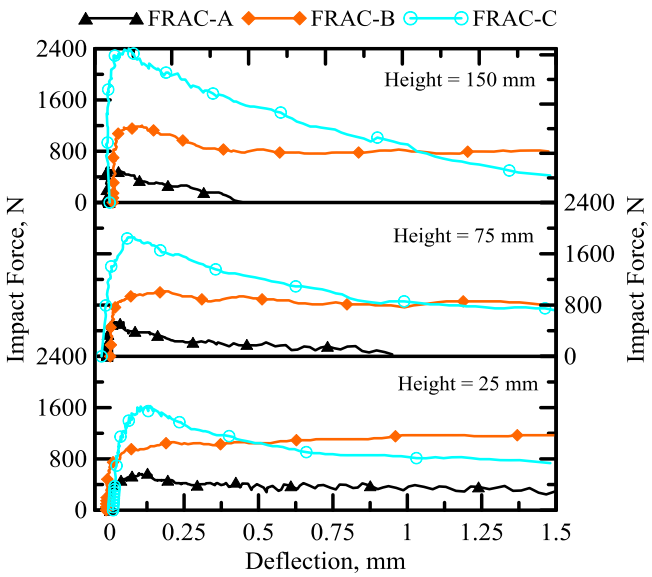

(a)

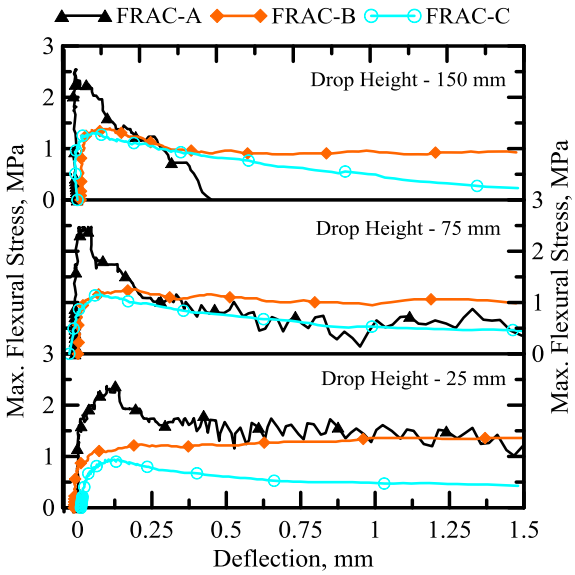

(b)

Figure 4-13 (a)-(b) : Size effect on FRAC specimen

Response of impact force against deflection of representative FRAC and AAC specimens can be observed in Figure 4-13(a) and Figure 4-14 (a). Rebound effect can be seen FRAC-C and AAC-C specimen under a drop height of 25 mm. Due to their comparatively large cross-sectional dimensions, the beams respond

as stiff beams under small drop height. They have enough resistance in them to avoid complete failure and has extra energy left in the system post the impact which results in the rebound of the impactor. The area under the impact load-deflection curve is the deformation energy that is initially progressively transferred from the hammer to the beam and then given back from the beam to the rebounding hammer; the area included inside the curve refers to the toughness / energy absorbed by the test specimen during impact [90].At higher drop heights of 75 and 150 mm, rebound effect is not recorded due to complete failure of the beam specimen. The area under the curve in the absence of rebound is the deformation energy which is progressively transferred from the hammer to the specimen, and is also the energy absorbed during the impact [91]. There is a significant improvement in the energy absorption capacities of both FRAC and AAC specimens with increasing cross-sectional dimensions, which highlights the size effect.

Response of flexural strength against defection of selected FRAC and AAC specimen can be studied in Figure 4-13(b) and Figure 4-14(b). Depth and width of the specimen mostly governs the flexural strength of these specimens. This results in reduction with increasing cross-sectional dimensions. Due to the size effect flexural strength for FRAC specimens varies between 1.0 - 2.4 MPa where as for AAC it varies between 1.3 to 2.4 MPa. Deformation capacity of both FRAC and AAC specimen improves with increasing cross-sectional dimension. This could be attributed to the increase in stiffness and resistance to impact loading.

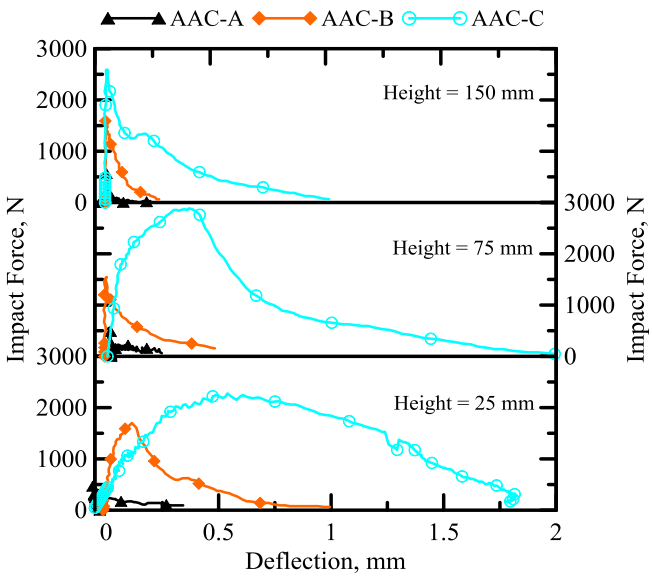

(a)

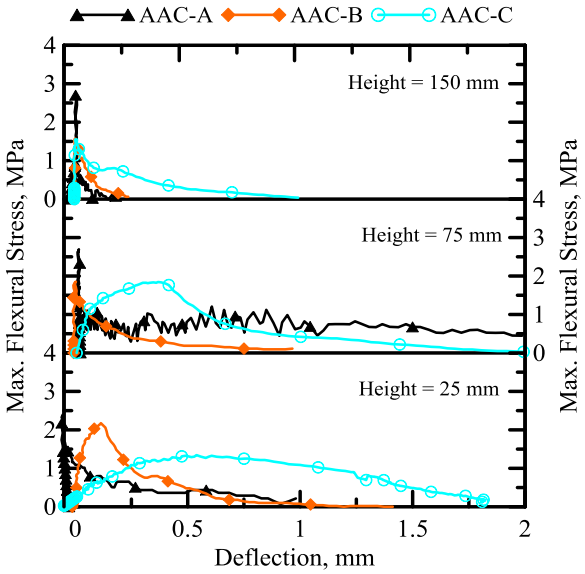

(b)

Figure 4-14 (a)-(b) : Size effect on AAC specimen subjected to impact loads

4.4.3 Comparison between FRAC and AAC specimen

Contribution of the short polymeric fibers towards toughness can be best understood by studying the flexural responses of FRAC and AAC. Fiber reinforcement helps in bridging the gaps created through cracks under tensile

loading, aiding in higher energy absorption capacity [1]. Typical damage mechanism involved could be explained to be associated with fiber de-bonding and nucleation of micro-voids [92]. Figure 4-15 (a) – (c) shows the comparison between impact responses of different dimensions of FRAC and AAC specimens tested under different input potential energies. In the absence of fibers, AAC is practically brittle by nature, and as clearly evident in the figures, it loses its structural integrity soon after peak load. There is hardly any resistance to propagation of tensile cracks and post-peak response involves unstable crack propagation and complete loss of load-carrying capacity [86]. FRAC specimens exhibit a well-defined post peak response due to the presence of the fibers. Peak strength is achieved in the non-linear part of the load-deflection response and is associated with strain hardening. There is an appreciable post peak response and is associated with large amount of energy dissipation and significant strain softening. Large area enclosed within the load-deflection response contributes to higher toughness and greater energy absorption capacity. However AAC exhibits marginally higher modulus of rupture and load carrying capacity than FRAC.

Figure 4-16 (a) – (c) summarizes the performance in term of flexural strength and initial stiffness (linear-part only) of three sizes of AC systems tested. Non-linear part of the load-deflection response after LOP is characterized by stiffness degradation.

Extent of stiffness degradation in the non-linear part was not evaluated in this current study. Flexural strength and initial stiffness recorded at different drop heights of the impactor show contrasting trends. AAC specimens show marginally

higher load carrying capacity than FRAC, hence when comparisons are made between same sized specimens, AAC has higher flexural strength values than FRAC.

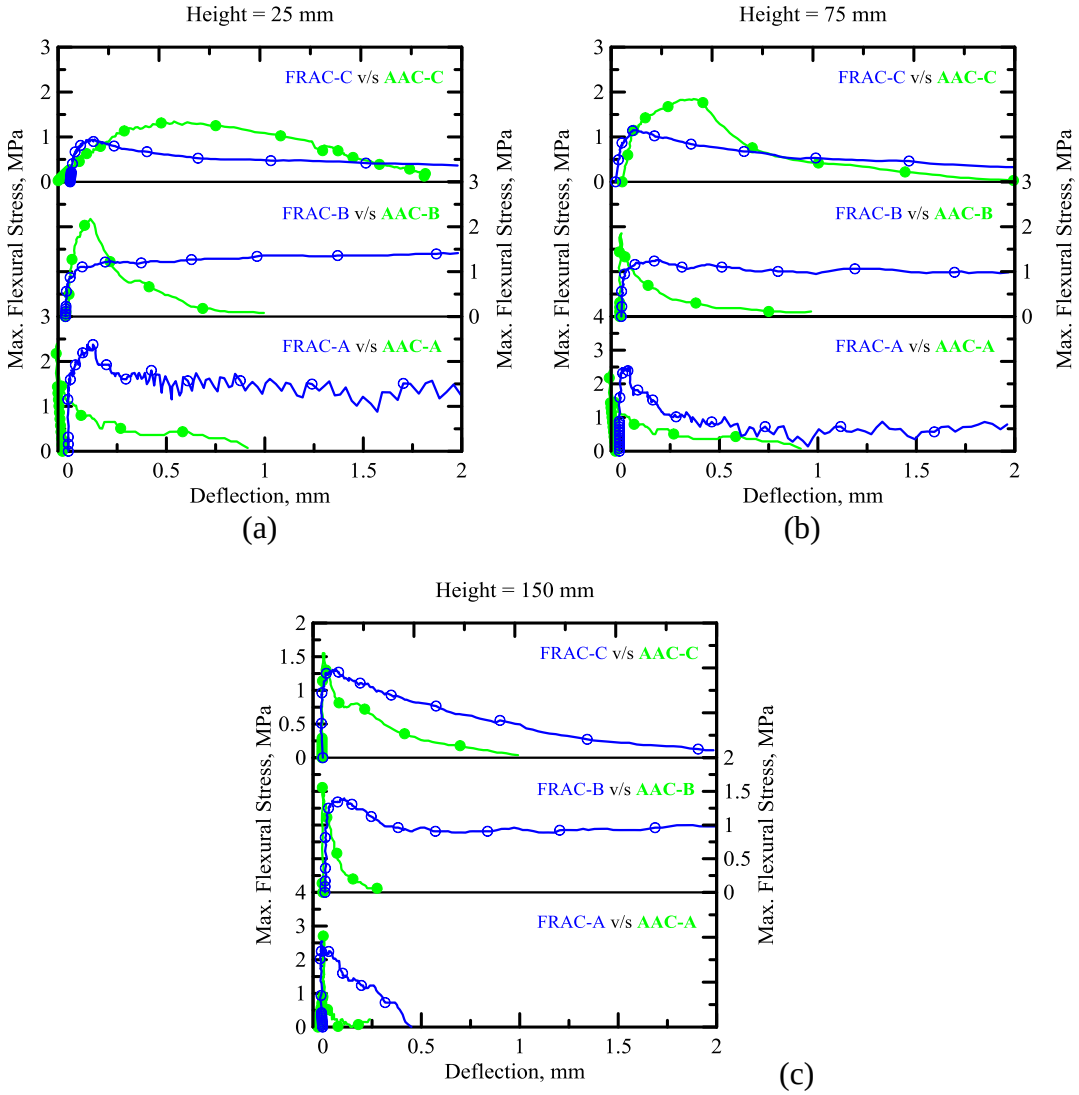

Figure 4-15 (a)-(c) : Comparison between FRAC and AAC under impact loading

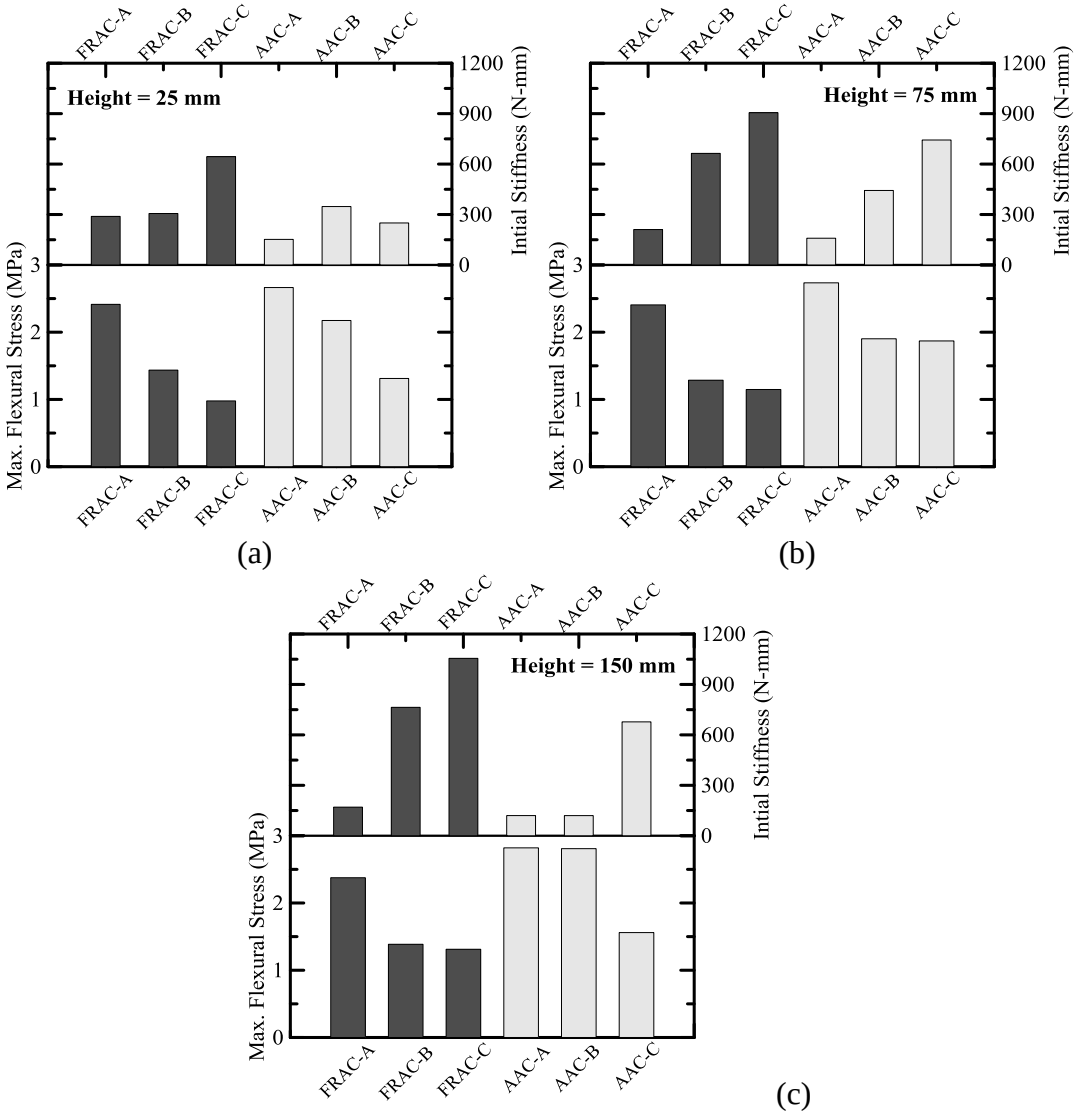

Figure 4-16 (a)-(c) : Flexural strength and initial stiffness of FRAC and AAC specimens

Rigidity or initial stiffness which is measured as the slope of the linear part of the load – deflection response, shows an increasing trend with increase in cross-sectional dimensions. This could be attributed to increase in load carrying capacity in case of large specimens. FRAC specimens however show higher rigidity when compared to AAC at matching drop heights of the impactor. Effect of increase in drop height has a significant effect on the stiffness of the

specimens. Maximum initial stiffness of the AC specimens can be observed at the drop height of 150 mm.

4.5 Energy Absorption

Assuming no frictional loss ($U_d = 0$) during the free fall of the hammer, the equation 2.4.1 is used to determine the input potential energy as a function of the drop height and mass of the hammer can be further simplified as in Equation 4-8 [1]**.**

$$U_i = mgH = \frac{1}{2}mv_0^2 = U_k + U_f \qquad \text{Equation 4-8}$$

Absorbed energy, U_k was determined for every drop height as shown in Figure 4-17. Energy absorption capacity, U_k of small sized specimens is very low, and there is marginal effect of drop height. FRAC-A has peak toughness value of about 3 J whereas AAC-A reported toughness value of < 1 J. AAC samples as discussed before has much lower energy absorption capacity than FRAC, because of its brittle nature. FRAC-C and AAC-C show matching response where in U_k increases between drop heights of 25 mm to 75 mm, and then decreases for drop height of 150 mm. FRAC-B and AAC-B show contrasting trends, wherein toughness of the former continues to increase with increasing drop height. For AAC-B however U_k first decreases between height of 25 mm and 75 mm, and then increases for the drop height of 150 mm. Such disparity in the toughness trends necessitated normalization against potential energy involved in the impact. A parameter, β defined as the ratio of the absorbed energy, U_k to the input potential energy, U_i is stated in Equation 4-9 [1].

$$\beta = \frac{U_k}{U_i}$$ Equation 4-9

Figure 4-17 shows similar declining trends of parameter, β across different sizes of FRAC and AAC specimens. A parabolic fit was used to highlight these trends.

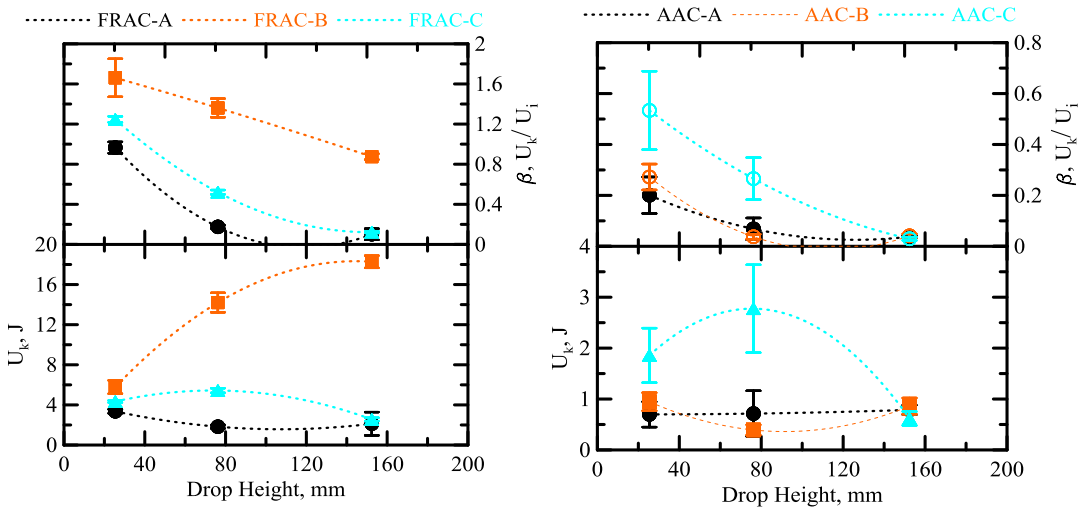

(a) (b)

Figure 4-17 (a)-(b) : Effect of drop heights on the absorbed energy and ratio of absorbed energy to the input potential energy for AC specimens

Potential energy as a function of drop height of hammer can be compared to the energy absorbed by the specimen during the impact event. This will address the energy absorption ability of AC systems further, as shown in Figure 4-18. At a fixed drop height of the hammer, FRAC-B type specimens show greater toughness or higher energy absorption ability amongst all FRAC beam type specimens due to their characteristic strain hardening behavior. However amongst AAC specimens, it is AAC-C which shows the maximum capacity which is much

less if compared to FRAC specimens.

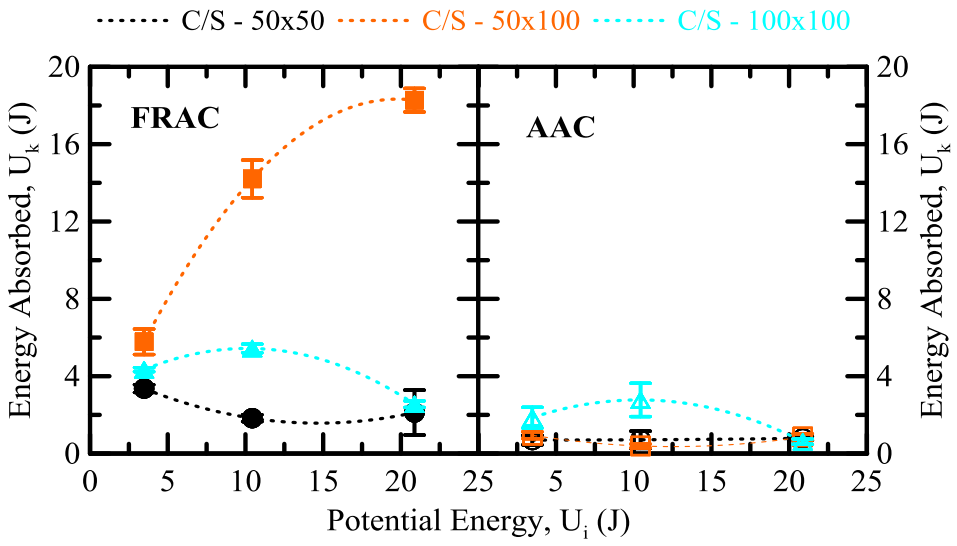

Figure 4-18 : Potential energy of the drop compared to the energy absorbed / toughness of AC

4.6 Crack Propagation

Crack growth under impact loading was studied using a high speed Phantom camera. Camera speed was set to 4000 fps, which was found to be adequate to capture different stages of the test. Image J software was used for converting the video to individual frames and for some elementary image analysis. Figure 4-19 and Figure 4-20 show the time lapse images of typical impact responses of FRAC-C and AAC-C specimens tested at drop height of 75 mm, respectively. Different stages of crack growth were further related to the load-deflection response. Seven points marked in the load-deflection plots for both FRAC-C and AAC-C could be related to the respective frames numbers. Each of these frames could be related to the experimental response in terms of time (T), load (P), deflection (δ), and crack width (w). Rebound effect could be

noticed in the load deflection response of FRAC-C specimen, which could be related to the frame titled F7. Deflection value recorded decreases from frame F6, signifying reduction in crack width due to rebound of the impactor.

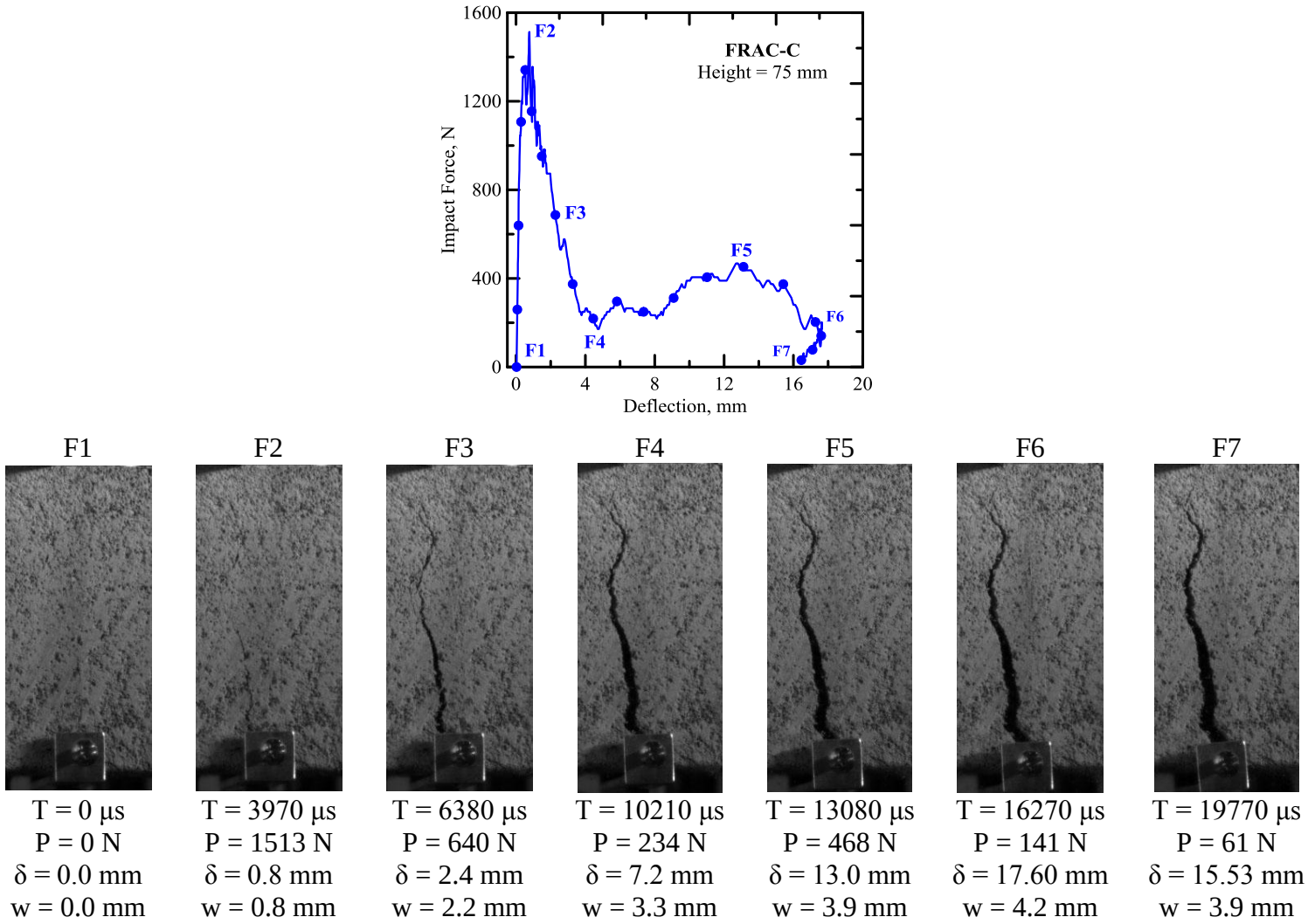

Figure 4-19 : Crack propagation of a representative FRAC-C specimen under a drop height of 75 mm

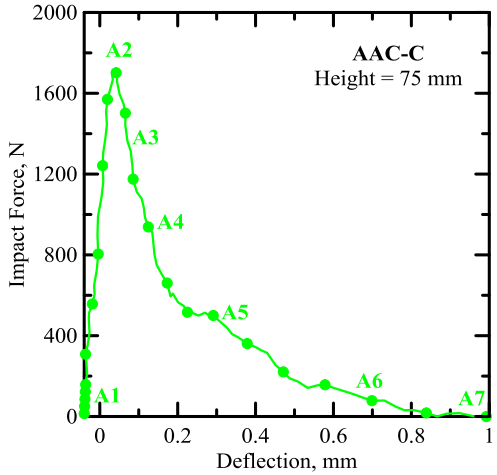

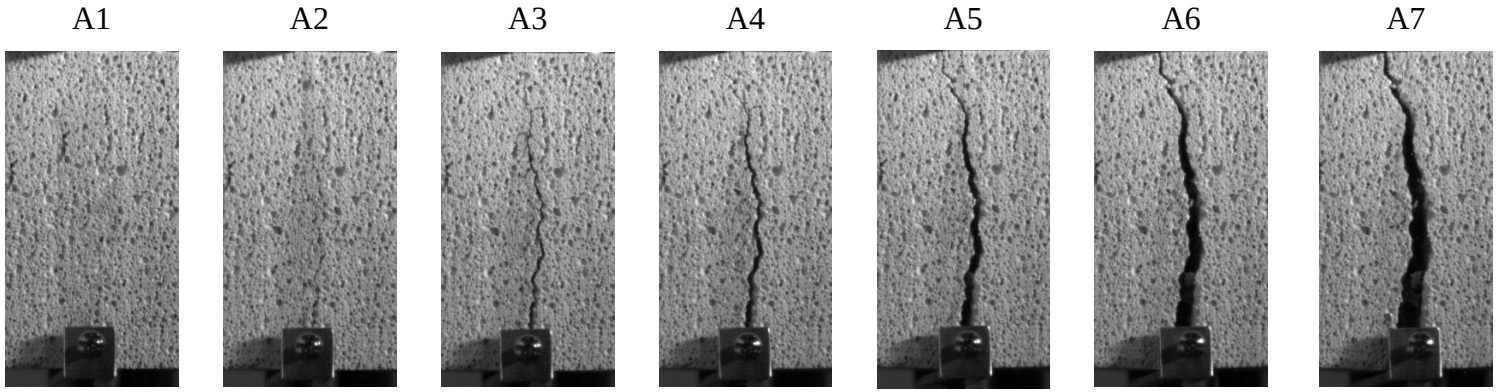

A1	A2	A3	A4	A5	A6	A7
T = 0 ms P = 0 N δ = 0.0 mm w = 0 mm	T = 1500 ms P = 1716 N δ = 0.0 mm w = 0.3 mm	T = 1840 ms P = 1441 N δ = 0.1 mm w = 0.7 mm	T = 2250 ms P = 987 N δ = 0.1 mm w = 1.3 mm	T = 2870 ms P = 515 N δ = 0.2 mm w = 2.0 mm	T = 3680 ms P = 174 N δ = 0.5 mm w = 3.4 mm	T = 4500 ms P = 1 N δ = 1.0 mm w = 5.4 mm

Figure 4-20 : Crack propagation of a representative AAC-C specimen under a drop height of 75 mm

Table 4-4 : Experimental results of FRAC specimens

Specimen Type (Dimensions)	Drop Height	Drop Velocity-Hammer	Velocity-Specimen	Strain Rate	Max Impact Force	Flexural Strength	Max Deflection	Potential Energy	Absorbed Energy	Initial Stiffness
	mm	mm/sec	mm/sec	sec^{-1}	N	MPa	mm	J	J	N/mm
FRAC-A (250 x 50 x 50)	25.4	706	689 (331)	2.5 (1.2)	549 (85)	2.41 (0.32)	17.70 (5.03)	3.48	3.36 (0.40)	289 (53)
	76.2	1223	1014 (77)	11.2 (0.8)	575 (125)	2.41 (0.33)	19.68 (0.09)	10.44	1.83 (0.36)	211 (50)
	152.4	1729	880 (85)	19.5 (1.9)	555 (194)	2.38 (0.65)	19.88 (0.21)	20.88	2.12 (2.32)	170 (60)
FRAC-B (250 x 50 x 100)	25.4	706	83 (94)	0.3 (0.3)	1214 (84)	1.44 (0.03)	11.18 (8.08)	3.48	5.78 (1.32)	306 (128)
	76.2	1223	965 (69)	10.7 (0.8)	1064 (99)	1.29 (0.09)	18.88 (0.73)	10.44	14.20 (1.95)	664 (105)
	152.4	1729	889 (179)	19.7 (4.0)	1129 (98)	1.39 (0.16)	19.55 (0.15)	20.88	18.27 (1.22)	764 (29)
FRAC-C (250 x 100 x 100)	25.4	706	86 (93)	0.3 (0.3)	1613 (299)	0.98 (0.24)	6.22 (3.05)	3.48	4.34 (0.21)	644 (144)
	76.2	1223	668 (266)	7.4 (2.9)	1819 (114)	1.15 (0.11)	16.68 (3.93)	10.44	5.44 (0.45)	906 (220)
	152.4	1729	945 (97)	20.9 (2.1)	2160 (229)	1.31 (0.13)	17.92 (0.79)	20.88	2.55 (0.34)	1055 (178)

Table 4-5 : Experimental results of AAC specimens

Specimen Type (Dimensions)	Drop Height	Drop Velocity-Hammer	Velocity-Specimen	Strain Rate	Max Impact Force	Flexural Strength	Max Deflection	Potential Energy	Absorbed Energy	Initial Stiffness
	mm	mm/sec	mm/sec	sec^{-1}	N	MPa	mm	J	J	N/mm
AAC-A (250 x 50 x 50)	25.4	706	896 (132)	3.7 (0.4)	546 (112)	2.66 (0.70)	19.59 (0.21)	3.48	0.26 (0.48)	152 (57)
	76.2	1223	920 (383)	12.4 (2.1)	558 (28)	2.73 (0.18)	19.72 (0.04)	10.44	0.71 (0.90)	159 (32)
	152.4	1729	1012 (46)	22.4 (1.0)	524 (95)	2.81 (0.70)	19.77 (0.35)	20.87	0.79 (0.19)	120 (20)
AAC-B (250 x 50 x 100)	25.4	706	437 (237)	1.6 (0.9)	1726 (190)	2.17 (0.25)	16.41 (7.93)	3.48	0.95 (0.35)	347 (143)
	76.2	1223	992 (165)	11.0 (1.8)	1541 (417)	1.90 (0.51)	19.95 (0.39)	10.44	0.39 (0.20)	443 (162)
	152.4	1729	1013 (96)	22.4 (2.1)	1706 (383)	1.92 (0.51)	19.51 (0.87)	20.87	0.86 (0.32)	379 (100)
AAC-C (250 x 100 x 100)	25.4	706	4 (3)	0.02 (0.01)	2182 (340)	1.31 (0.23)	1.30 (0.89)	3.48	1.86 (1.07)	250 (55)
	76.2	1223	453 (406)	5.0 (4.5)	2943 (581)	1.87 (0.33)	11.82 (8.87)	10.44	2.77 (1.72)	743 (671)
	152.4	1729	802 (42)	17.8 (0.9)	2539 (169)	1.56 (0.10)	17.42 (0.09)	20.87	0.62 (0.27)	677 (168)

Table 4-4 and Table 4-5 present the average values of the results obtained from the analysis of FRAC and AAC specimens, respectively. Average and standard deviation values of 5 replicate specimens are reported in these tables in adjacent rows. Analysis was done using the MATLAB code described in the previous sections. Absorbed energy (toughness) and deformation capacity of the specimens are reported directly from the output of the computer code wherein entire history of the load-deflection response is considered. Accurate toughness values need to be determined by considering individual responses which has to be reported against a pre-determined deflection value (actual deformation capacity). This deflection value could be assumed at load level at which specimen does not have any significant load carrying capacity.

4.7 Conclusions

Impact response of aerated concrete was studied using an instrumented test based on a three-point bending configuration. Time-history of the load, acceleration, deflection responses, and absorbed energy of the specimen were obtained and discussed in details. Plain autoclaved aerated concrete (AAC) and fiber-reinforced aerated concrete (FRAC) were tested for their flexural impact behavior. The effect of impact energy on the mechanical properties was investigated for various drop heights of 25 mm, 75 mm, and 150 mm and different specimen sizes. It was observed that dynamic flexural strength under impact tests was more than twice higher than the static flexural strength. FRAC showed more than thirty times higher flexural toughness compared to AAC which can be attributed to the role of short fibers in bridging the flexural cracks and absorbing

the impact energy. Rebound effect was observed for larger specimens under low drop heights. The instrumented impact test performed in this chapter was found to be a good method for studying the impact response of cement-based materials such as aerated concrete products. The same testing procedure was used to investigate the impact resistance of sandwich beams with aerated concrete core.

5. IMPACT RESPONSE OF SANDWICH BEAMS WITH AERATED CONCRETE

Behavior of AR-Glass textile reinforced stress skin layer type sandwich composite with aerated concrete was investigated under static flexural and high strain rate impact loads. Aerated concrete core was chosen for this study due to its unique characteristics of being a light-weight, pseudo-ductile material with good thermal efficiencies [93]. Aerated concrete is characterized by a discontinuous pore structure, with almost 80% of the hardened structure being constituted by with a general ratio of 2.5:1.0 air-pores to micro-pores [94]. This results in low-density structure with poor compressive strength. This limits the applicability of this material to one-two stored residential and commercial structures only.

Idea behind developing this unique cement-based sandwich composite is to improve some of the mechanical properties of the aerated concrete core with textile reinforcement at the top and bottom of the core as shown in Figure 5-1. Key features of this type of layered composite are the ease of manufacturing, anchorage and bond development between the textile skin and aerated concrete core material. Proper characterization of a novel composite requires understanding the behavior of the material subjected to high loading rates. Performance of the composite under different strain rates, energy absorption capacity and modes of failure are pre-requisites for optimal design considerations [93]. This study involves testing the sandwich composites under static flexural tests and high strain – dynamic impact tests.

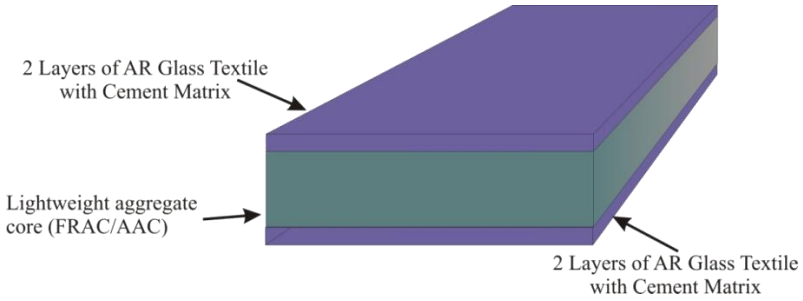

Figure 5-1 : Macro-structure of sandwich panel

Sandwich composites are known for their applications in naval, aerospace industries and defense structures which may be exposed to shock loading. They are typically considered as light-weight sections with high load-bearing capacity, damage tolerance and impact resistance. Dynamic response of these composites is mainly dependent of the properties of the skin and core material and interface bond strength [95].

5.1 Experimental Program

5.1.1 Material Properties and Mix Design

Bonded AR glass fabric consisting of a perpendicular set of yarns (warp and weft) which were glued at the junction points was used. Density of the fabric in both warp and weft directions was four yarns per centimeter and was manufactured by NEG Glass. 400 filaments of fiber of diameter 13.5 μm constitute a fiber bundle of diameter 0.27 mm. Tensile strength of this textile was in range of 1270 – 2450 MPa and modulus of elasticity of 78 MPa [93]. As evident in Figure 5-1 , two layers of textile reinforced cementitious matrix was used in the sandwich composites. Each of these layers consists of 2 lines of AR glass textile embedded along with cement matrix. The textile were first cut and trimmed down using electronic cutting tools to the size of 300 mm x 300 mm

sized planes from the main textile roll. A partial fly-ash substituted cement based mix design was used in the matrix as mentioned in Table 5-1. Each of the ingredients of the mixture was weighed separately and the mixing of the paste was done with a high speed mixing machine for 5 minutes. After mixing of the cement paste a precisely weighed amount of paste is placed for each line of AR-Glass textile. Evenness of the spread of the matrix is ensured in each layer to prevent delamination of the textile skins. Various stages of the manufacturing procedure of the sandwich composite can be seen in Figure 5-2. 28 day average compressive strength of three cylinders made with this cementitious matrix was found to be 22 MPa, with a standard deviation of 2 MPa.

Table 5-1 : Mix Design of Cementitious Matrix

Constituents:	Weight (in grams)
Portland Cement (Type I/II)	900
Water	180
Fly Ash (Class F)	310
Super plasticizer (SP Melflux 4930F)	2

Two types of aerated concrete were used as the core material - autoclaved aerated concrete (AAC) and fiber-reinforced aerated concrete (FRAC). Influence of the material properties of the core material have been described in the following sections. Aerated concrete blocks of dimension 300 mm (L) x 300 (B) mm were used in this study. Depth of these blocks was varied between 50 mm and 100 mm to understand the size effect.

Stage A Stage B

Stage C Stage D

Figure 5-2 : Fabrication process of sandwich composites

A mechanical punching machine was used to prevent delamination, unsoundness of the system and ensure perfect bond between the interfaces. Post manufacturing treatment consists of wrapping the sandwich panel with plastic films, followed by curing inside temperature and moisture controlled chamber for 28 days. To maintain consistency in the curing conditions, temperature of the chamber was maintained at 23 deg. C with 100 % relative humidity. After curing, the panels were cut to proper dimensions using a mechanical saw. The outside edges were trimmed out and rejected. Each of these panels was then further trimmed down to five small beams of dimensions of 250 mm (L) x 50 mm (B).

The depth of the specimen was maintained as 50 mm and 100 mm, as mentioned earlier. Dimensions and types of specimens investigated in this study have been summarized in Table 5-2.

Table 5-2 : Testing Schematics

Designation of Sandwich Specimens		Core Material	Dimensions, mm	
SWFRAC	A	FRAC	50 x 50 x 250	Square X-Sec.
	B		50 x 100 x 250	Rectangle X-Sec.
SWAAC	A	AAC	50 x 50 x 250	Square X-Sec.
	B		50 x 100 x 250	Rectangle X-Sec.

5.1.2 Static Flexural Tests

Three point bending tests were performed using a servo-hydraulic MTS machine with a load cell capacity of 222 KN under closed loop conditions. The tests were run under cross-head displacement control at the rate of 1.3 mm/min. Deflections at the mid-span were measured using a linear variable differential transformer (LVDT). Test data recorded from the test includes deflection (LVDT), bending load (load cell) and cross head displacement (actuator).

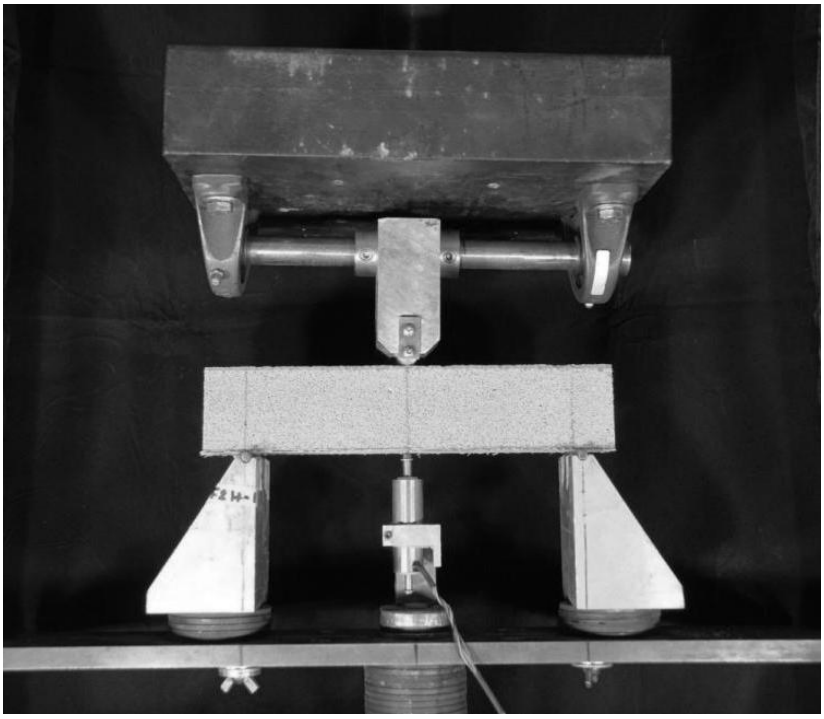

Figure 5-3 : Experimental setup of static flexural tests on sandwich panels

Five sandwich specimens with FRAC as the core material were tested and then compared to the results obtained from FRAC core material. Dimensions of specimens tested are 50 (mm) x 50 (mm) x 250 (mm) and the span was maintained as 200 mm. Results obtained from these tests have been mentioned in the subsequent sections.

5.1.3 Flexural Impact Test

A drop weight type impact test setup based on free fall drop of instrumented hammer described in the previous chapter was used for this study. Drop height of the impact was adjusted to understand the impact resistance of these sandwich composites. The results obtained were then compared to the performance of the plain AC core under similar loading conditions. The

experimental setup used in this study is shown in Figure 5-4. Impact response of these composites, were recorded with a high-speed digital camera (Phantom v.7).

Figure 5-4 : Experimental setup of impact tests on sandwich panels

5.2 Discussion and Analysis

The experimental response of both static flexural and high speed impact tests was analyzed using computer programs written using MATLAB. They were used to smoothen and filter the raw data and calculate some experimental parameters such as stress, stiff, toughness, etc. The code written for impact test had an additional feature of reducing the experimental data based on user defined selection of the actual range of impact. Figure 5-5 shows the analyzed response obtained for the static tests conducted on five sandwich beams. Displacement of the test specimens beyond working range of the LVDT, were recorded using the actuator displacement of testing rig.

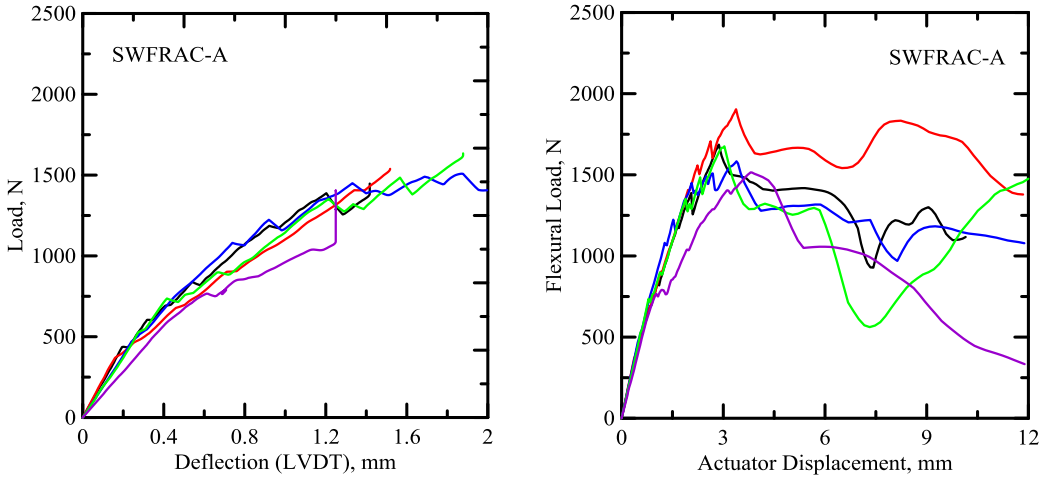

(a) (b)

Figure 5-5 : Replicates of SWFRAC tested under static load; (a) Deflection (LVDT) vs. Load Response; (b) Displacement (Actuator) vs. Load Response

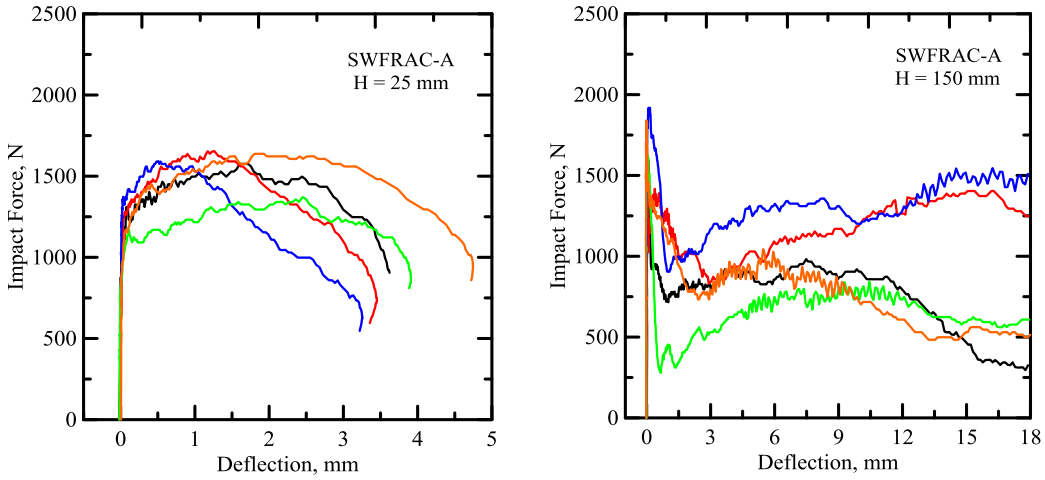

(a) (b)

Figure 5-6 : Replicates of SWFRAC tested under impact loading; (a)Drop height of 25 mm; (b) Drop height of 150 mm

Replicates of sandwich beams (SWFRAC) tested at two different drop heights (25 mm and 150 mm) of the impactor are shown in Figure 5-6. The effect of textile reinforcement, influence of the core material, effect of drop height and effect of specimen have been discussed in the subsequent sections.

5.2.1 Sandwich Effect

Static flexural tests were also conducted on core FRAC material under displacement control rate of 0.4 mm/min. Five beams of FRAC material of dimension 50 (mm) x 50 (mm) x 250 (mm) and the span was maintained as 200 mm. Results were then compared to the sandwich beams as shown in Figure 5-7.

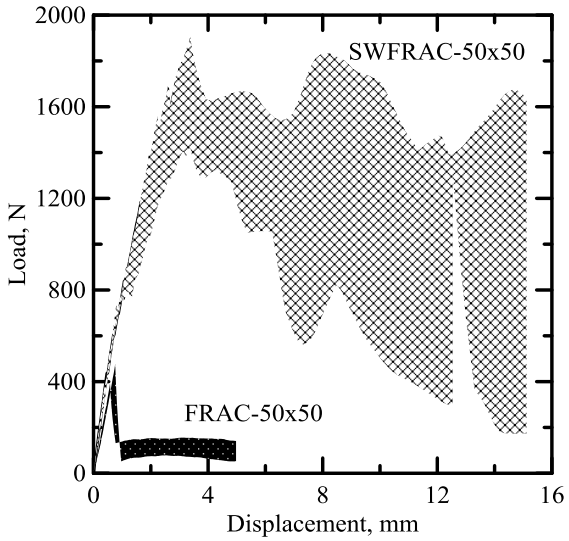

Figure 5-7 : Comparison between FRAC and SWFRAC under static loads

Image sequence captured from the static flexural tests on FRAC-A and SWFRAC-A has been shown in Figure 5-8 and Figure 5-9, respectively. Time, T (min), deflection, δ (mm) and flexural strength, σ (MPa) have been presented sequentially. Fiber bridging action of plain FRAC core specimens under flexural loads is clearly evident in Figure 5-11. This explains the pseudo-ductile response of this material and influences the energy absorption properties of this material. Also evident is the enhancement in flexural strength from 0.5 MPa for plain FRAC specimen to 2.9 MPa for sandwich specimen. Deformation capacity also doubles due to the textile reinforcement on the aerated concrete core.

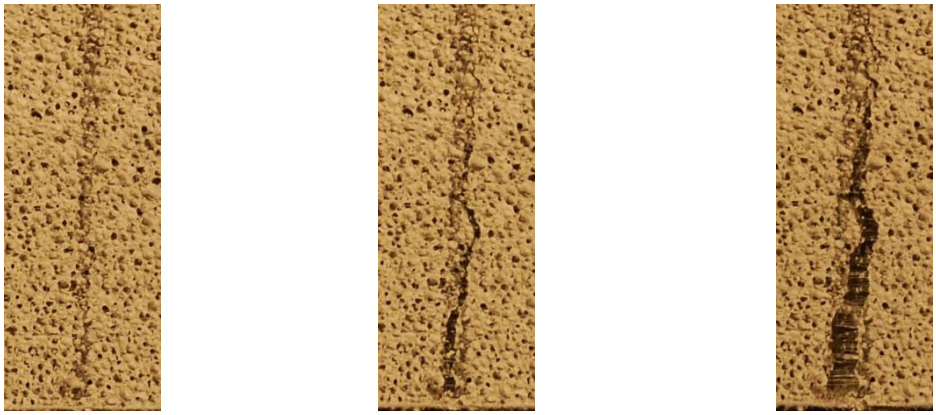

Stage A Stage B Stage C

[T = 0 δ = 0 σ = 0] [T = 7 δ = 1.9 σ = 0.6] [T = 14 δ = 4.5 σ = 0.5]

Figure 5-8 : FRAC-A specimen under static flexural loading

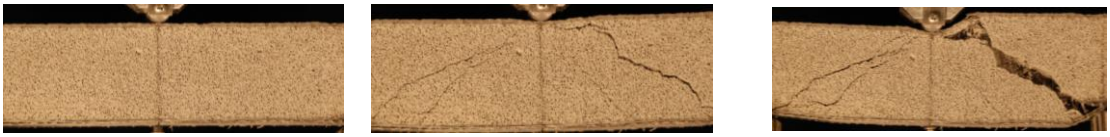

Stage A Stage B Stage C

[T = 0 δ = 0 σ = 0] [T = 7 δ = 4.1 σ = 3.4] [T = 14 δ = 9.4 σ = 2.9]

Figure 5-9 : SWFRAC-A specimen under static flexural loading

Impact tests were conducted on sandwich beams with FRAC and AAC as the core at three different drop heights 25 mm, 75 mm, and 150 mm. Results obtained were again compared with the impact tests done on the core material. Depth of the specimens used for this comparisons were maintained as 50 mm. Figure 5-10 summarizes the impact resistance of the sandwich beams (dots only) and plain core beams (solid line). Effect of textile is clearly evident in terms of load carrying and deflection capacity. With the increase in the peak load response, flexural strength of the sandwich beams also increases to almost 3 times, when compared to the plain core material. The presence of textile reinforcement also

affects the energy absorption capacity of such composites. Energy absorption (toughness) is measured as the area enclosed in the load-deflection response. This is calculated using the computer program described in the previous chapter. The energy absorption capacity for sandwich beams with AAC as the core material is almost 30 times more than the brittle AAC core material. The effect of textile reinforcement for FRAC is however less profound with about 8 times increase in toughness.

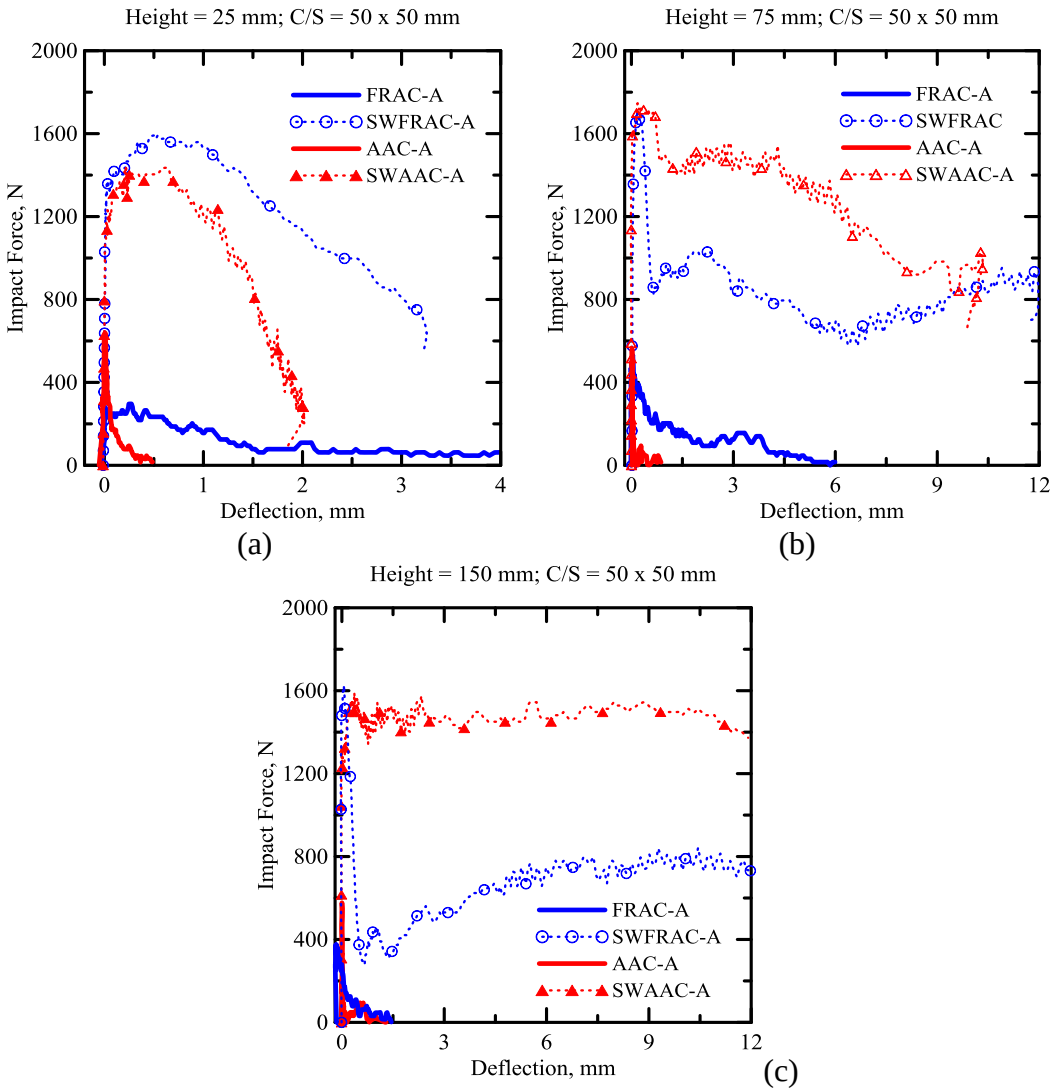

Figure 5-10 : Effect of textile reinforcement on FRAC (blue) and AAC (red)

Increase in flexural strength and initial stiffness (linear part of load response) is shown in Figure 5-11. Size effect of the specimen which controls the flexural strength of specimens under flexural loading is discussed in the following sections. Effect of textile reinforcement on the initial stiffness of the sandwich composites is more profound for size "A" specimens with about 5 times increase for both SWFRAC and SWAAC. However there is only moderate increase for size "B" specimens (depth > width). This could be attributed to shear failure due to difference in interface properties and effect of delamination.

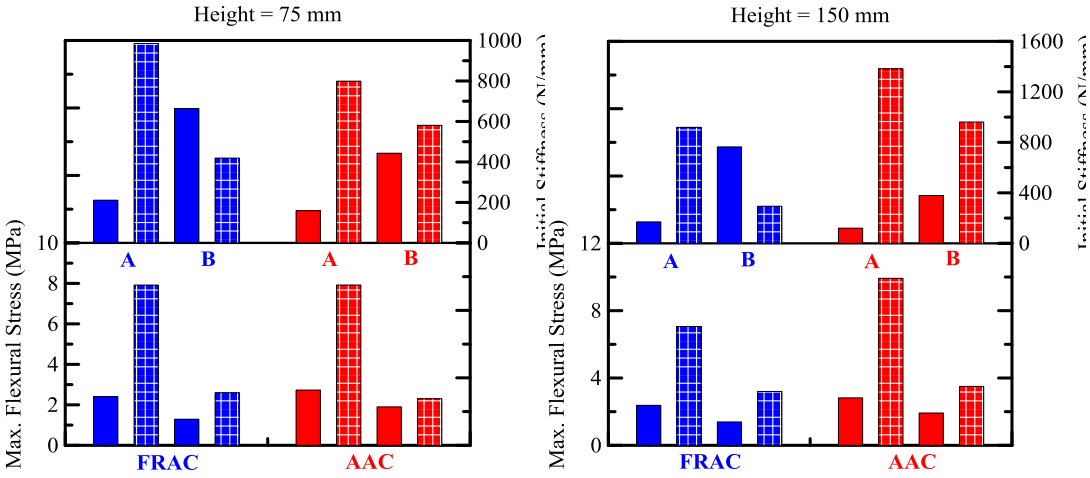

Figure 5-11 : Effect of textile reinforcement on flexural strength and stiffness under (a) Drop height of 75 mm; (b) Drop height of 150 mm under impact loading

5.2.2 Effect of the core material

Figure 5-12 compares the response of sandwich beams with FRAC and AAC as the core material under impact loading at drop height of 300 mm. In the absence of internal fiber reinforcement, AAC acts as a brittle material when subjected to impact loading. As evident SWFRAC-B has slightly higher load carrying capacity of 3400 N than SWAAC-B which is at about 3300 N. Maximum

flexural strength of SWFRAC-B at a drop height of 300 mm is 4 MPa, whereas for SWAAC-B it is 3.7 MPa. Initial stiffness (about 1900 N/mm) and deformation capacity (about 18 mm) is similar for both of these sandwich composites. Also as clearly evident, energy absorption (toughness) of SWFRAC-B (25 J) is higher than SWAAC-B (20 J) at the same input potential energy of 42 J.

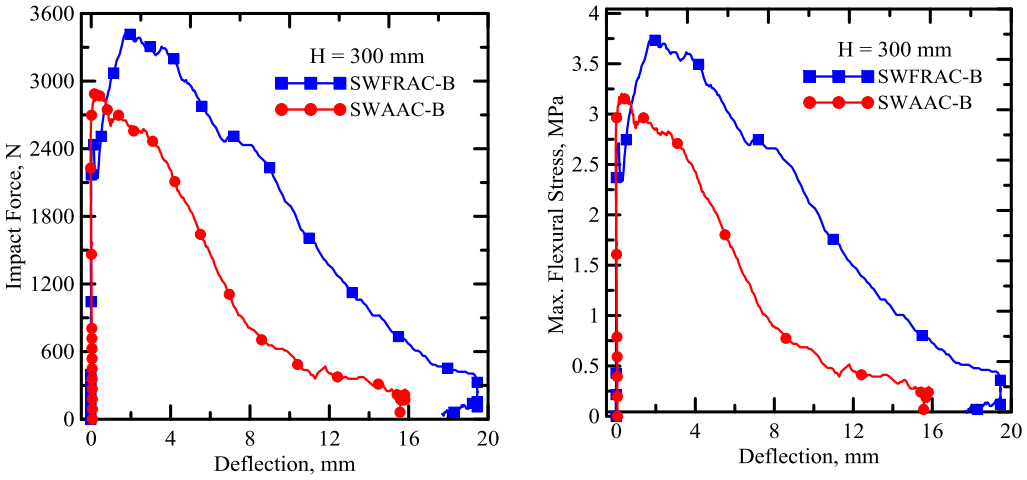

Figure 5-12 : SWFRAC (blue) versus SWAAC(red(; (a) Impact force versus deflection; (b) Flexural Strength versus deflection

SWFRAC-A SWAAC-A

Figure 5-13 : Crack propagation of SWFRAC-A and SWAAC-A under different heights of the impactor; (a) 25 mm; (b) 75 mm; (c) 150 mm

Propagation of cracks under impact loading on sandwich beams can be seen in Figure 5-13. Presence of polymeric fibers in FRAC core materials helps in controlling the crack propagation through fiber bridging action, as previously demonstrated. Innate brittleness of the AAC material dictates the distributed cracking mechanism as seen in sandwich beams with AAC as the core material. As expected damage caused due to sudden drop of the impactor is much less at smaller drop heights of 25 mm. The crack width and crack intensity can be easily distinguished at higher drop heights of 75 mm and 150 mm of the impact head. At this point, it is also important to understand the effect of the drop height of the hammer on the impact response of these composites.

5.2.3 Effect of drop height of the impactor

Figure 5-14 summarizes the responses of both types of sandwich beams at four different drop heights. There is an insignificant difference in the maximum load carrying capacity (about 1500 N) for size "A" sandwich beams at drop heights of 25 mm (red), 75 mm (blue) and 150 mm (green). Larger cross-section beams (size "B") beams are expected to have more load carrying capacity hence their performance was also evaluated at an additional drop height of 300 mm (purple). As evident, effect of drop height is more pronounced for the size "B" beams with a rectangular cross-section. For SWAAC-B beams, peak load increases from 2250 N (75mm) to 2620 N (150 mm) and to 2920 N (300 mm). Whereas for SWAAC-A which show slightly more impact resistance, load increase from 2250 N to 2950 N and shows peak load of 3430 N at 300 mm drop. Deformation capacity and energy absorption capacity of all sandwich beams also

increase with increasing drop height of the loading head. This signifies that textile reinforcement improves the toughness and resistance of the beams under impact loads. The beams could retain their strength and did not undergo complete failure. This is the key aspect of the sandwich beams.

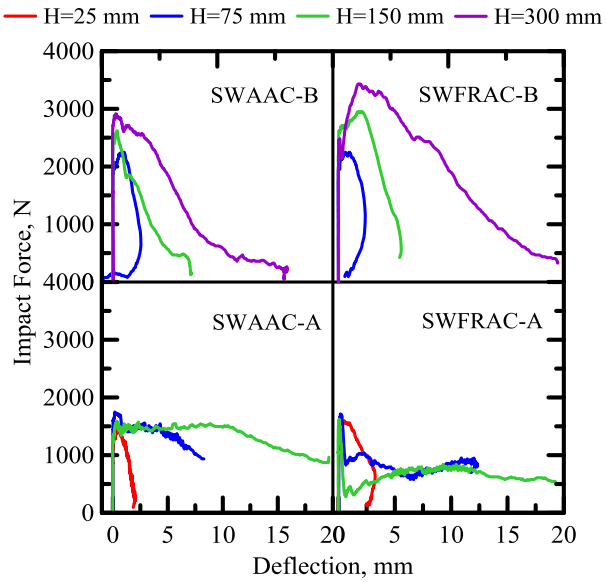

Figure 5-14 : Effect of drop height of the impactor

5.2.4 Size Effect

Size effect on sandwich beams was studied with two cross-sections: square and rectangle. It is to be noted that the span of beams tested under three-point bending configuration were maintained constant at 250 mm. Width of the specimens was maintained constant at 50 mm, whereas the depth was varied between 50 mm and 100 mm. This affects the apparent flexural strength with smaller cross-section beams (size “A”) showing higher strength than size “B” beams. Effect of the specimen cross-section is shown in Figure 5-15. The dotted lines represent size “A” beams whereas the solid lines represent size “B” beams.

The results were summarized for two different drop heights 75 mm and 150 mm and shown. Maximum average flexural strength of SWFRAC-A beams was 7.9 MPa at drop height of 75 mm; whereas for SWFRAC-B it was only 3.2 MPa at a drop height of 150 mm. Similarly for SWAAC-A beams, maximum average strength was 9.9 MPa and 3.5 MPa for SWAAC-B at a drop height of 150 mm.

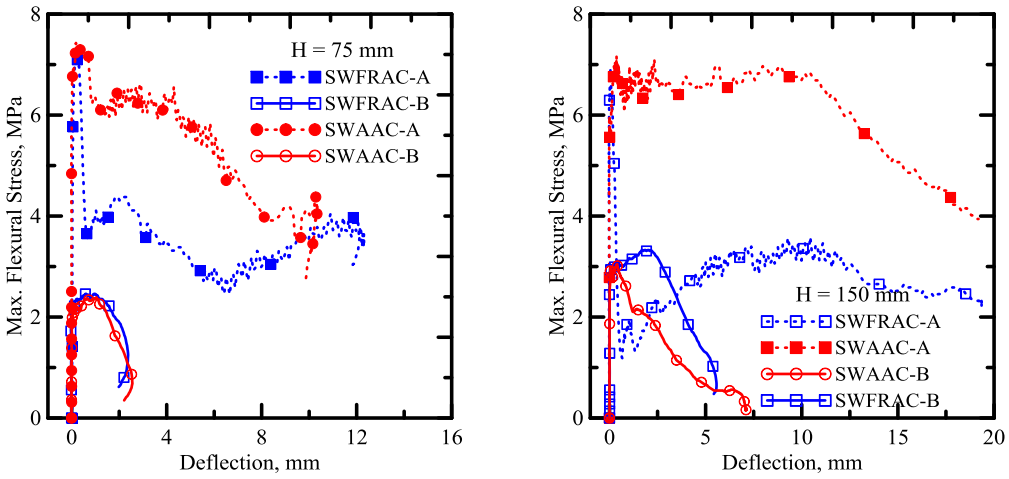

Figure 5-15 : Size effect on SWFRAC (blue) and SWAAC (red) beams

5.2.5 Energy Absorption

Energy response of the sandwich beams were compared to the tests results of the core material at similar drop heights. Energy absorbed is measured via two parameters – toughness (U_k) which is the area enclosed within the load-deflection curve and a normalized parameter, β (U_k/U_i). Parameter, β is the ratio between the energy absorbed by the specimen during an impact event (U_k) and the potential energy of the impact (U_i). Potential (input) energy is controlled by the height and weight of the dropping mass. Loss of energy due to friction is neglected, as frictionless bearings and drop columns used as a part of impact test setup controls

the loss of energy due to friction. Energy absorption capacity of sandwich beams of size "A" were compared to the plain core in Figure 5-16.

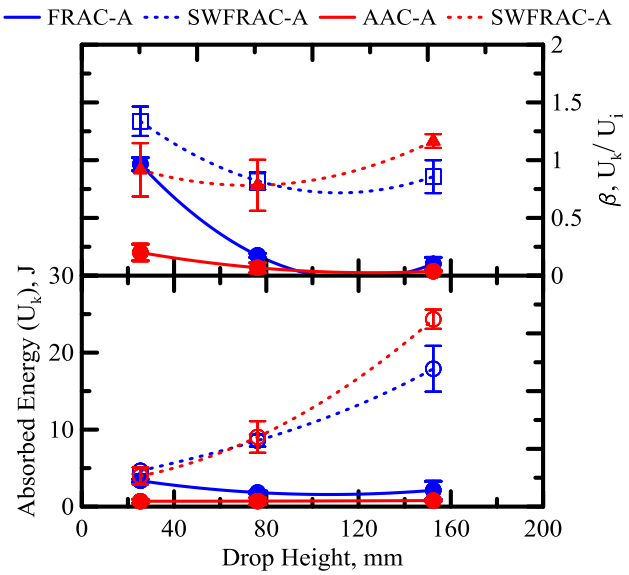

Figure 5-16 : Effect of textile reinforcement on energy absorption

As can be clearly seen, the plain AAC core material (red solid line) because of its brittle nature has very less toughness (> 1 J) signifying complete failure under impact loads at three different drop heights (25 mm, 75 mm, and 150 mm). Presence of randomly oriented polypropylene fibers inside FRAC core enhances its energy absorption capacity as stated earlier. At drop height of 25 mm, FRAC specimen (blue solid line) has the maximum energy absorption capacity of about 3 J. At higher drop heights, however the toughness of the FRAC specimen is reduced and complete loss of load carrying capacity is predominant. With textile reinforcement however this trend can be reversed. Toughness of SWAAC-A (red dotted lines) beams is as much as 30 times more than its plain AAC core. However for SWFRAC-A beams (blue dotted lines) this trend is less dramatic, wherein energy absorption capacity increases by about 8 times due to

the presence of textile layers. It is to be noted that maximum toughness of the sandwich beams were observed at drop height of 150 mm, with SWAAC-A having an average toughness value of 24 J; and SWFRAC-A has an average toughness of 18 J.

5.3 Crack Propagation

Cracks pattern of sandwich beams with FRAC core under static flexure loading can be seen in Figure 5-17. Bottom view of the specimen is shown in part (a) of the figure wherein the flexural cracks at the bottom TRC layer can be clearly seen. A side view of the sandwich is shown in part (b), wherein diagonal tension cracks and shear cracks can be seen emanating from the region near the bottom supports. The top textile layer of the composite is characterized by compression failure under the loading head. Part (c) shows the magnified side view image of the sandwich panels captured using a microscopic camera. Diagonal tension cracks are clearly evident. Effects of fiber pullout in the core and de-lamination of the top TRC layer can also be observed.

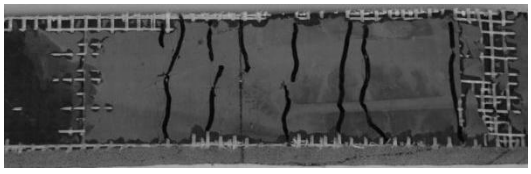

a

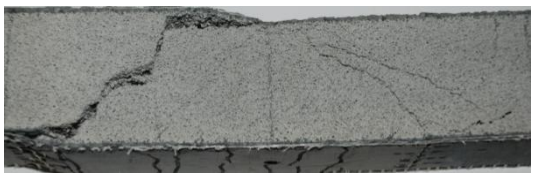

b

c

Figure 5-17 : Crack propagation of SWFRAC beams under static load

Development of cracks under impact loading was studied using a Phantom (v.7) high speed camera. Figure 5-18 (a-b) and Figure 5-19 (a-b) shows the typical behavior of SWFRAC-B and SWAAC-B beams at a drop height of 300 mm, respectively. Frames numbers are numbered from F1 – F8 and A1 – A8 as mentioned in Figure 5-18(a) and Figure 5-19(a). They can be associated with time (T), load (P), deflection (δ) and flexural strength (σ) for SWFRAC-B and SWAAC-B, respectively as mentioned in Figure 5-18(b) and Figure 5-19(b). Careful observations of frames F8 and A8 would suggest the effect of rebound wherein the deflection value recorded decreases with increase in impact load. This is dependent on the relative stiffness and strength of the material and also the loading conditions.

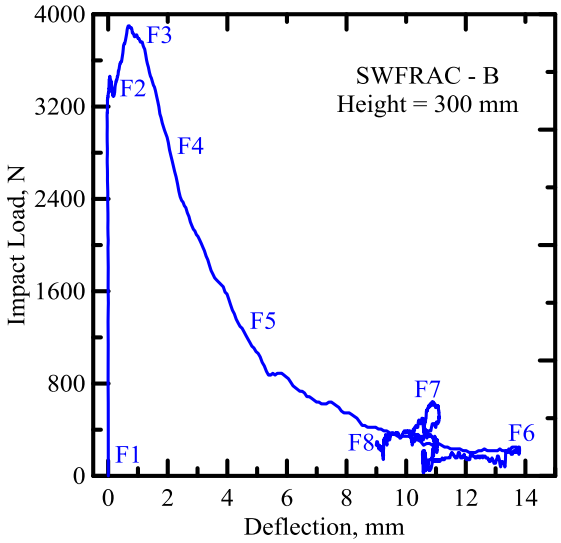

(a)

Figure 5-18 : Typical Load-Deflection response of a SWFRAC-B beam under impact load

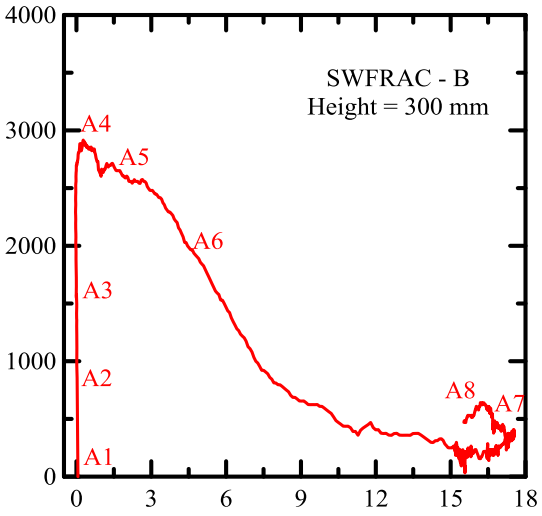

(a)

Figure 5-19 : Typical Load-Deflection response of a SWAAC-B beam under impact load

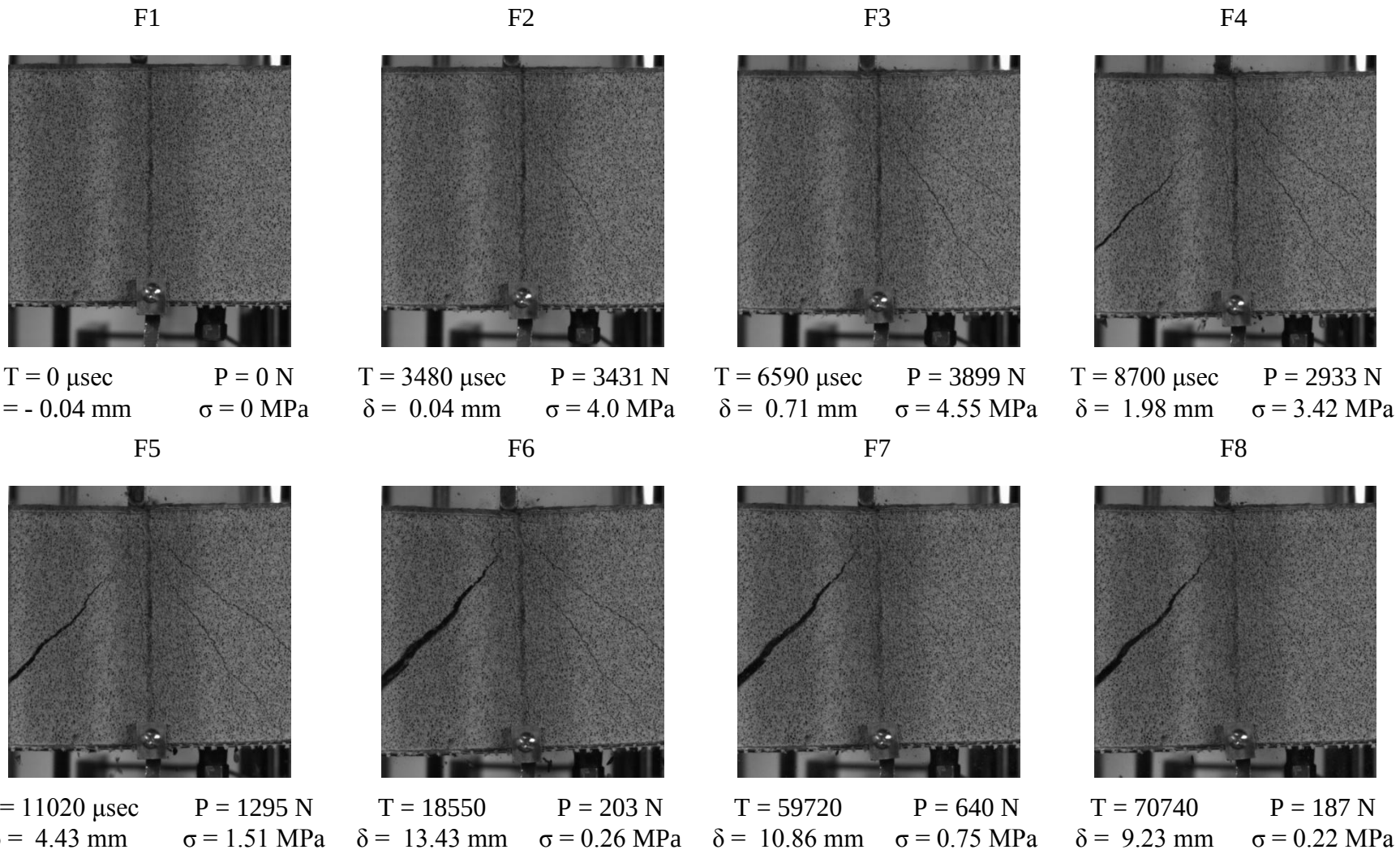

Figure 5-18 (b) : Crack propagation of SWFRAC-B beam under impact loading (Drop Height = 300 mm)

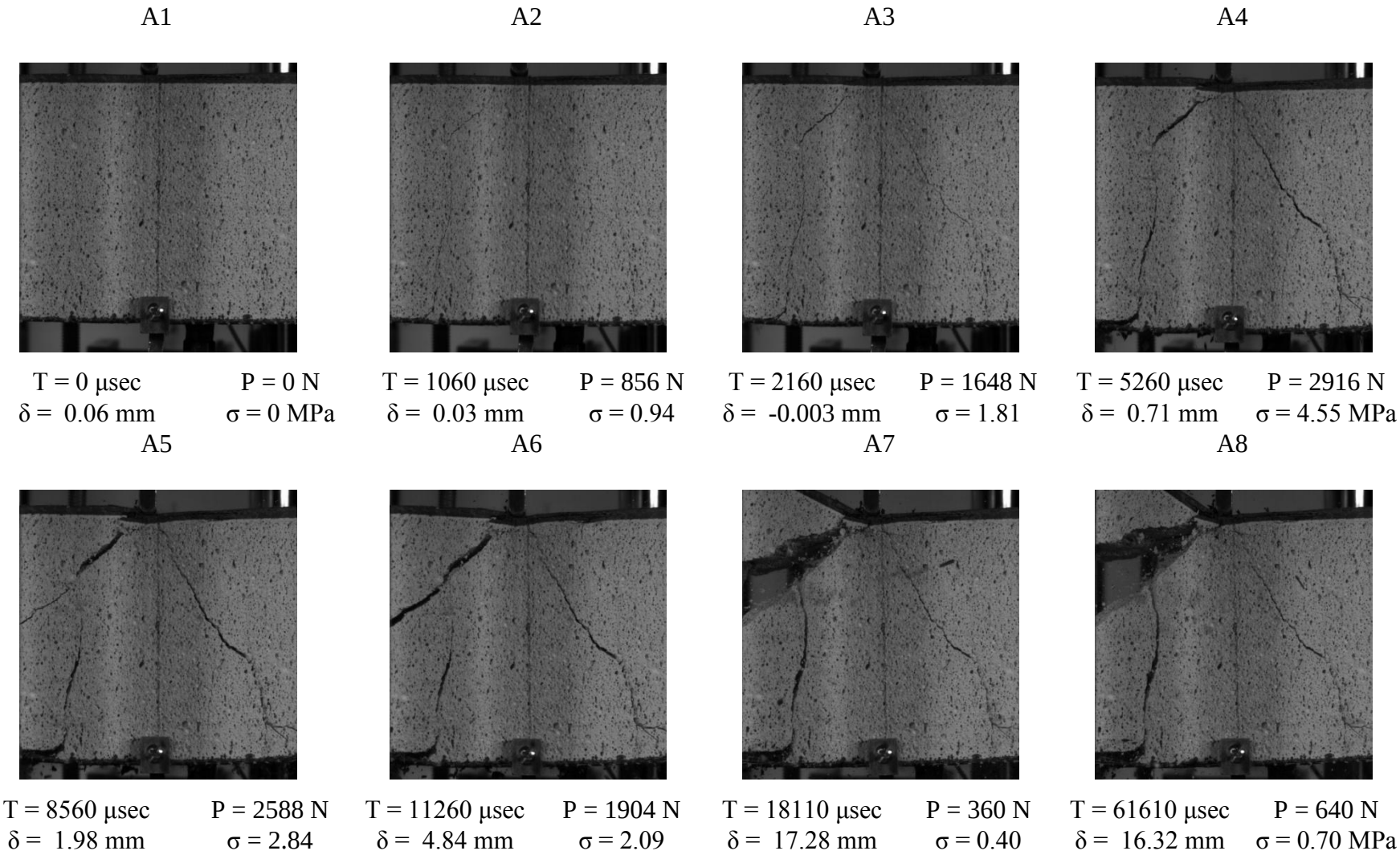

Figure 5-19 (b) : Crack propagation of SWAAC-B beam under impact loading (Drop Height = 300 mm)

Table 5-3 : Results of the impact tests conducted on the sandwich beams

Material	Drop Height	Velocity-Hammer	Velocity-Specimen	Strain Rate	Impulse	Max Impact Force	Max Flex. Stress	Max Defl.	Defl. at Max Force	Potential Energy	Absorbed Energy	Initial Rigidity
	mm	mm/sec	mm/sec	sec^{-1}	N-sec	N	MPa	mm	mm	N-mm	N-mm	N/mm
SWFRAC-A	25.4	706	13.8	0.05	28.8	1566	6.7	3.80	1.57	3479	4651	177
			(9.3)	(0.03)	(2.7)	(114)	(0.6)	(0.58)	(0.73)		(885)	(113)
	76.2	1223	76	0.85	33.1	1900	7.9	11.20	0.34	10437	8570	985
			(53)	(0.59)	(11.3)	(186)	(0.7)	(4.45)	(0.26)		(1557)	(225)
	152.4	1729	847	18.76	21.6	1694	7.1	19.42	0.04	20875	17901	919
			(134)	(2.97)	(5.1)	(178)	(0.7)	(0.07)	(0.05)		(5955)	(76)
SWAAC-A	25.4	706	8	0.03	31.6	1645	6.9	3.08	1.24	3479	3979	349
			(8)	(0.03)	(13.3)	(180)	(1.0)	(1.46)	(0.85)		(2186)	(237)
	76.2	1223	256	2.83	30.5	1859	7.9	13.88	0.39	10437	9046	799
			(416)	(4.60)	(18.3)	(369)	(1.6)	(5.91)	(0.28)		(4112)	(225)
	152.4	1729	49	1.10	41.5	2233	9.9	15.74	2.46	20875	24338	1382
			(24)	(0.53)	(6.2)	(413)	(2.0)	(2.77)	(1.58)		2498	410
SWFRAC-B	76.2	1223	14	0.15	41.0	2340	2.6	4.18	1.32	10437	8010	419
			(12)	(0.13)	(6.5)	(262)	(0.3)	(1.56)	(1.47)		(2458)	(207)
	152.4	1729	23	0.50	38.1	2902	3.2	5.50	1.79	20875	12293	294
			(5)	(0.10)	(5.3)	(69)	(0.1)	(0.65)	(0.14)		(2289)	(64)
	304.8	2445	68	3.03	52.4	3442	3.9	17.53	1.53	41750	25113	1805
			(80)	(3.57)	(17.8)	(452)	(0.7)	(3.22)	(0.71)		(10338)	(112)
SWAAC-B	76.2	1223	12	0.13	29.4	2288	2.3	3.12	1.06	10437	5794	581
			(2)	(0.02)	(1.5)	(175)	(0.2)	(0.43)	(0.20)		(423)	(450)
	152.4	1729	34	0.75	39.2	3016	3.5	7.62	0.82	20875	10005	961
			(33)	(0.73)	(26.0)	(405)	(0.5)	(2.09)	(0.55)		(2129)	(698)
	304.8	2445	66	2.92	57.8	3280	3.7	18.15	0.67	41750	19991	1975
			(24)	(1.05)	(10.0)	(352)	(0.4)	(1.39)	(0.73)		(6997)	(452)

Table 5-4 : Results of the static tests conducted on the sandwich beams

Material	Absorbed Energy	Rigidity	PEL Load	PEL Defl.	Max Load	Max Stress	Defl. at Max Force	Max Displ.
	N-mm	N/mm	N	mm	N	MPa	mm	mm
FRAC-A	840	1099	121	0.14	378	0.88	0.3	6.3
	(390)	(190)	(6)	(0.06)	(73)	(0.18)	(0.1)	(1.9)
SWFRAC-A	15229	1953	434	0.22	1680	3.54	2.2	13.3
	(4894)	(364)	(103)	(0.10)	(147)	(0.28)	(1.0)	(2.2)

Results obtained from the analysis of impact tests on sandwich beams with FRAC and AAC as the core have been presented in Table 5-3. Average and standard deviations (within brackets) have been reported in subsequent rows. Similar to the previous chapter, only apparent (total) toughness and deformation capacity has been reported. Test results from the static flexural tests conducted on FRAC-A and SWFRAC-A are shown in Table 5-4.

5.4 Conclusion

Static flexural and high strain impact tests were conducted on an innovative sandwich composite with aerated concrete as the core material and textile reinforced cementitious layer as boundary reinforcement. It was found that textile reinforcement improves the load carrying and energy absorption capacity along with deformation capacity and stiffness. This contributes to vast improvement in impact resistance under high strain dynamic loads. Effects of material properties of the core material, size effect of specimen and drop height of

impactor were studied in detail. Considering the ease of manufacturing, this type of a composite can be a solution to increase the structural strength of the lightweight aerated concrete core. This type of composite could find its application as structural members such as pre-fabricated building envelope systems.

REFERENCES

1. Mobasher, B., "Mechanics of Fiber and Textile Reinforced Cement Composites", CRC press, 2011, p. 480, ISBN: 9781439806609.

2. Bentur, A., Mindess, S., "Fibre Reinforced Cementitious Composites", Taylor & Francis, Second Edition, 2007, ISBN13: 978-0-415-25048-1

3. Balaguru, N., Perumalsamy, Shah, P., Surendra, "Fiber-Reinforced Cement Composites", Mc Graw-Hill, Inc., 1992, p. 6, ISBN: 0-07-056400-0

4. Naaman AE, Reinhardt HW., "Setting the stage: toward performance based classification of FRC composites". In: Proc of 4th Int workshop on High Performance Fiber Reinforced Cement Composites (HPFRCC-4), Ann Arbor, USA, June 15-18, 2003, p. 1–4.

5. Peled A, Mobasher, B. "Pultruded fabric-cement composites". ACI Materials Journal 2005;102(1):15-23.

6. Mobasher B, Peled A, Pahilajani J. "Distributed cracking and stiffness degradation in fabric-cement composites." Materials and Structures 2006; 39(287):317–331.

7. Mobasher, B., and Shah, S. P., "Test Parameters for Evaluating Toughness of Glass-Fiber Reinforced Concrete Panels," ACI Materials Journal, Vol. 86, No. 5, Sept-Oct. 1989, pp.448-458.

8. Shah, S.P., Ludirdja, D., Daniel, J.I., and Mobasher, B., "Toughness – Durability of Glass Fiber Reinforced Concrete Systems," ACI Material Journal, Vol. 85, No. 5, Sep. 1988, pp. 352-360.

9. Soroushian, P., Tlili, A., Yohena, M., and Tilsen, B.L., "Durability Characteristics of Polymer-Modified Glass Fiber Reinforced Concrete," ACI Material Journal, Vol. 90, No. 1, Jan-Feb. 1993, pp. 40-49.

10. Litherland, K.L., Oakley, D.R., and Proctor, B.A., "The Use of Accelerated Aging Procedures to Predict the Long Term Strength of GRC Composites," Cement and Concrete Research, Vol. 11, No. 3, May 1981, pp. 455-466.

11. Cockram, D.R., Litherland, K.L., Proctor, B.A., and Yale, B., "Assessing the Durability of Glass Compositions," Research and Development Laboratories of Pikington Brothers PLC, Lancashire, Glastech. Ber. 1983, 56 (Int. Glaskongr, 13th, band 1), pp. 644-649.

12. Proctor, B.A., Oakley, D.R., and Litherland, K.L., "Developments in the Assessment and Performance of GRC Over 10 Years," Composites (Guildford), Apr. 1982, pp. 173-180.

13. Proctor, B.A., "Past Development and Future Prospect for GRC Materials," Proceedings, International Congress on Glass Fibre Reinforced Cement (Paris, Nov. 1981), The Glass Fibre Reinforced Cement Association, Gerrards Cross, pp. 50-67.

14. Soranakom, C., and Mobasher, B., "Correlation of Tensile and Flexural Responses of Strain Softening and Strain Hardening Cement Composites," Cement and Concrete Composites, (in press Jan, 2008).

15. Soranakom, C., and Mobasher, B., "Flexural Modeling of Strain Softening and Strain Hardening Fiber Reinforced Concrete," Proceeding of the Fifth International RILEM Workshop, High Performance Fiber Reinforced Cement Composites (HPFRCC5), Mainz, Germany, July 2007, pp. 155-164.

16. Naaman, A. E., and Reinhardt H. W., "Proposed Classification of HPFRC Composites Based on Their Tensile Response", Materials and Structures, Vol. 39, June 2006, pp. 547–555.

17. Cohen, Z., Peled, A., Mobasher, B.,Janetzko,S.,Gries,T., "Hybrid Cement-Based Composites: Dynamic and Static tensile behaviors", BEFIB2012 – Fiber reinforced concrete Joaquim Barros et al., UM, Guimarães.

18. Soranakom C, Mobasher B. Correlation of tensile and flexural response of strain softening and strain hardening cement composites. CemConcr Compos, 2008;30:465-477.

19. Mobasher, B., Barsby, C., "Flexural design of strain hardening cement composites", BEFIB2012 – Fiber reinforced concrete Joaquim Barros et al., UM, Guimarães.

20. Sueki, S., Soranakom, C., Peled, A., and Mobasher, B. (2007), "Pullout–slip response of fabrics embedded in a cement paste matrix," Journal of Materials in Civil Engineering, 19, 9.

21. Soranakom C, Mobasher B. Closed-form moment-curvature expressions for homogenized fiber reinforced concrete. ACI Material Journal 2007; 104(4):351-9

22. Soranakom C, Mobasher B. Closed form solutions for flexural response of fiber reinforced concrete beams. Journal of Engineering Mechanics 2007;133(8):933-41.

23. Ulfkjaer, J.P., Krenk, S., Brincker, R.,"Analytical Model for Fictitious Crack Propagation in Concrete Beams," Journal of Engineering Mechanics, Vol. 121, No.1, 1995, pp.7-15.

24. Olesen, JF., "Fictitious Crack Propagation in Fiber-Reinforced Concrete Beams," Journal of Engineering Mechanics, Vol. 127, No. 3, March 2001, pp. 272-80.

25. Marikunte, S., and Aldea, C., and Shah, S.P., "Durability of Glass Fiber Reinforced Cement Composites: Effect of Silica Fume and Metakaolin," Advanced Cement Based Materials, Vol. 5, No. 3-4, Apr-May 1997, pp. 100-108.

26. Litherland, K.L., Oakley, D.R. and Proctor, B.A., The use of accelerated aging procedures to predict the long term strength of GRC composites, Cement and Concrete Research, vol. 11, pp. 455-466, 1981.

27. Majumdar, A.J and Laws, V., Glass fibre reinforced cement, Oxford BSP Professional Books, 1991, p. 197.

28. Aindow, A.J., Oakley, D.R. and Proctor, B.A., Comparison of the weathering behavior of GRC with predictions made from accelerated aging tests, Cement and Concrete Research, vol. 14, pp. 271-274, 1984.

29. Litherland, K.L. , Test methods for evaluating the long term behavior of GFRC, Proceedings - Durability of Glass Fiber Reinforced Concrete Symposium organized by PCI, ed. S. Diamond, November 12-15, 1985, Chicago , ed. S. Diamond, 1986, pp. 210-221.

30. Proctor, B.A., Oakley, D.R. and Litherland, K.L., Developments in the assessment and performance of GRC over 10 years, Composites, vol. 13, 1982, pp. 173-179.

31. Bentur, A. and Diamond, S., Fracture of glass fiber reinforced cement, Cement and Concrete Research, vol. 14, pp. 31-34, 1984.

32. Bentur, A., Mechanisms of potential embrittlement and strength loss of glass fiber reinforced cement composites, Proceedings - Durability of Glass Fiber Reinforced Concrete Symposium organized by PCI, Concrete Symposium organized by PCI, November 12-15, 1985, Chicago , ed. S. Diamond, 1986, pp. 109-123.

33. Shah, S. P., Ludirdja, D., Daniel J. I., Mobasher, B.,"Toughness-Durability of Glass Fiber Reinforced Concrete Systems", ACI Materials Journal, Sept-Oct. 1988, pp. 352-360. Discussion, 85-M39, ACI Materials Journal, July-Aug. 1989, p 425.

34. Mobasher, B., and Shah, S. P.,"Test Parameters in Toughness Evaluation of Glass Fiber Reinforced Concrete Panels", ACI Materials Journal, Sept-Oct. 1989, pp. 448-458.

35. Kumar, A. and Roy, D.M., Microstructure of glass fiber/cement paste interface in admixture blended Portland cement samples, Proceedings - Durability of Glass Fiber Reinforced Concrete Symposium organized by PCI, November 12-15, 1985, Chicago , ed. S. Diamond, 1986, pp. 147-156.

36. Leonard, S. and Bentur, A., Improvement of the durability of glass fiber reinforced cement using blended cement matrix, Cem. and Conc Res., vol. 14, pp. 717-728, 1984.

37. Litherland, K.L. and Proctor, B.A., The effect of matrix formulation, fiber content and fiber composition on the durability of glass fiber reinforced cement, Proceedings - Durability of Glass Fiber Reinforced Concrete Symposium organized by PCI, November 12-15, 1985, Chicago , ed. S. Diamond, 1986, pp. 124-135.

38. Purnell, P., Short, N.R., Page, C.L., Majumdar, A.J., Walton, P.L., Accelerated ageing characteristics of glass-fiber reinforced cement made with new cementitious matrices, Composites A, vol. 30, 1999, pp. 1073-80.

39. Zhu, W., Bartos, P.J.M., Assessment of interfacial microstructure and bond properties in aged GRC using a novel micro indentation method, Cement and Concrete Research, Vol. 27, No. 11, 1997, pp. 1701-1711.

40. Orlowsky, J., Raupach, M., Cuypers, H and Wastiels, J., Durability modeling of glass fiber reinforcement in cementitious environment, Materials and Structures vol. 38, March 2005, pp. 155-162.

41. Marikunte, S., Aldea, C. and Shah, S., Durability of glass fiber reinforced cement composites: effect of silica fume and metakaolin, Journal of Advanced Cement Based Composites, vol. 5, 1997, pp. 100-108.

42. Beddows, J. and Purnell, P., Durability of new matrix glass fiber reinforced concrete, GRC 2003 Proceedings of 12th Congress of the GRCA, October 2003, Barcelona, Spain, eds. J.N. Clarke and R. Ferry, paper 16.

43. Purnell, P. and Beddows, J., Durability and simulated ageing of new matrix glass fiber reinforced concrete, Cement and Concrete Composites, vol. 27, issues 9-10, October-November 2005, pp. 875-884.

44. Bijen, J., A survey of mew developments in glass composition, coatings and matrices to extend service life of GFRC, Proceedings - Durability of Glass

Fiber Reinforced Concrete Symposium organized by PCI, November 12-15, 1985, Chicago , ed. S. Diamond, 1986, pp. 251-269.

45. Bijen, J., Durability of some glass fiber reinforced cement composites, ACI Materials Journal, July-August, 1983, pp. 304-311.

46. Ball, H., Durability of naturally aged, GFRC mixes containing Forton Polymer and SEM analysis of the facture interface, GRC 2003 Proceedings of 12th Congress of the GRCA, October 2003, Barcelona, Spain, eds. J.N. Clarke and R. Ferry.

47. Qi, C., Tianyou, B., A review of the development of the GRC industry in China, GRC 2003 Proceedings of 12th Congress of the GRCA, October 2003, Barcelona, Spain, eds. J.N. Clarke and R. Ferry, paper 37.

48. Ambroise, J. and Péra, J., Durability of glass-fiber cement composites: comparison between normal, Portland and calcium sulphoaluminate cements, Proceedings Composites in Construction 2005 - Third International Conference, Lyon, July 11-13, 2005, pp. 1197-1204.

49. Litherland, K.L., Oakley, D.R. and Proctor, B.A., The use of accelerated aging procedures to predict the long term strength of GRC composites, Cement and Concrete Research, vol. 11, pp. 455-466, 1981.

50. Gartshore, G.C., Kempster, E. and Tallentire, A.G., A new high durability cement for GRC products, The Glass fiber Reinforced Cement Association 6th Biennial Congress, 21-24 October 1991, Maastricht, Netherlands Proceedings, pp. 3-12.

51. Cuypers, H., Wastiels, J., Orlowsky, Jana Raupach, M., Measurement of the durability of glass fiber reinforced concrete and influence of matrix alkalinity, Brittle Matrix Composites 7, Proceedings, A.M. Brandt, V.V. Li and I.H. Marshall eds., Warsaw, October 13-15, 2003, pp. 163-172.

52. Cuypers, H., Van Itterbeeck, P., De Bolster, E., Wastiels, J., Durability of cementitious composites, Composites in Construction 2005 - Third International Conference, Proceedings, Lyon, France, July 11-13, 2005, pp. 1205-1212.

53. Cuypers, H., Gu, J., Croes, K, Dumortier, S., Wastiels, J., Evaluation of fatigue and durability properties of E-glass fiber reinforced phosphate cementitious composite, Brittle Matrix Composites 6, Proceedings, A.M. Brandt, V.C. Li, I.H. Marshall eds., Warshaw, October 9-11, 2000, pp. 127-136.

54. Cuypers, H., Wastiels, J., Van Itterbeeck, P., De Bolster, E., Orlowsky, J. and Raupach, M., Durability of glass fiber reinforced composites experimental methods and results, Composites Part A, vol. 37, 2006, pp. 207-215.

55. Brameshuber, W. and Brockmann, T., Calcium aluminate cement as binder for textile reinforced concrete, International Conference on Calcium Aluminate Cements (CAC), Edinburgh, Scotland, 16-19 July 2001, pp. 659-666, 2001.

56. Brameshuber, W., Brockmann, Development and optimization of cementitious matrices for textile reinforced concrete, GRC 2001, Proceedings of the 12th International Congress of the International Glass fiber Reinforced Concrete Association, Dublin, Ireland, 14-16 May 2001, eds. N. Clarke and R. Ferry, pp. 237-249.

57 Litherland, K.L., Oakley, D.R., Proctor,B.A., "The use of accelerated ageing procedures to predict the long term strength of GRC compostes": Cement and Concrete Research, 1981, Vol. 11, pp. 455-466.

58. 523.2R, ACI., "Guide for Precast Cellular Concrete Floor, Roof and Wall Units", American Concrete Institute. Farminton Hills. 1996.

59. "Modeling Unsaturated Moisture Transport in Autoclaved Aerated Concrete: a Microstructural Approach". Trondheim, Norway : Building Physics, 2002.

60. ASTM C-1693, "Standard Specification for Precast Autoclaved Aerated Concrete (AAC) Wall Construction Units". ASTM International, PA. 2009.

61. Holt, E and Raivio, P.,"Use of gasification residues in aerated autoclaved concrete": Cement and Concrete Research, 2005, Vols. 35, 796 - 802.

62. Narayanan, N and Ramamurthy, K., "Structure and properties of aerated concrete: a review": Cement and Concrete Composites, 2000, Vols. 20, 321 - 329.

63. Bonakdar, A and Mobasher, B., "Multi-Parameter Study of External Sulfate Attack in Blended Cement Materials": Journal of Construction and Building Materials, 2010, Vols. V. 24, pp 61-70.

64. Radhi, Hassan., “Viability of autoclaved aerated concrete walls for the residential sector in the United Arab Emirates”, Energy and Buildings, 2011, Vols. 43, pp. 2086 – 2092.

65. Zollo, F. Ronald, and Hays, D. Carol., “Engineering Material Properties of a Fiber Reinforced Cellular Concrete”: ACI Materials Journal. Title no. 95 - M61.

66. Perez-Pena, M and Mobasher, B.,“Mechanical properties of fiber reinforced lightweight concrete composites”: Cement and Concrete Research, 1994, Vols. 24, pp. 1121 - 1132.

67. Gibson, L.J and Ashby, M.F.,“Cellular Solids, Structure and Properties”. Cambridge : Cambridge University Press, 1997.

68. Silva, Flavio de Andrade, et al., et al., “Impact Behavior of Sisal Fiber Cement Composites under Flexural Load”: ACI Materials Journal. Title no. 108 - M19.

69. Zhu, Deju, Gencoglu, Mustafa and Moabsher, Barzin.,"Low velocity flexural impact behaviour of AR glas fabric reinforced cement composites": Cement & Concrete Composites.

70. Glencoglu, Mustafa, Zhu, Deju and Mobasher, Barzin., "Static and Impact Behaviour of Fabric Reinforced Cement Composites in Flexure".

71. Silva, F. A. "Toughness of Non-conventional Materials". Msc Thesis, Department of Civil engineering. PUC-Rio : s.n., 2004.

72. Silva, F. A., Ghavami, K and d'Almeida, J.R.M.,"Toughness of Cementitious Composites Reinforced by Randomly Sisal Pulps". Head Island, SC : Eleventh International Conference on Composites Engineering (ICCE-11), 2004.

73. Romano, G.Q, et al., et al.,"Impact Loading Behaviour of Steel Fiber Reinforced Refractory Concrete exposed to High Temperatures". Tours, France : Fifth International Conference on Concrete under Severe Conditions: Evironment and Loading, 2007, Vols. V.2, pp. 54-59.

74. Bindiganavile, V and Banthia, N., "Polymer and steel fiber-reinforced cementitious composites under impact loading. Part 1: bond - slip response": ACI Materials Journal, Vols. 98(1), 17 - 24.

75. Bindiganavile, V and Banthia, N., "Polymer and steel fiber-reinforced cementitious composites under impact loading. Part 2: flexural toughness": ACI Materials Journal, Vols. 98 (1), 17 - 24.

76. Manolis, G.D, et al., et al.,"Dynamic properties of polypropylene fiber-reinforced concrete slabs": Cement and Concrete Composites, 1997, Vols. 19, 341 - 349.

77. Lok, T.S and Zhao, P.J., "Impact response of steel fiber-reinforced concrete using a split hopkinson pressure bar": Journal of Materials in Civil Engineering, 2004, Vols. 16(1), 54 - 59.

78. Choi, I.H and Lim, C.H., "Low-velocity impact analysis of composite laminates using linearized contact law": Composite Structures, Vols. 66, 125 - 132.

79. Wang, N.Z, Sidney, M and Keith, K., "Fiber reinforced concrete beams under impact loading": Cement and Concrete Research, 1996, Vols. 26 (3), 363 - 376.

80. Li, Z, Mu, B and Chui, SNC.,"Static and dynamic behavior of extruded sheets with short fibers": Journal of Materials in Civil Engineering, 2001, Vols. 13 (4), 54 - 59.

81. Serrano-Perez, Juan C., Uday K. Vaidya, Nasim Uddin, "Low velocity impact response of autoclaved aerated concrete / CFRP sandwich plates" : Composite Structures, 2007, Vols. 80, 621-630.

82. Yankelevsky, David Z., Avnon, Itzhak, "Autoclaved aerated concrete behavior under explosive action": Construction and Building Materials, 1998, Vols. 12, 359-364.

83. Laukaitis, A, Keriene, J, Mikulskis, D, Sinica, M, Sezemanas, G, "Influence of fibrous additives on properties of aerated autoclaved concrete forming mixtures and strength characteristics of products": Construction and Building Materials, 2009, Vols. 23, 3034-3042

84. Wittmann, F,H, and Gheorghita, I., "Fracture toughness of autoclaved aerated concrete", Cement and Concrete Research, 1984, Vols. 14, 369-374.

85. Song, P, S, Hwang, S, Sheu, B, C, "Strength properties of nylon and polypropylene fiber reinforced concretes", Cement and Concrete Research, 2005, Vols. 35, 1546 – 1550.

86. Bonakdar, A, Mobasher, B and Babbit, F. ,"Physical and mechanical characterization of fiber-reinforced Aerated Concrete (FRAC)", ACI Spring Convention. Chicago, IL : American Concrete Institute, March 21 - 25, 2010.

87. Cheresh, M. C. and McMichael, S.,"Instrumented impact test data interpretation". In: Kessler, S. L. et. al., editors. Instrumented impact testing of plastic and composite materials. Philadelphia. STP: ASTM, 1987. p. 963".

88. Cain, P.,J., "Digital filtering of impact data" Kessler Sl et al., editors. Instrumented impact testing of plastic and Composite Materials. Philadelphia. STP: ASTM, 1987. p. 963.

89. Land, P.L., "Strain rates for three and four point flexure tests": Journal of Materials Science, 1979, Vols. 14, 2760 - 2761.

90. Belingardi, G and Vadori, R.,"Low Velocity Impact Tests of Laminate Glass-fiber-epoxy Matrix Composite Material Plates": International Journal of Impact Engineering, 2002, Vols. 27, 213 - 229.

91. Mobasher, B, Pivacek, A and Haupt, G.J.,"Cement based cross-ply laminates": ACI Materials Journal, 1997, Vols. 6, 144 - 152.

92. Lee, H.K., Liang, Z., "Computational modeling of the response and damage behavior of fiber reinforced cellular concrete": Computers & Structures, 2004, Vols. 82, 581 – 592.

93. Mobasher, Barzin.,"Mechanics of Fiber and Textile Reinforced Cement Composites": CRC Press - Taylor & Francis Group, 2012.

94. Narayanan, N and Ramamurthy, K., "Structure and properties of aerated concrete: a review": Cement and Concrete Composites, 2000, Vols. 20, 321 - 329.

95. Tekalur, S.A., et.al. "Shock loading response of sandwich panels with 3-D woven E-glass composite skins and stitched foam core", Composites and Technology, 2009, Vols. 69, pp. 736 - 753